A HIGH PERFORMANCE AUTOMATIC MODE-MATCHED MEMS GYROSCOPE

A THESIS SUBMITTED TO
THE GRADUATE SCHOOL OF NATURAL AND APPLIED SCIENCES
OF
MIDDLE EAST TECHNICAL UNIVERSITY

BY

SONER SÖNMEZOĞLU

IN PARTIAL FULFILLMENT OF THE REQUIREMENTS
FOR
THE DEGREE OF MASTER OF SCIENCE
IN
ELECTRICAL AND ELECTRONICS ENGINEERING

SEPTEMBER 2012

Approval of the thesis:

A HIGH PERFORMANCE AUTOMATIC MODE-MATCHED MEMS GYROSCOPE

submitted by **SONER SÖNMEZOĞLU** in partial fulfillment of the requirements for the degree of **Master of Science in Electrical and Electronics Engineering Department, Middle East Technical University** by,

Prof. Dr. Canan Özgen
Dean, Graduate School of **Natural and Applied Sciences** ____________________

Prof. Dr. İsmet Erkmen
Head of Department, **Electrical and Electronics Eng.** ____________________

Prof. Dr. Tayfun Akın
Supervisor, **Electrical and Electronics Eng. Dept., METU** ____________________

Examining Committee Members

Prof. Dr. Sencer Koç
Electrical and Electronics Eng. Dept., METU ____________________

Prof. Dr. Tayfun Akın
Electrical and Electronics Eng. Dept., METU ____________________

Assoc. Prof. Dr. Haluk Külah
Electrical and Electronics Eng. Dept., METU ____________________

Dr. Said Emre Alper
Technical Vocational School for Higher Education, METU ____________________

Dr. Kıvanç Azgın
MEMS Center, METU ____________________

Date: ________________

I hereby declare that all information in this document has been obtained and presented in accordance with academic rules and ethical conduct. I also declare that, as required by these rules and conduct, I have fully cited and referenced all referenced material and results that are not original to this work.

Name, Surname: Soner SÖNMEZOĞLU

Signature:

ABSTRACT

A HIGH PERFORMANCE AUTOMATIC MODE-MATCHED MEMS GYROSCOPE

Sönmezoğlu, Soner

M.S., Department of Electrical and Electronics Engineering

Supervisor: Prof. Dr. Tayfun Akın

September 2012, 158 pages

This thesis, for the first time in the literature, presents an automatic mode-matching system that uses the phase relationships between the residual quadrature and drive signals in a gyroscope to achieve and maintain the frequency matching condition, and also the system allows controlling the system bandwidth by adjusting the closed loop parameters of the sense mode controller, independently from the mechanical sensor bandwidth. There are two mode-matching methods, using the proposed mode-matching system, presented in this thesis. In the first method, the frequency matching between the resonance modes of the gyroscope is automatically accomplished by changing the proof mass potential. The main motivation behind the first method is to tune the sense mode resonance frequency with respect to the drive mode resonance frequency using the electrostatic tuning capability of the sense mode. In the second method, the mode-matched gyroscope operation is accomplished by using dedicated frequency tuning electrodes that only provides a capability of tuning the sense mode resonance frequency generating an electrostatic spring effect on the sense frame, independently from the proof mass potential. This study mainly focuses on the second method because the proof mass potential variation is not desired during the gyroscope operation since the proof mass potential directly affects the drive and sense mode dynamics of the gyroscope. Therefore, a single-mass fully-decoupled gyroscope including the dedicated frequency tuning electrodes are designed. To identify mode shapes and mode frequencies of the designed gyroscope, FEM simulations are performed. The designed gyroscopes are fabricated using SOI-based SOG process. The fabrication imperfections are clarified during the formation of the structural layer of the gyroscope. Next, the closed loop controllers are designed for the drive amplitude control, sense force-feedback, quadrature cancellation, and mode-matching regarding the phase relationship between the quadrature and drive signals. Mode-matching is achieved by using a closed loop controller that provides a DC tuning potential. The mode-matching system consisting of vacuum packaged sensor, drive amplitude control, sense force-feedback, quadrature cancellation, and mode-matching modules is implemented on a printed circuit board (PCB), and then the system level tests are performed.

Tests illustrate that the mode-matching system operates in a desired manner. Test results demonstrate that the performances of the studied MEMS gyroscopes are improved up to 2.6 times in bias instability and 2 times in ARW under the mode-matched condition compared to the mismatched (~200 Hz) condition, reaching down to 0.73 °/hr and 0.024 °/√hr, respectively. At the mode-matched gyroscope operation, the better performance is obtained to be bias instability of 0.87 ^{0}/hr and ARW of 0.014 °/√hr, close to a theoretical mechanical Brownian noise limit of 0.013 °/√hr, under 10 mTorr vacuum ambient condition. The system bandwidth is adjusted and measured to be greater than 50 Hz. The mode-matched gyroscope has a linearity of 99.99% in a dynamic range of ±90 °/sec. The dynamic range can be increased above that level without sacrificing linearity.

To conclude, the proposed mode-matching system improves the performance of the gyroscope up to a mechanical Brownian noise limit by substantially suppressing the electronic noise of the sense mode controller and achieves sub-degree per hour performance without sacrificing system bandwidth and linearity.

Keywords: MEMS Gyroscope, Mode-Matching, Sub-degree per Hour Performance, Gyroscope Controller Design, MEMS Fabrication.

ÖZ

YÜKSEK PERFORMANSLI OTOMATİK MOD EŞLENMİŞ DÖNÜÖLÇER

Sönmezoğlu, Soner

Yüksek Lisans, Elektrik ve Elektronik Mühendsiliği Bölümü

Tez Yöneticisi: Prof. Dr. Tayfun Akın

Eylül 2012, 158 sayfa

Bu tez, bir MEMS dönüölçerin artık ofset ve sürüş sinyalleri arasındaki faz ilişkisini; frekans eşleme koşulunu sağlamak ve sürdürmek amacıyla kullanan otomatik bir mod eşleme sistemini literatürde bir ilk olarak sunmaktadır. Ayrıca bu sistem, mekanik sensör bant genişliğinden bağımsız bir şekilde kapalı döngü mod kontrolcü parametrelerini ayarlayarak, sistem bant genişliğinin kontrol edilmesini sağlamaktadır. Bu tezde sunulan mod eşleme sistemini kullanan iki ayrı mod eşleme yöntemine yer verilmiştir. İlk yöntemde, dönüölçerin rezonans modları arasındaki frekans eşlemesi, ataletsel kütle potansiyelinin değiştirilmesiyle otomatik olarak sağlanmaktadır. Bu yöntemin kullanımındaki esas neden, algılama modunun elektrostatik ayarlanabilme özelliğini kullanarak, algılama modu rezonans frekansını sürüş modu rezonans frekansına göre ayarlayabilme yetisidir. İkinci yöntemde, mod-eşlenmiş dönüölçer işleyişi, yalnızca algılama modu rezonans frekansının ayarlanabilmesini sağlayan ve algılama çerçevesinde elektrostatik yay etkisi yaratan, ataletsel kütle potansiyelinden bağımsız özel frekans ayarlayan parmak yapıları kullanılarak sağlanmıştır. Bu çalışma, dönüölçer işleyişi sırasında ataletsel kütle potansiyeline bağlı sürüş ve algılama mod dinamiklerinin, ataletsel kütle üzerindeki etkisi istenmediğinden, çoğunlukla bahsi geçen ikinci yöntem üzerine yoğunlaşmıştır. Bu sebeple, özel frekans ayarlayan parmak yapıları içeren tek kütleli, tamamıyla etkileşimsiz bir dönüölçer tasarlanmıştır. Tasarlanan dönüölçerin mod şekillerini ve mod frekanslarını tanımlayabilmek amacıyla, sonlu eleman analizleri gerçekleştirilmiştir. Bu dönüölçerler, SOI temelli SOG üretim tekniği kullanılarak üretilmiştir. Üretim kusurları, dönüölçerin yapısal katmanları oluşturulurken belirlenmiştir. Bir sonraki adım olarak, sürüş genlik kontrol, algılama modu güç geri besleme, ofset giderme ve mod eşleme işlemleri için, ofset ve sürüş sinyalleri arasındaki faz ilişkisi göz önünde bulundurularak, kapalı-döngü kontrolcüler tasarlanmıştır. Mod eşleme, DC ayarlama gerilimi sağlayan kapalı-döngü kontrolcü tarafından sağlanmıştır. Vakum paketlenmiş duyarga, sürüş genlik kontrol, algılama modu güç geri besleme, ofset giderme ve mod eşleme modüllerini içeren mod eşleme sistemi, bir baskı devre kartı (PCB) üzerinde birleştirilmiş ve daha sonra sistem seviyesinde testler gerçekleştirilmiştir.

Testler, mod eşleme sisteminin istenilen şekilde çalışmakta olduğunu göstermiştir. Test sonuçları eşlenmiş mod durumunda, eşlenmemiş mod (~200 Hz) durumuna göre, sabit kayma kararsızlığında 2.6 kata kadar, açısal rasgele kaymasında (ARK) 2 kata kadar, sırasıyla 0.73 °/saat'e ve 0.024 °/√saat'e ulaşarak, çalışılan dönüölçerlerin performansında gelişme olduğunu göstermiştir. Mod eşlenmiş dönüölçer işleyişi sırasında daha iyi performans 10 mTorr vakum koşulu altında sabit kayma kararsızlığı olarak 0.87 °/saat ve ARK olarak 0.014 °/√saat olarak elde edilmiştir ve bu sonuç teorik mekanik Brown gürültüsü olan 0.013 °/√saat'e yakındır. Sistem bant genişliği 50 Hz'den yüksek olacak şekilde ayarlanmış ve doğrulanmıştır. Mod eşlenmiş dönüölçer, ±90 °/sn dinamik ölçüm aralığında, %99.99 doğrusallığa sahiptir. Dönüölçerin dinamik ölçüm aralığı, doğrusallığı düşürmeden daha da yüksek değerlere artırılabilmektedir.

Sonuç olarak, önerilen mod eşleme sistemi, sistem bant genişliği ve doğrusallığından feragat etmeden, algılama modu kontrolcüsünün elektronik gürültüsünü ileri derecede bastırarak dönüölçer performansını mekanik Brown gürültüsü seviyesi sınırlarına kadar iyileştirmiştir ve neticede 1 ^{0}/saat'in altında performans elde edilmiştir.

Anahtar kelimeler: MEMS Dönüölçer, Mod Eşleme, 1 ^{0}/saat’in Altı Performans, Dönüölçer Kontrolcü Tasarımı, MEMS Üretimi.

To My Family

ACKNOWLEDGEMENTS

First of all, I would like to thank my thesis advisor Prof. Dr. Tayfun Akın for his guidance, support, and encouragement during my graduate studies. It is a great opportunity for me to work in his MEMS group.

I would like to thank to Dr. Said Emre Alper for his valuable suggestions and guidance during my M.Sc. study. The implementation of this study became easier for me with his knowledge and experience.

I would like to express my gratitude to Burak Eminoğlu, master of control electronics, for his valuable suggestions, helps, and precious friendship. Special thanks to Erdinç Tatar, my smart research partner, for his valuable suggestions and helps in tests of the mode-matching system. It is a really great chance for me to work with Burak Eminoğlu and Erdinç Tatar. I would also like to thank Mert Torunbalcı, master of the process, for his worthy helps during fabrication of MEMS gyroscopes.

I would like to thank Tunjar Asgarli, Cavid Musayev, Alperen Toprak, Dinçay Akçören, Uğur Sönmez, and Fırat Tankut, for fruitful discussions about the controller electronic design. I would like to express my gratitude to METU-MEMS center stuff, especially Orhan Şevket Akar and Dr. Kıvanç Azgın, for his helps and valuable suggestions in the fabrication of MEMS gyroscopes. Special thanks to Deniz Eroğlu, Serdar Tez, Osman Aydın, Dr. İlker Ender Ocak, Selçuk Keskin, Şeniz Esra Küçük, and Sevil Zeynep Lüleç for their valuable friendship.

I would like to express my gratitude and appreciation to my parents, Dursun and Melek Sönmezoğlu, and my siblings, Cevdet, Cemal, Kemal, and Selma Sönmezoğlu, for their endless support and encouragement throughout all my life. Special thanks to my brother Assist. Prof. Dr. Savaş Sönmezoğlu for his invaluable guidance in my academic and non-academic life.

TABLE OF CONTENTS

CHAPTERS

LIST OF TABLES

TABLES

LIST OF FIGURES

FIGURES

CHAPTER 1

INTRODUCTION

A vast number of researches have been conducted to track linear and angular movements of an object for over one century. Since then, many developments have taken place in the field of inertial sensors to get information about the exact position and orientation of a moving object within a specific time. Inertial sensors are classified in two main groups as accelerometers and gyroscopes due to their different sensing mechanisms and operation principles. The accelerometer and gyroscope are capable of measuring the linear acceleration and angular rotation rate, respectively. Today, they have wide variety of applications, in which automotive, military, consumer electronics, and aerospace are a couple of well-known application areas. Within the inertial sensors applications, the accelerometer and gyroscope are mostly used for not only inertial navigation that is the process of determining the exact position of the object but also stabilization of the object's position and orientation.

In 90's, MEMS (Micro-Electro-Mechanical System) technology provides an opportunity for the creation of miniaturized mechanical sensors in a microscopic scale with the aid of the developments in integrated circuit (IC) fabrication techniques. The MEMS technology brings about increase in the potential applications of the sensors, including microfluidics, biomedical, communications, aerospace, inertial measurement units, and so on. Among these, MEMS inertial sensors constitute one of the fastest growing area in the MEMS market thanks to the high reliability, promising performance, small size, and low cost. For example, the inertial sensor market had total revenue of $306 million in 2009, but in 2015, the expected total revenue is $1191 million, which is the most dynamic segment throughout MEMS market in the world [1].

MEMS accelerometers are presented earlier than MEMS gyroscopes in the literature. Therefore, there was much more research conducted on MEMS accelerometers. The high operational performance has been achieved due to their relatively simple mechanical structure and electronics. Today they are capable of detecting acceleration in a resolution of micro-g levels satisfying the requirements of inertial navigation applications. In contrast, the performances of the current MEMS gyroscopes are not sufficient to satisfy the requirements of inertial navigation applications. An example of gyro compassing needs a performance in ARW of 0.001 °/√hr and of bias instability of 0.005 °/√hr [2]. In fact, these performance requirements can be satisfied through fiber optic, laser, and mechanical gyroscopes, but these are not preferred due to the high cost, power consumption, and large size.

A vast number of different mechanical designs and fabrication techniques are tried to satisfy the requirement of high performance applications. Since the performance of the gyroscope came to a limit with respect to the development of mechanical designs and fabrication processes, today the research focuses on electronic interface electronics of the gyroscope because a high-quality electronic interface is required to operate the gyroscope at mode-matched condition. The mode-matching, which corresponds to 0 Hz frequency split between the resonance mode frequencies of the gyroscope, is a critical path to achieve high performance gyroscope operation. This thesis mainly focuses on the mode-matching concept to accomplish an improvement in the performance of the gyroscope operation and stable mode-matching operation in the presence of different environmental conditions, namely temperature and vacuum. This work proposes an automatic mode-matching system that enables to achieve and maintain the matching between the drive and sense resonance frequencies during operation without sacrificing the system bandwidth. The bandwidth of the system can also be controlled by adjusting closed loop sense mode controller parameters. For the first time in literature, the experimental verifications of the mode-matching system that utilizes the phase relationship between the drive and residual quadrature error signals in a gyroscope are performed. In the scope of this thesis, closed loop controllers, namely drive, sense, quadrature cancellation, and mode-matching loops were designed and operated to achieve the mode-matching operation by applying a DC tuning potential to the proof mass or special frequency tuning electrodes. These special frequency tuning electrodes were also designed and verified.

The organization of this chapter is as follows; Section 1.1 gives information about operation principles of MEMS vibratory gyroscopes to simply understand the actuation mechanism. Section 1.2 introduces performance specifications to determine the quality of the gyroscope and application areas regarding the performance requirements. The historical overview of the micromachined vibratory gyroscopes is summarized in Section 1.3. Section 1.4 demonstrates the gyroscopes studied in this study. Next, Section 1.5 provides overview of the mode-matching and its implementations, and lastly, Section 1.6 presents the research objective and thesis organization.

1.1 Operation Principles of MEMS Vibratory Gyroscopes

The MEMS vibratory gyroscope operation is mainly based on the Coriolis force, found and named by French scientist Gaspard Gustave de Coriolis. The Coriolis force is a fictitious force caused by the rotational movement of the system. To understand the Coriolis Effect, the object moving along the x-direction can be visualized. If the object is subject to a rotation about the reference z-axis when moving in the x-direction, the Coriolis force is exerted on the moving object along the y-direction. The direction of the exerted force is orthogonal to the movement direction of the object and the reference rotation axis, and also its amplitude is directly proportional with the velocity of the movement and rotation rate (Ω). Figure 1.1 shows the visualization of the Coriolis force with inertial frame coordinates.

The Coriolis force can be analytically expressed in [3] as

$$F_C = -2m\vec{\Omega} \times \vec{\mathrm{V}} \tag{1.1}$$

where m is the mass of the moving particle, and Ω and V are the rotation rate and velocity of the object with respect to the non-inertial reference frame.

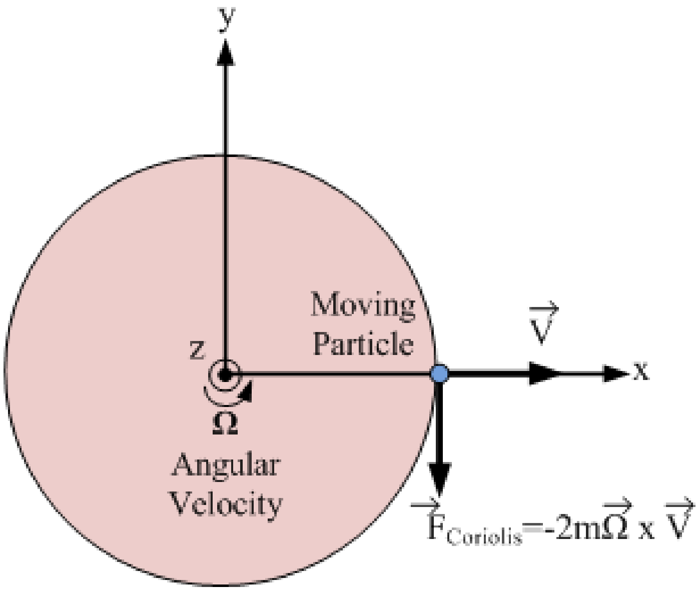

Figure 1.1: Visualization of the Coriolis force with inertial frame coordinates.

The MEMS vibratory gyroscopes basically consist of three suspended frames, namely drive, proof mass, and sense, which are mechanically connected through springs. Figure 1.2 shows the simplified view of the vibratory gyroscope. During the gyroscope operation, first the drive frame is continuously vibrated by means of piezoelectric, electromagnetic or electrostatic actuation mechanisms to ensure proper gyroscope operation because if the velocity of the drive frame becomes zero, the Coriolis force induced by rotation becomes zero, as shown in Equation 1.1. The proof mass frame vibrates along the direction of the drive and sense frames to transfer energy induced by the angular rotation rate to the sense mode. Then, the transferred energy, which is proportional to the amplitude of the angular rotation rate, leads to a displacement at the sense axis. This displacement is detected as an angular rotation rate in the sense mode of the gyroscope by using different sensing mechanisms, such as piezoelectric, optical detecting, piezoresistive or capacitive [4].

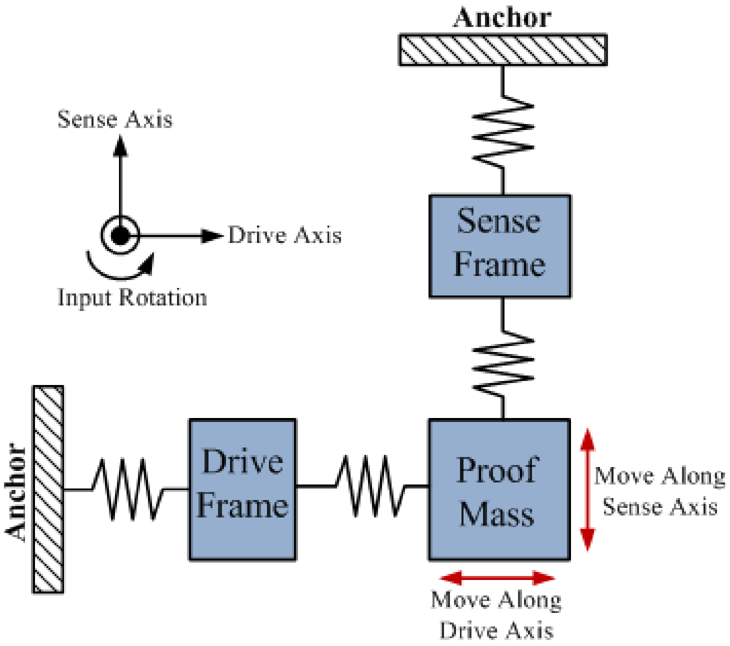

Figure 1.2: Simplified view of the vibratory gyroscope.

The drive and sense modes of the vibratory gyroscopes are excited into resonance using sinusoidal signals in order to achieve the highest possible gain during operation. The vibratory gyroscopes can be operated under two different conditions, mismatch and mode-matched, by adjusting difference between the resonance frequencies of the drive and sense modes. Since the Coriolis based energy caused by rotation is transferred to the sense mode by means of the proof mass frame vibrated at the drive mode resonance frequency, it is desired to operate the gyroscope under the condition of mode-matching corresponding to 0 Hz frequency split between the resonance modes of the gyroscope. The detailed information will be given in Section 1.5.

1.2 Performance Specifications and Application Areas

There are many criteria that are used to specify the quality of the gyroscopes with respect to application areas. Performance parameters (noise floor and bias instability) do not cover all of the requirements within a specific application. The other parameters, like scale factor, linearity, dynamic range, bandwidth, and operation temperature range should be considered as well. The mentioned performance parameters are the most commonly used ones, but the complete list of these can be found in [4]. The performance criteria are briefly summarized below.

Noise Floor: It directly indicates the minimum detectable signal level caused by rotation, and it is commonly expressed in a resolution unit of °/hr/√Hz. The overall noise floor (Ω_{Total}) of the system is determined by considering the Brownian noise (Ω_{Brownian}) coming from the mechanical sensor and the electronics noise ($\Omega_{\text{Electronics}}$) coming from the electronic blocks used to construct the control electronics of the gyroscope. The total equivalent noise floor of the system can be expressed as

$$\Omega_{Total} = \sqrt{\Omega_{Brownian}^2 + \Omega_{Electronics}^2} \qquad 1.2$$

The noise floor of the system is directly related to angle random walk (ARW), which is the angular measurement error of the gyroscope operation with time. It is expressed in a unit of °/√hr. The parameters of the noise floor and ARW can be expressed in terms of each other as

$$\Omega_{Total}\ (°/hr\ /\sqrt{Hz}) = ARW\ (°/\sqrt{hr}) * 60 \qquad 1.3$$

Bias Instability: There is always a finite amount of rate signal exist in the output of the gyroscope regardless of the absence of rotation. This finite amount of signal is called zero-rate output (ZRO) or bias. The stability of the bias is very critical for the gyroscope operation because it is the reference point by utilizing the rate output of the gyroscope in a specific time. The referenced bias can drift in time due to many reasons. Some of them are caused by the controller stability, ambient temperature variations, environmental vibrations, and sensor architecture. The bias drift should be suppressed as much as possible to achieve long term stability during the gyroscope operation. The unit of the bias instability is °/hr.

Scale Factor and Linearity: The scale factor is the measure of the rate output voltage variation in response to an angular rate input rotation. The scale factor of the gyroscope is determined from the slope of the rate output voltage vs. angular rate input rotation by fitting the best straight line to this slope through the method of least squares [4]. The unit of the scale factor is V/°/sec. The linearity (R^2) is the important parameter that shows the deviations at the rate output voltage from the desired output voltage in response to the angular rate input rotation, and it is determined from the correlation between the best fit straight line and the line which corresponds to the rate output voltage vs. angular rate input rotation.

Dynamic Range: It is the maximum applicable input range that the gyroscope responses to a rotation without losing the performance, and it is expressed in the unit of ± °/sec.

Bandwidth: It is directly related to the settling time of the system which indicates how fast the system responses to an abrupt input change like step function. In the open loop operation, the bandwidth is determined by the sensor, but in the closed loop operation, it is determined by the sense mode controller, independently from the mechanical sensor. It is expressed in the unit of Hz.

Temperature Range: It is the range for the proper operation of the system. In that range, the parameters of the sensor changing with temperature, such as the resonance frequencies of drive and sense modes of the gyroscope, should be identified and controlled in order not to substantially sacrifice the performance of the gyroscope.

The performance specifications discussed above should be considered while designing the sensor and the electronic interface of the system. In general, according to the performance metrics the MEMS gyroscopes are classified into three categories, inertial grade, tactical grade, and the rate grade gyroscopes [5]. In the scope of this thesis, the requirements for the high end of tactical grade applications have been satisfied and implemented. Table 1.1 shows the classification of gyroscopes with respect to the performance specifications.

Table 1.1: Classification of gyroscopes with respect to the performance specifications.

Parameter, Unit	Rate Grade	Tactical Grade	Inertial Grade
Angle Random Walk, °/√hr	>0.5	0.5-0.05	<0.001
Bias Instability, °/hr	10-1000	0.1-10	<0.01
Scale Factor Linearity, %	0.1-1	0.01-0.1	<0.001
Dynamic Range, °/sec	50-10000	>500	>400
Bandwidth, Hz	>70	~100	~100

The MEMS gyroscopes are utilized in a various number of applications due to their size, weight, and cost. Some of the main application areas can be summarized as follows [6],

- Consumer Electronics
- Industry
- Military
- Automotive

The applications of the gyroscopes differ with respect to the performance requirements of the system. Some of the applications, such as robotics, gyro compassing, inertial navigation, and some consumer electronics, use high performance gyroscopes to satisfy the measurement accuracy of the system. However, in automotive applications, such as vehicle stabilization, rollover detection for airbags, there is no need to use high performance MEMS gyroscopes due to the application requirements. In general, the rate grade gyroscopes satisfy most of the requirements of the automotive applications.

1.3 Overview of the Micromachined Vibratory Gyroscopes

The history of the gyroscopes was started with the understanding of the principle operation of the gyroscope, which was first demonstrated and reported by George H. Bryan in the early of 1890’s [7]. Then the first micromachined vibratory gyroscope implementations were demonstrated in 1980’s with quartz piezoelectric gyroscopes [3], but their processes were not IC compatible. In 1991, Draper Laboratory demonstrated the first IC compatible micromachined vibratory gyroscope fabricated on a silicon wafer, with a resolution of 4 °/sec in a 1Hz bandwidth [8]. In 1993, the Draper Laboratory reported a silicon-on-glass tuning fork gyroscope fabricated using a dissolved wafer process with a performance improvement in resolution, which is equal to 0.19 °/sec in a bandwidth of 1 Hz. In this work, the stray capacitance was minimized using the silicon-on-glass technique [9].

After 1993, there were many different fabrication techniques and gyroscope structures used to accomplish a performance improvement. In 1994, the first ring gyroscope was developed by integrating CMOS readout electronics in University of Michigan through metal electroforming [10]. It demonstrated an impressive performance with a resolution of 0.5 °/sec and a bandwidth of 25 Hz. A further improvement in the ring gyroscope was achieved through the development of high-aspect ratio trench-refill technology [11]. Since the smallest capacitive gaps and thicker structural layer accomplished with this technology ensures a higher sensitivity and lower Brownian noise, respectively, the performance of the gyroscope was improved up to a resolution of 0.01 °/sec in a bandwidth of 1 Hz [12]. In 2002, a further development in vibratory ring gyroscope was achieved by using deep-reactive-ion-etching (DRIE) fabrication technique [13]. This gyroscope fabricated on single crystal silicon with a thickness of 150 μm demonstrated a resolution of 10.4 °/hr in a 1 Hz bandwidth. The ring gyroscope shows some special features compared to other type gyroscope structures. It provides excellent matching between the resonance modes, minimum undesired mechanical cross-talk between the drive and sense modes, and minimum temperature dependency during the operation, thanks to the symmetry of the structure, but the amplitude of actuation displacement is the main limitation to obtain better performance compared to other gyroscope designs. Therefore, the tuning fork gyroscope structure had started to gain importance due to the advantage of large amplitude vibration. R. Bosch GmbH reported a silicon yaw tuning fork gyroscope fabricated using combination of bulk and surface micromachining techniques [14]. It has large amplitude vibration (about 50 μm) with the minimized mechanical crosstalk between the modes. The performance of the gyroscopes was demonstrated in a resolution of 0.4 °/sec/√Hz under the atmospheric pressure thanks to its large oscillation amplitude of 50 μm.

Furthermore, in mid-1990’s, surface-micmomachined gyroscopes were realized with the help of easy integration capability with the CMOS technology. Murata reported the first simple-shaped surface micromachined gyroscope with a resolution of 2 °/sec/√Hz [15]. R. Bosch GmbH also reported a surface micromachined silicon gyroscope with a resolution of 1.26 °/sec at a bandwidth of 10 Hz [16]. There is also research conducted on the CMOS-integrated gyroscopes fabricated using surface micromachining technique. This is accomplished by Analog Devices, which reported a surface-micromachined tuning fork gyroscope that was fully integrated with the IC electronics on the same wafer by using BiCMOS process in 2002 [17]. In this gyroscope, the undesired mechanical cross-talk is significantly suppressed by using optimal mechanical levers. Despite the thickness of the structure (4 µm) causing a high Brownian noise due to the limited amount of mass of the structural layer, the gyroscope demonstrated an impressive resolution of 0.0015 °/sec/√Hz thanks to a high quality fabrication process and mechanical sensor architecture. Another approach to combine the gyroscope and its electronics on a single chip is a post-CMOS process reported by Carnegie Mellon University in 2002 [18]. In this process, the gyroscope and its electronics are constructed on the same CMOS wafer, and the gyroscope is released through a high-aspect ratio DRIE etching. The performance of the gyroscope was reported as 0.5 °/sec at bandwidth of 1 Hz. Among the gyroscopes fabricated by surface micromachined post-CMOS process, after the gyroscope is released, curling is generally observed at the structure layer caused by the residual stress in the layers, which is undesired in production of gyroscopes. In 2003, Carnegie Mellon University reported the improved version of the surfaced micromachined gyroscope combined with CMOS electronics on a same chip [19]. The new version of the gyroscope is fabricated with a thicker structural layer (60 µm) by using bulk micromachining technique to achieve an increase in the mass, resulting in Brownian noise suppression, and to overcome the residual stress effect causing curling. In most of the new generation gyroscopes, the advantages of the bulk and surface micromachining are combined to fabricate the gyroscopes to achieve high performance.

On the other hand, in 2000’s different types of mechanical designs combined with the electronics have been investigated, and reducing the undesired mechanical cross-talk between the resonance modes of the gyroscope drew much more attention to achieve high performance. In 2001, Samsung proposed a decoupled gyroscope to minimize the mechanical crosstalk, called quadrature error, between the vibration modes [20]. The independent spring structures were used for mitigation of the undesired coupling between modes of the gyroscope. It demonstrated a resolution of 0.013 °/sec at a bandwidth of 60 Hz. In 2002, HSG-IMIT also reported a decoupled micro-gyroscope that mechanically minimizes quadrature error with a resolution close to 0.07 °/sec in a bandwidth of 50 Hz [21]. In mid-2000's, a decoupled tuning-fork gyroscope demonstrating a quadrature error minimization by combining the mechanics and electronics was reported with a performance 0.01 °/sec/√Hz [22]. A more complicated mechanical design compared to a tuning-fork structure was also reported to reduce the quadrature error in [23], but its performance was limited due to low-quality electronics. After minimizing the quadrature error through different mechanical designs, many researchers started to focus on the mode-matching concept for further performance enhancement.

In 2006, a mode-matched tuning fork gyroscope was reported by Georgia Institute of Technology with a high performance in ARW of 0.045 °/√hr and bias instability of 0.96 °/hr [24]. The performance of this gyroscope was substantially improved through the mode-matching to 0.003 °/√hr in ARW and 0.16 °/hr in bias instability by characterizing the sensor structure and using high-quality CMOS electronics [25]. In 2009, a mode-matched gyroscope with digital control electronics was reported by Thales Avionics with a performance of 0.01 °/√hr in ARW and <0.1 °/hr in bias instability [26]. In the same year, Sensonor also presented a digitally controlled tuning-fork gyroscope operated under the mode-matched condition with a target performance in ARW of 0.002 °/√hr and bias instability of 0.04 °/hr [27].

In conclusion, there are various number of mechanical designs and fabrication techniques investigated to enhance the performance of the gyroscopes in the literature but it is clearly observed that the performance of the gyroscopes is improved by minimizing the undesired mechanical cross-talk between the drive and sense modes of the gyroscope, satisfying large amplitude vibrations at the drive mode, increasing thickness of the structural layer, using high-aspect ratio fabrication techniques, combining the gyroscope with high-quality electronics, and operating under the mode-matched condition. Today most of the researchers are generally focused on the mode-matching concept by using mechanically decoupled gyroscope structures. On the other hand, there is a research continues on the development of more robust and high-quality gyroscope electronics for mode-matching to achieve better performance in resolution and bias instability.

1.4 Gyroscopes Studied in This Thesis

Figure 1.3 shows an SEM image of the fully-decoupled gyroscope studied in this thesis. This gyroscope was studied to cancel the quadrature error and observe effects of quadrature cancellation on the gyro performance [28]. After the quadrature cancellation, it is also used for the mode-matching implementation as a first phase of this study [29].

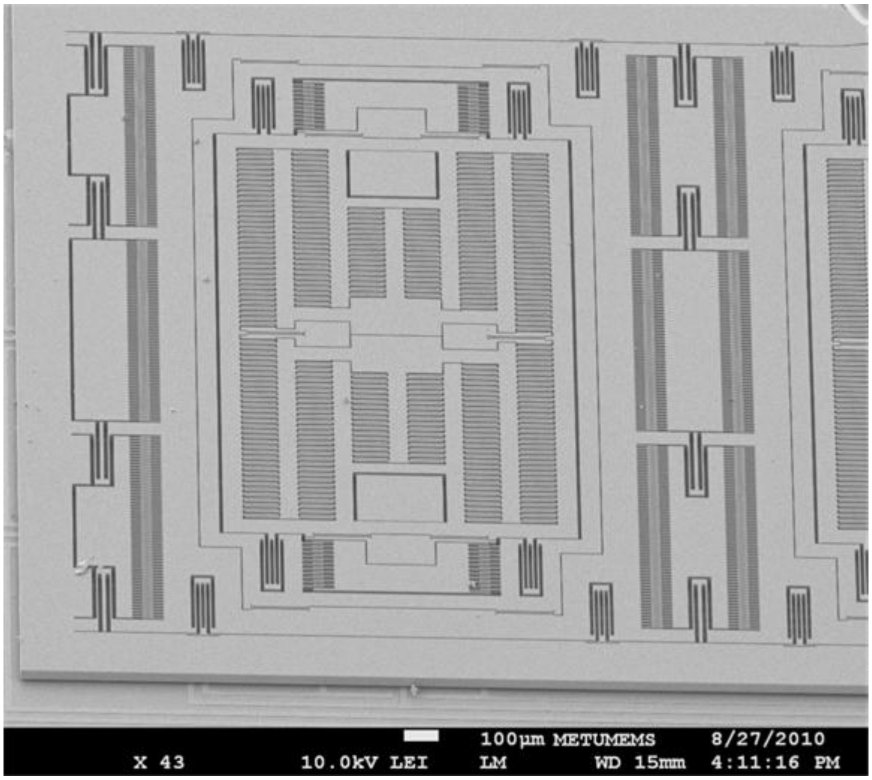

Figure 1.3: SEM image of the fully-decoupled gyroscope studied in the scope of this thesis [28].

In tuning-fork gyroscope designs, two identical gyroscopes are used, but they are vibrated in an opposite direction. Their outputs are differentially read to eliminate common linear acceleration. Also, the same idea is used in the design of the fully-decoupled gyroscope, shown in Figure 1.3. However, these two identical gyroscopes are not mechanically connected to each other except drive mode. The lack of the mechanical connection causes two different resonance peaks at the sense mode output of the gyroscope due to fabrication imperfections, which leads to spring imbalances. In this work, since the phase relationship between the quadrature error signal and drive pick signal are used to accomplish the mode-matching gyroscope operation, there is only a need for a single resonance peak in both sense and drive modes of the gyroscope. Therefore, one of the sense resonance peaks is eliminated by cutting the electrical connections of one of the two identical. If it is not eliminated, the quadrature error coming from the unmatched sense resonance peak, which has a different phase characteristic compared to the matched sense resonance peak, prevents an exact frequency matching between modes of the gyroscope. Thus, the gyroscope is used as a single-mass gyroscope with mechanical quadrature cancellation electrodes which are used to cancel out the undesired mechanical cross-talk between the drive and sense modes of the gyroscope by applying a differential DC potential to quadrature cancellation electrodes.

In this study, the main motivation behind the mode-matching implementation is to match drive and sense mode frequencies of the gyroscope by using tuning capability of the sense mode resonance frequency. In the first phase of this study, the gyroscope, shown in Figure 1.3, is operated under the mode-matched condition by changing the proof mass potential, which provides tuning of the sense mode resonance frequency.

Figure 1.4 shows the single-mass fully-decoupled MEMS gyroscope with additional frequency tuning electrodes studied in the scope of this thesis. In the second phase of this study, the mode-matched gyroscope operation is satisfied by applying a DC potential to frequency tuning electrodes. The gyroscope is comprised of a single mass with additional frequency tuning electrodes to mechanically eliminate one of two sense resonance peaks discussed above and to satisfy the mode-matching operation without changing the proof mass potential. In the gyroscope operation, generally, it is undesired to change the proof mass potential because it directly affects overall system dynamics. Therefore, it should be changed in a defined region or kept constant when changing from mismatch condition to mode-matched condition during gyroscope operation.

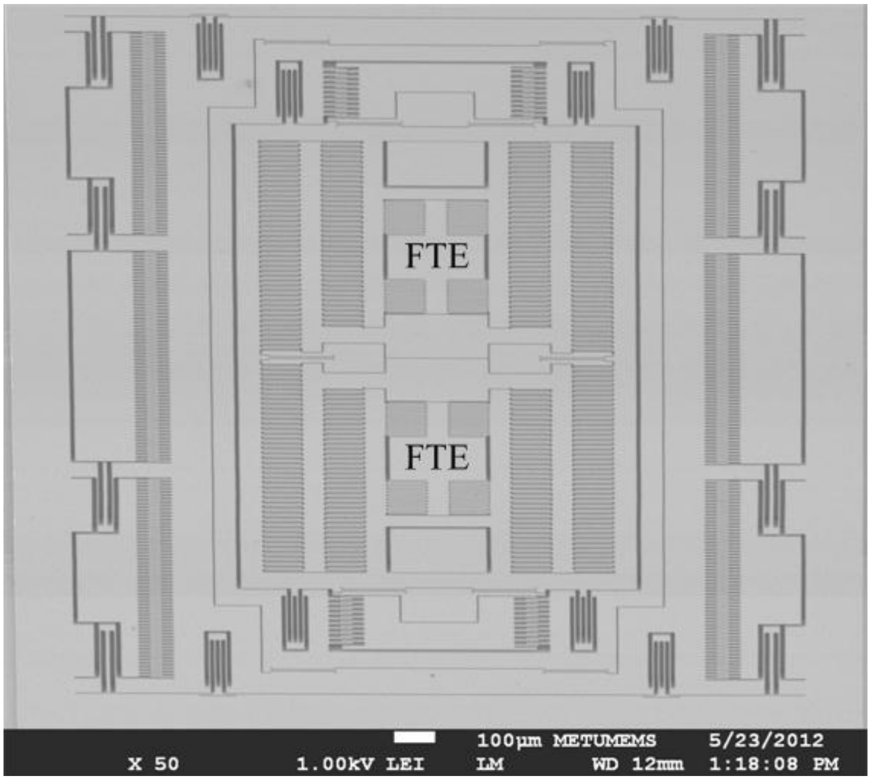

Figure 1.4: SEM image of a single-mass fully-decoupled MEMS gyroscope with additional frequency tuning electrodes (FTEs) studied in the scope of this thesis.

These two gyroscopes studied in this thesis are fabricated in METU with a structural thickness of 35µm through the SOG-based SOI process outlined in [30].

The main purpose in this thesis is to achieve the-matched gyroscope operation and to observe the effects on the gyroscope performance. For the first time in METU, there is a research study conducted on the mode-matching gyroscope operation, and it was successfully accomplished. There were two different methods used for matching frequencies of resonance modes. Before using these methods, controller electronics, which are drive, sense, quadrature, and mode-matching control loops, were constructed and implemented after optimizing them by means of simulations. Then, the mode-matching condition was obtained changing the proof mass potential of the gyroscope, shown in Figure 1.3. Following, it was satisfied applying a DC potential to dedicated frequency tuning electrodes placed in the designed single-mass fully-decoupled gyroscope, shown in Figure 1.4.

1.5 Overview of Mode-Matching and Its Implementations

Mode-Matching is a concept that is used to obtain maximum mechanical output response from the sensor. This means that when the drive and sense mode resonance frequencies of the gyroscope are exactly matched, sensitivity becomes maximum, which leads to a significant performance improvement of the system. Undesired electronic noise, coming from mostly the preamplifier stage, plays an important role when determining performance of the gyroscope. This electronic noise is significantly suppressed when the gyroscope is operated under the mode-matched condition because the output signal of the gyroscope is significantly amplified due to increase in the mechanical response. Hence, an improvement in the signal-to-noise ratio (SNR) of the system, which provides less prone to electronics noise, is also obtained through the mode-matching.

The mechanical output response of the gyroscope is directly proportional with the sense mode displacement. The sense mode displacement maximizes due to coupling mechanism between the Coriolis acceleration caused by rotational movement and sense mode of the gyroscope when the resonance mode frequencies of the gyroscope is matched. When there is Coriolis acceleration in the system, it is directly modulated with drive mode resonance frequency. After the modulation, it is directly coupled with the sense mode through the proof mass of the gyroscope. Amount of coupling highly depends on the frequency separation between the drive and sense mode resonance frequencies of the gyroscope. If the resonance characteristics of the sense mode are considered, the maximum coupling is obtained in the mode-matched case because the modulated Coriolis acceleration is transferred to the sense mode with a maximum gain. Thus, the maximum mechanical response at the output of the gyroscope is obtained under the mode-matched condition. Figure 1.5 shows the amount of the sense mode displacement due to Coriolis acceleration with respect to mismatch (a) and mode-matched (b) cases. Sense mode displacement increases in the presence of rotational movement at the system when the frequency separation between the resonance modes of the gyroscope goes to zero.

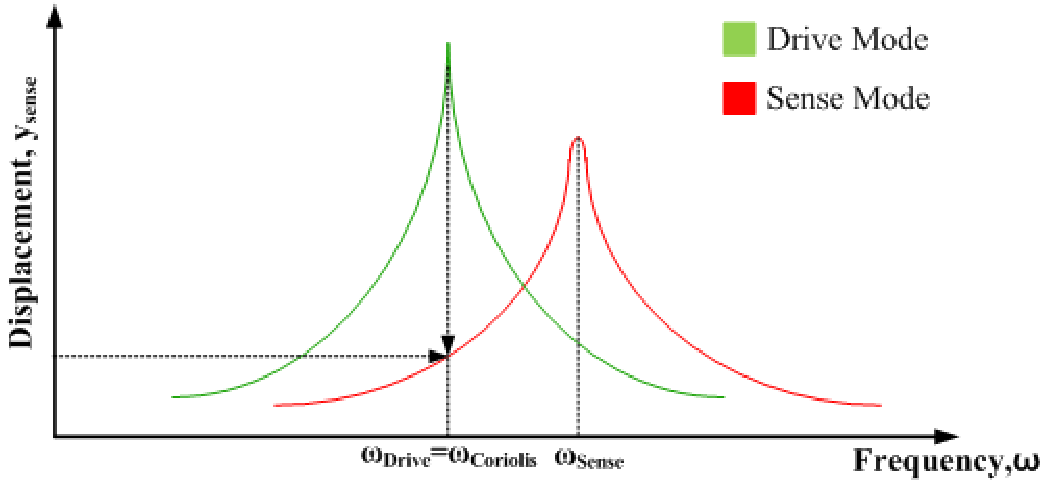

(a) Mismatch Case

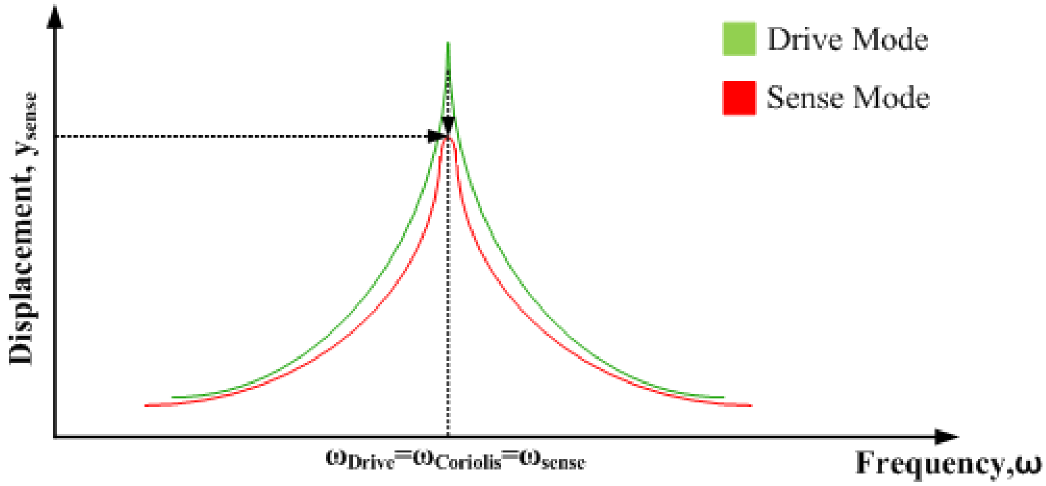

(b) Mode-Matched Case

Figure 1.5: Amount of the sense mode displacement due to Coriolis acceleration with respect to mismatch (a) and mode-matched (b) cases. The sense mode displacement increases in the presence of rotational movement at the system when the frequency separation between the resonance modes of the gyroscope goes to zero.

There are number of different approaches presented in the literature to reduce the frequency separation between the resonance modes. Some of the proposed approaches used localized thermal stressing effect [31], laser trimming [32], and selectively deposited polysilicon [33]. Since these approaches utilize the change in the mechanics of the structural layer or structural material, they are not reliable for proper mode-matching operation because of the sensitivity of the unexpected condition variations, such as temperature and vacuum. In addition, these methods are not desirable in terms of time, cost, and process complexity because they need a manual tuning effort.

Today, a more effective method is to use an electrostatic spring constant effect to tune drive and sense mode resonance frequencies of the gyroscope. The tuning of the resonance modes of the gyroscope is accomplished by applying a DC potential to a proof mass or special frequency tuning electrodes. Some of them used iterative methods, which rely on computational algorithms [34, 35]. In these methods, first, the drive and sense mode resonance frequencies are determined through the resonance tests, and then they are continuously monitored to find the optimum bias potential, which provides 0Hz frequency split between the mode frequencies. There are various number of iterations performed depending on the quality factor of the resonance modes. In high-Q systems, iteration procedures are much more time-consuming because it requires more iterations to reach optimum bias potential, and also they are more sensitive to the environmental condition variations because of the lack of feedback control mechanism, which ensures a stable mode-matching operation.

Among the frequency tuning methods, an automatic and real-time tuning mechanisms are much more preferable to achieve and sustain the mode-matched gyroscope operation thanks to the insensitivity to ambient variations. Some of the current implementations, which use the automatic and real-time mode-matching mechanisms, are summarized as follows. In [25], the amplitude information of the zero-rate output (ZRO) of the gyroscope caused by minimized quadrature error was used to achieve exact frequency matching between resonance modes of the gyroscope. In this application, the mode-matching is automatically accomplished and sustained through digital control loops. However, this application suffers from a bandwidth limitation due to the open loop sensing mechanism, which brings a confinement at the application areas. There is another approach that demonstrated a mode-matching operation over a bandwidth of 50Hz [36]. The mode-matching operation was performed using two pilot tones injected to the sense mode dynamics of the system. The amplitude difference information between the tones equally separated from the drive resonance frequency is used to achieve automatic mode-matched operation with digital control electronics, but the reported resolution performance is limited with 14.4 °/hr/√Hz. In [37], the mode-matching was electronically carried with the closed loop feedback mechanism by introducing a square wave dither signal as quadrature signal into a gyroscope's sense mode, and then monitoring its phase variation across the sense mode. However, the bandwidth and performance of the gyroscope is limited with 10 Hz and 12 °/hr. In [38], the use of the PLL based approach was proposed to tune the sense mode resonance frequency with respect to a reference frequency namely, drive resonance frequency by means of tunable electrode structures. The main idea behind this method is to use phase relationship between the drive and sense mode resonance frequencies of the gyroscope. There were no experimental data demonstrated regarding the system bandwidth and gyroscope's performance.

Each of the proposed methods regarding the automatic and real-time mode-matching systems discussed above suffers from bandwidth or performance or both of them. Today, the most accepted research consideration is to reach a high performance through the mode-matching without sacrificing the system bandwidth in the gyroscope applications. The developed study in this thesis eliminates the bandwidth limitation while providing the performance that meets the requirement of high-end of tactical grade applications.

1.6 Research Objectives and Thesis Organization

The main purpose of this work is to construct an automatic mode-matching system depending on real-time tuning mechanism during the gyroscope operation and hence to reach high performance without sacrificing the system bandwidth. The specific objectives of this work can be listed as follows:

1. Modification of a fully-decoupled gyroscope. Since the gyroscope includes mechanically unconnected two identical gyroscopes, there are two resonance peaks observed at the sense mode. Therefore, one of them should be eliminated to satisfy a requirement of the mode-matching. The tuning characteristic of the sense mode should be investigated under the changing proof mass potential. Since the tuning is satisfied with changing proof mass potential, the effects of proof mass variation of the system on the overall system dynamics should also be discussed to prevent possible instability at the closed loop controllers.

2. Design of a single-mass fully-decoupled gyroscope consisting of frequency tuning electrodes. The frequency tuning electrodes should be placed in a gyroscope to generate an electrostatic force based on electrostatic spring constant effect for tuning the sense mode resonance frequency, independently from the proof mass potential. The number of the frequency tuning electrodes should be determined. Therefore, they will identify initial maximum allowable frequency separation between the mode frequencies to achieve the mode-matching in a predetermined potential range. Considering the design of the gyroscope, spring constants, which are used to determine gyroscope's mode frequencies, should be adapted to confine sense and drive mode resonance frequencies in a frequency tuning range by considering the proof mass potential. The placement of pads' metallization should be made by considering couplings between the pads in order to minimize the inevitable capacitive coupling effect between the resonance modes. Furthermore, the effect of common acceleration on the gyroscope output in the presence of angular rotation should be investigated.

3. Fabrication of a designed single-mass gyroscope by using SOG-based SOI process. The problems related to the fabrication should be deeply investigated, and then they should be solved considering all of the fabrication steps separately. Process optimization should be performed to achieve a consistency between parameters of the fabricated and designed sensor.

4. Design and implementation of controller electronics. The controller electronics of the system is comprised of the drive, sense, quadrature and mode-matching control loops. The closed loop feedback mechanism is preferred by constructing them to achieve stable gyroscope operation. Since stability is the main concern in a controller design, open loop and closed loop stability analysis of the controller should be performed, and then the controller parameters should be separately adjusted with regard to the analysis results for each different loop to get stable operation. At the stage of controller implementation, its parameters should also be revised by considering tolerances of the real electronic components. As a next the controller electronics should be combined with the gyroscope on a PCB to observe the overall system performance.

The organization and the contents of this thesis are arranged as follows:

Chapter 2 presents detailed information about the theory behind the MEMS vibratory gyroscopes. After understanding the theory, the mechanical modeling of gyroscope dynamics is introduced with the relevant equations. Then, the design considerations, extraction of the electromechanical model parameters, quadrature cancellation mechanism, and electrostatic spring effect are briefly discussed. The design of frequency tuning electrodes is also provided with the governing equations after getting an idea about the electrostatic spring effect. Lastly, the mechanical simulations, which are performed using finite element methods (FEM), are demonstrated to observe modal frequencies of the single-mass fully-decoupled gyroscope.

Chapter 3 describes the design of the drive, sense, quadrature, and mode-matching controllers. In the design of the controllers, the stability analysis of the open loop system performed in Laplace domain and closed loop time domain analysis performed in a SIMULINK are demonstrated in a detailed manner. This chapter also presents the noise performance of the overall system with regarding the mechanical Brownian and electronic noise.

Chapter 4 gives the details of SOG-based SOI process used to fabricate the single-mass fully-decoupled gyroscope. Fabrication results are also covered in this chapter.

Chapter 5 demonstrates the test results of the gyroscopes used in this study. These results include the parameters of angle random walk (ARW), bias instability, scale factor, dynamic range, and linearity for mismatched and mode-matched gyroscope operations to make a comparison between them. In addition, the performances of ARW and bias instability of the gyroscope under the mode-matched condition is presented for different temperature and vacuum conditions to observe the effects on the gyroscope performance.

Chapter 6 presents the summary of the conducted work and its contributions. The future research study related to this work is also identified in the light of obtained results.

CHAPTER 2

VIBRATORY GYROSCOPE THEORY AND MODELLING

This chapter describes the electromechanical model of the vibratory gyroscopes studied in this thesis. Section 2.1 provides a mechanical model of the gyroscope, and then the dynamics of the drive and sense modes of the proposed vibratory gyroscope are discussed in Section 2.2. Section 2.3 explains the extraction of the model parameters. Following, Section 2.4 and 2.5 demonstrate the actuation and capacitive sensing mechanisms in the gyroscope, respectively. Next, Section 2.6 explains the electrostatic spring constant effect used for tuning of the resonance frequencies and then Section 2.7 describes the design of the frequency tuning electrodes used for the mode-matching. Section 2.8 explains the definition of the quadrature error and its cancellation mechanism required to achieve mode-matching. Section 2.9 presents the mechanical model simulations of the gyroscope designed in this work performed by using finite element method (FEM). Finally, this chapter is summarized in Section 2.10.

2.1 Mechanical Model of the Gyroscope

In the mechanical design of the vibratory gyroscopes, there are different coupling and decoupling mechanisms employed by considering trade-off between the angular rate sensitivity and mechanical cross talk. Figure 2.1 shows three different actuation mechanisms. Figure 2.1-a shows a simple view of the coupled gyroscope mechanism, in which the drive, sense, and proof mass frames are directly connected to each other without any restriction at the movement of drive and sense frames. Therefore, they have a capability of 2-DOF (Degree-of-Freedom) movement, which results in a rate error signal at the output of the gyroscope in the presence of an undesired misalignment related with the drive mass and driving actuation force. Higher undesired mechanical cross talk is the main problem as a design challenge in the mechanical design of the coupled gyroscope, but they provide the maximum angular rate sensitivity without any loss when detecting the angular rotation as a rate. Figure 2.1-b shows the simple view of the decoupled gyroscope. Here, the motion of the drive frame restricted in a pre-determined drive axis direction has a movement capability of 1-DOF, but the sense has 2-DOF movement capability. The decoupled gyroscopes are highly insensitive to the undesired misalignment an actuation force related with the drive frame, but there still is a continuous movement not only in the direction of the sense axis but also in the direction of the drive axis at the sense frame, which leads to an undesired rate offset at the output of the gyroscope. Figure 2.1-c shows the simple view of the fully-decoupled gyroscope, in which the drive and sense frames are exactly orthogonal to each other and can move only along one direction (1-DOF). Therefore, the undesired mechanical crosstalk between the drive and sense modes can be totally eliminated in the absence of fabrication imperfections, but substantial loss in angular rate sensitivity is observed [39].

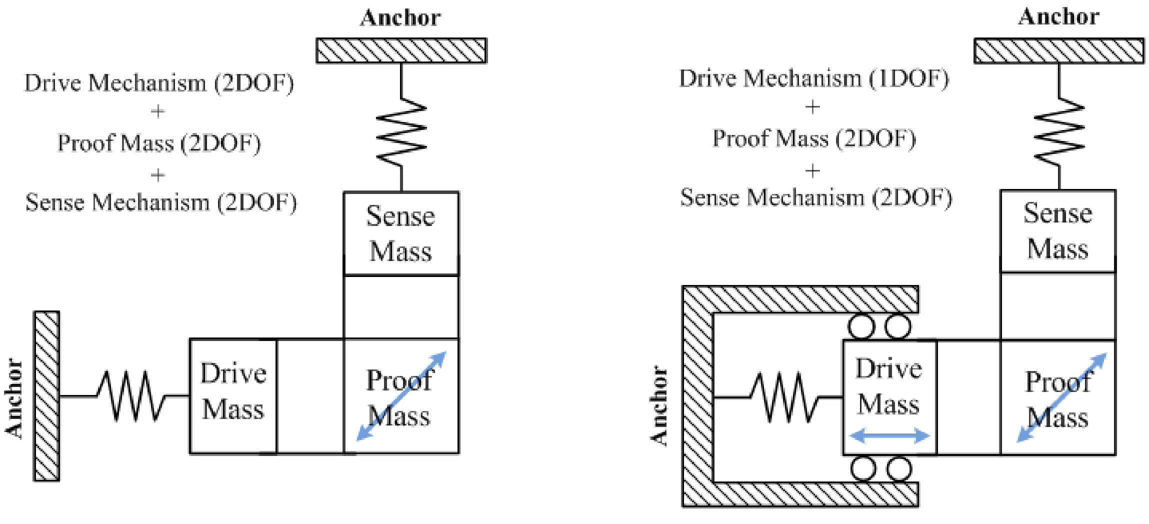

(a) (b)

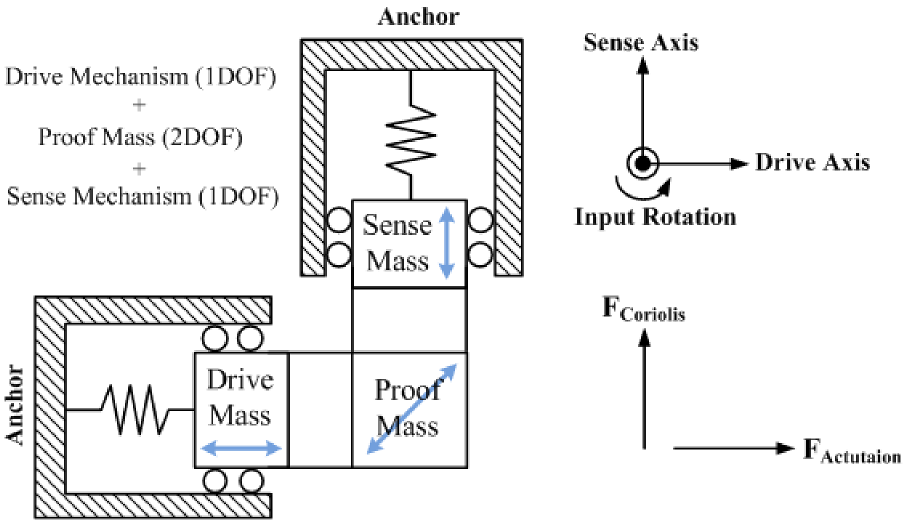

(c)

Figure 2.1: Three different actuation mechanisms rely on the coupling among the drive, proof mass, and sense frames in a gyroscope.

Figure 2.2 shows the simplified view of the fully-decoupled gyroscope studied in this thesis. Basically, the gyroscope consists of drive, proof mass, and sense frames. The drive and sense frames of the gyroscope have a capability of 1-DOF, whereas the proof mass frame enabling to transfer Coriolis acceleration to the sense frame has 2-DOF movement capability, as in Figure 2.1-c. The DOF movement capability is assigned to the drive, proof mass and sense frames by adjusting the rotational and linear stiffness of them with the aid of the springs and beams. In fact, the direct coupling between the drive and sense frames can be totally eliminated through the mechanical design of fully-decoupled gyroscope, but this cannot be achieved due to the fabrication imperfections. This undesired coupling causes a quadrature error at the system. The details of quadrature error will be given in Section 2.8.

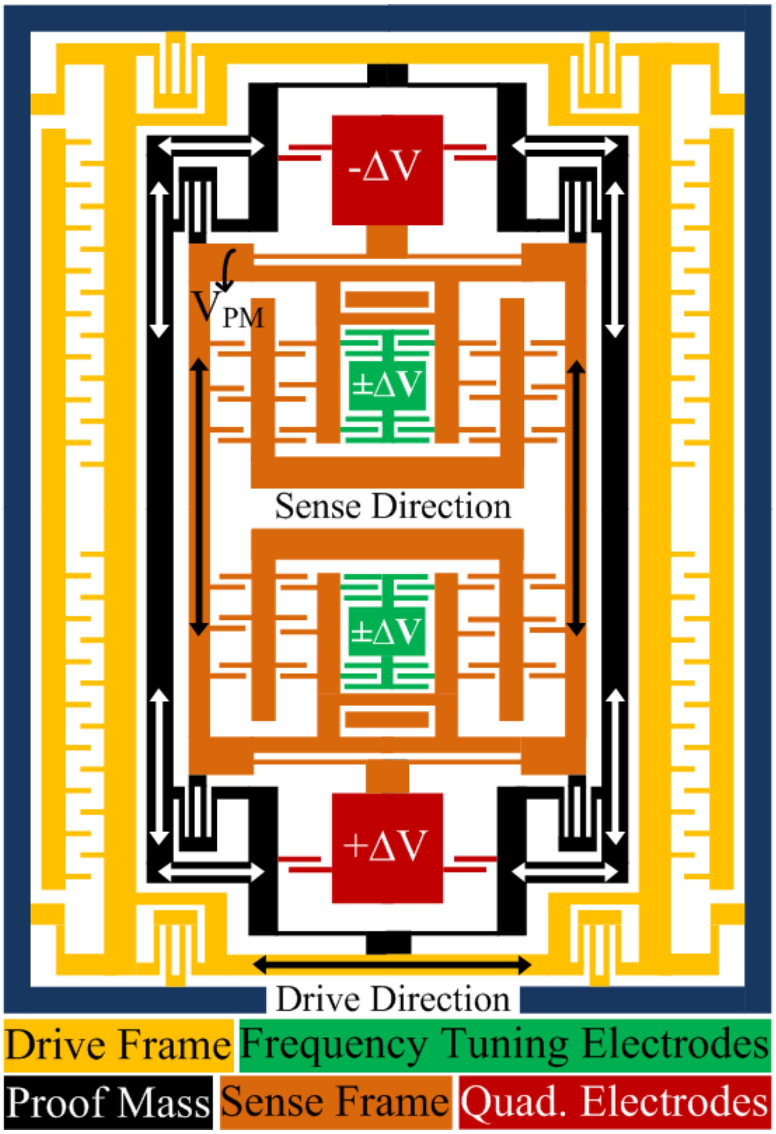

Figure 2.2: Simplified view of the fully-decoupled gyroscope studied in this thesis.

2.2 Vibratory Gyroscope Dynamics

Basically, a vibratory gyroscope consists of proof mass suspended by springs anchored to the rigid outer frame. The overall gyroscope structure can be represented by a 2-DOF mass-spring-damper system because the proof mass, which provides energy transfer caused by Coriolis acceleration to the sense mode, has a capability of movement at the direction of the drive and sense axes. Figure 2.3 shows the simple mass-damper-spring representation of the vibratory gyroscope. The gyroscope dynamics are deeply analyzed by separating the drive and sense mode dynamics for the simplicity.

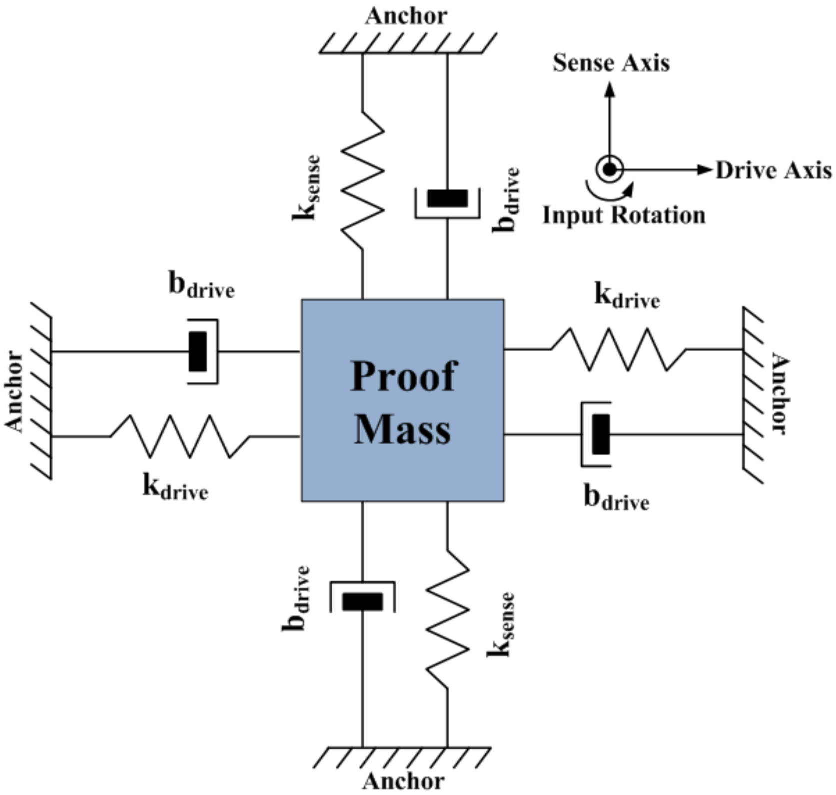

Figure 2.3: Simple mass-damper-spring representation of MEMS vibratory gyroscope.

2.2.1 Drive Mode Dynamics

The proof mass requires a continuous movement along the drive axis to generate a Coriolis acceleration in the presence of an angular rotation rate at the system. This continuous movement is provided to the proof mass by the drive mode of the gyroscope because these are directly coupled to each other by means of mechanical springs. During the gyroscope operation the drive mode is continuously vibrated by an electrostatic force to sustain continues movement at the proof mass frame. The drive mode dynamics are described by Newton’s second law due to the direct relation between the force and displacement at the drive mode of the gyroscope. The relationship between the force and displacement at the drive mode can be represented by the second order differential equation based on the characteristics of the mass-damper-spring system without considering other effects caused by misalignment at the proof mass due to fabrication imperfections as

$$f_D(t) = m_D\ddot{x}(t) + b_D\dot{x}(t) + k_D x(t) \qquad 2.1$$

where f_D is the actuation force applied to the drive mode of the gyroscope, x is the drive mode displacement, m_D is the mass of the drive mode including the drive and proof mass frame, b_D is the damping factor caused by gas surrounding the gyroscope structure, and finally, k_D is the spring constant related to the flexion elements in the drive mode. A time-varying electrostatic force resulting in a time-dependent drive displacement is required to achieve an oscillatory movement at the drive mode. The time domain equivalent expression of the force-displacement relation, shown in Equation 2.1, is converted to the frequency domain by using Laplace transform, and the resultant frequency domain expression of the force-displacement relation can be expressed as

$$F_D(s) = m_D s^2 X(s) + b_D s X(s) + k_D X(s) \qquad 2.2$$

Now, the direct relation between the force and displacement can be directly obtained by rearranging the terms in Equation 2.2, and it can be expressed in terms of the mechanical system parameters as

$$\frac{X_D(s)}{F_D(s)} = \frac{1/m_D}{s^2 + \frac{\omega_D}{Q_D}s + \omega_D^2} \qquad 2.3$$

In Equation 2.3, ω_D and Q_D are the resonance frequency and quality factor of the drive mode, and can be calculated by

$$\omega_D = \sqrt{\frac{k_D}{m_D}} \tag{2.4}$$

$$Q_D = \frac{\sqrt{k_D m_D}}{b_D} \tag{2.5}$$

The drive mode of the gyroscope is desired to oscillate at the drive mode resonance frequency to obtain the maximum drive displacement under the applied minimum force condition. When operating frequency of the drive actuation force is set to the drive mode resonance frequency, the force-displacement relation under the resonance condition by replacing the “s” term with “$j\omega_D$” in Equation 2.3 is simplified to

$$\frac{X_D(j\omega_D)}{F_D(J\omega_D)} = \frac{1/m_D}{j\frac{{\omega_D}^2}{Q_D}} = \frac{1}{j}\frac{Q_D}{k_D} \tag{2.6}$$

The equation above implies that when the drive mode is actuated under the mechanical resonance condition, there will be a phase shift of 90° observed between the actuation force and resultant drive displacement. The Equation 2.6 also states that the larger drive displacement can be obtained by increasing the quality of the resonance peak with the same actuation force because energy dissipation through the drive mode resonator is minimized when the drive mode of the gyroscope is operated with the highest possible gain described by the quality factor of the resonance peak.

2.2.2 Sense Mode Dynamics with Coriolis Effect

Since the mechanical structures of the drive and sense modes are similar with each other, the sense mode dynamics can be represented with the same second order differential equation as in Equation 2.1 by changing the subscript “$_{D}$” with “$_{S}$”, which are notations used to declare the mode name. The external electrostatic force used to establish the displacement in the drive mode is not required in the sense mode because it is desired to create a vibration at the sense mode by the self-induced fictitious forces, which are Coriolis, Radial (Centrifugal), and Tangential (Euler) forces. These forces are directly coupled to the sense mode though the proof mass and causes a deflection in the sense mode. These fictitious forces can be calculated considering the drive displacement along x-axis, the sense displacement along y-axis, and rotation along z-axis in [41] as

$$F_{Coriolis} = -2m_{PM}(\Omega_z \times \dot{X}) \tag{2.7}$$

$$F_{Tangential} = -m_{PM}(\dot{\Omega}_z \times X) \tag{2.8}$$

$$F_{Radial} = -m_{PM}\Omega_z \times (\Omega_z \times Y) \tag{2.9}$$

where m_{PM} is the mass of the proof mass frame, Ω_z is the applied angular rate input, $\dot{X}$ and X are the drive velocity and displacement, respectively, and Y is the sense mode displacement. The effect of the linear force along the sense axis caused by the radial force term can be mechanically eliminated with the use of two identical and fully differential sensing frames. Therefore, it is not taken into account in the modeling of the sense mode dynamics. If there is a time-invariant rotation applied to the system, the tangential force becomes zero. However, the Coriolis force always exists at the system in the presence of a time-varying or time-invariant rotation. Therefore, the Coriolis force establishes the main sensing principle idea behind the operation of the gyroscope. When the gyroscope is subjected to a angular rotation, the proof mass frame vibrates along the drive axis through the drive mode experiences Coriolis force that is orthogonal to both drive and rotation axis and is proportional to the amplitude of the angular rotation rate. Therefore, when there is a Coriolis force present at the system, the sense mode is started to vibrate along the sense axis. The most common case, in which time-varying rotation is applied to the system, is considered by analyzing the force-displacement relation in the sense mode. The relation between the sense mode displacement and fictitious forces can be presented as

$$-2m_{PM}\Omega_z(t) \times \dot{x}(t) - m_{PM}\dot{\Omega}_z(t) \times x(t) = m_S\ddot{y}(t) + b_S\dot{y}(t) + k_Sy(t) \qquad 2.10$$

In Equation 2.10, m_S is the total sense mass including proof mass and sense electrodes. Assuming the drive displacement at the drive mode resonance frequency induced by the time-varying electrostatic actuation force and angular rate input are taken as

$$x(t) = X_D \cos(\omega_D t) \qquad 2.11$$

$$\Omega_z(t) = \Omega_z \cos(\omega_z t) \qquad 2.12$$

where ω_z is the frequency of the applied angular rotation rate input. Inserting the terms in Equation 2.11 and 2.12 into Equation 2.10 and dividing both sides of Equation 2.10 by m_S, the force-displacement relation is rearranged as

$$\begin{aligned}&\frac{m_{PM}}{m_S}\Omega_z X_D\left[\left(\omega_D + \frac{\omega_z}{2}\right)\sin\big((\omega_D + \omega_z)t\big) + \left(\omega_D - \frac{\omega_z}{2}\right)\sin\big((\omega_D - \omega_z)t\big)\right] \\ &\qquad = \ddot{y}(t) + \frac{\omega_S}{Q_S}\dot{y}(t) + {\omega_S}^2 y(t)\end{aligned} \qquad 2.13$$

Equation 2.13 illustrates that the sense mode is actuated with two forces which are equally separated from ω_D in the frequency domain. The left-hand-side (LHS) of Equation 2.13 can be expressed by imaginary parts of the complex sinusoidal terms as

$$\text{LHS} = \frac{m_{PM}}{m_S}\Omega_z X_D Im\left[\left(\omega_D + \frac{\omega_z}{2}\right)e^{i(\omega_D+\omega_z)t} + \left(\omega_D - \frac{\omega_z}{2}\right)e^{i(\omega_D-\omega_z)t}\right] \qquad 2.14$$

Taking Fourier transform of both sides in Equation 2.13 by using Equation 2.14 for the LHS, the resultant equation can be expressed in the frequency domain, which enables to obtain the sense mode response.

$$\frac{m_{PM}}{m_S}\Omega_z X_D\left(\left(\omega_D+\frac{\omega_z}{2}\right)\delta(\omega-(\omega_D+\omega_z))+\left(\omega_D-\frac{\omega_z}{2}\right)\delta(\omega-(\omega_D+\omega_z))\right)$$

$$=Y(\omega)\left(-\omega^2+j\omega\frac{\omega_S}{Q_S}+{\omega_S}^2\right) \quad 2.15$$

In Equation 2.15, $\delta(\omega)$ is the impulse response. The sense mode response separated with regarding to frequency components is obtained through the simplification of Equation 2.15.

$$Y(\omega_D+\omega_z)=\frac{\frac{m_{PM}}{m_S}\Omega_z X_D\left(\omega_D+\frac{\omega_z}{2}\right)}{({\omega_S}^2-(\omega_D+\omega_z)^2)+j(\omega_D+\omega_z)\frac{\omega_S}{Q_S}} \quad 2.16\text{-a}$$

$$Y(\omega_D-\omega_z)=\frac{\frac{m_{PM}}{m_S}\Omega_z X_D\left(\omega_D-\frac{\omega_z}{2}\right)}{({\omega_S}^2-(\omega_D+\omega_z)^2)+j(\omega_D-\omega_z)\frac{\omega_S}{Q_S}} \quad 2.16\text{-b}$$

Equation 2.16-a implies that there are two components present at the sense frame in response to a sinusoidal angular rate input, having a frequency of ω_z. The sense mode response can be analyzed for two specific conditions, i.e. mode-matched and mismatched conditions, to get deep understanding of the sense mode response.

Assuming that the frequency (ω_z) of the angular rate input is zero, and the resonance mode frequencies of the gyroscope are exactly equal to each other, i.e., $\omega_D=\omega_S$, Equation 2.16-a can be simplified to

$$Y(\omega_D+\omega_z)+Y(\omega_D-\omega_z)\cong\frac{2\Omega_z X_D Q_S}{j\omega_D}\frac{m_{PM}}{m_S} \quad 2.17$$

Equation 2.17 indicates that when the resonance frequencies of the drive and sense modes are matched, the displacement at the sense mode is proportionally increases with the mechanical sense mode quality factor. This is the main motivation behind the mode-matching implementation, in which sensitivity of the sensor maximizes corresponding to the displacement of the sense mode thanks to the sense mode quality factor multiplication, which is around a few thousand at vacuum.

In the gyroscope operation, it is not necessary to perform mode-matching by exactly obtaining 0 Hz frequency split between the resonance modes. Now, it is required to decide the gyroscope operated under the mismatched or mode-matched condition. For a frequency mismatch and constant angular rate input ($\omega_z = 0$) condition, Equation 2.16-a can be represented as

$$Y(\omega_D + \omega_z) + Y(\omega_D - \omega_z) \cong \frac{2\Omega_z X_D \omega_D}{2\omega_D \Delta\omega - j\omega_D \frac{\omega_S}{Q_S}} \frac{m_{PM}}{m_S} \qquad 2.18$$

In Equation 2.18, $\Delta\omega$ is the frequency difference between the sense and drive modes. It is clearly observed that the condition needed to decide whether the gyroscope is operated under mode-matched condition or not can be derived from the denominator of Equation 2.18 as

$$\Delta f \ll \frac{f_S}{2Q_S} \qquad 2.19$$

where f_S/Q_S is the response bandwidth. When the condition in Equation 2.19 is satisfied, it is acceptable that the gyroscope is operated under the mode-matched condition as a rule of thumb. When the sense mode quality factor (Q_S) increases, the response bandwidth decreases. This is the main challenge in the mode-matching implementations. Another challenge is the phase characteristic of the sense mode which becomes sharper when Q_S increases. If the motivation of the mode-matching implementation is based on the phase relationship between the signals in a gyroscope at the system, the phase characteristic should also be taken into account when designing the mode-matching controllers.

The other gyroscope operation is mismatch operation which is satisfied in the condition of

$$\Delta f \gg \frac{f_S}{2Q_S} \tag{2.20}$$

Under the condition of Equation 2.20, the sense mode displacement is obtained in response to a constant angular rotation rate input as

$$Y(\omega_D + \omega_z) + Y(\omega_D - \omega_z) \cong \frac{\Omega_z X_D}{\Delta\omega} \frac{m_{PM}}{m_S} \tag{2.21}$$

The sensitivity corresponding to the sense mode displacement is significantly decreases under the mismatched condition compared to the mode-matched condition as expected. Therefore, it is not desired to operate the gyroscope under the mismatched condition. Finally, it should also be noticed that there are no phase difference between the drive and sense modes in the mismatched gyroscope operation, but the phase difference of 90° exists between these modes at the mode-matched condition. In the content of thesis, mode-matching have been performed by utilizing the phase relationship between the drive and quadrature signals. As a rule of thumb, there are always 90° phase difference exists between the sense mode and quadrature signals at the gyroscope operation. In the design stage of the gyroscope, the drive and sense mode resonance frequencies are adjusted to be matched, but these are not match after the fabrication due to the fabrication imperfections, so mode-matching operation is started in the mismatched condition. Then, it goes into the matched condition by tuning the sense mode resonance frequency. Therefore, the phase variation at the sense mode output of the gyroscope is taken into account as a key factor in the design stage of the mode matching controllers.

2.3 Design of MEMS Vibratory Gyroscope and Extraction of Model Parameters

Model parameters are basically required to identify the mode dynamics of the gyroscope, discussed in Section 2.1. Basically, these parameters can be extracted by using the spring constants, mass of the frames, and damping factor, which are discussed in the following subsections.

2.3.1 Mechanical Spring Design

Mechanical spring constants are used to determine the drive and sense mode resonance frequencies of the gyroscope. There are mainly three types springs used for connecting the drive, proof mass, and sense frames. The double-folded and half-folded spring structures are used in the drive mode because they enable large displacement without sacrificing linearity, which is the main concern in the drive mode. However, linearity is not the case for the sense mode because it vibrates only a few angstroms. The clamped-guided-end springs are used in the sense mode considering the area covered by springs. The detailed information about the spring design and spring constant calculation can be found in [41].

2.3.2 Mass and Damping Factor Estimation

The mass of the frames is crucial for adjusting the modal frequencies of the micromachined vibratory gyroscope and determining the mechanical Brownian noise of the gyroscope which is the maximum level that the performance improvement in the system may converge. Mass of the frames can be calculated by using the well-known expression

$$m = Vd \qquad 2.22$$

Where d is the density of the material used to construct the sensor, and V is the volume that can be directly found from the geometry of the structure.

It is quite difficult to estimate the damping factor with hand calculation because there is a complicated analysis required to calculate the damping factor. Therefore, the damping factor is experimentally determined by using Equation 2.5.

2.4 Electrostatic Actuation Mechanism Using Parallel Plate Capacitor

Basically, a parallel plate capacitor consisting of two isolated conductors is used to generate an electrostatic force required for actuation. Figure 2.4 shows the parallel plate capacitor structure used for actuation in the gyroscope. When the different bias potentials having different polarity are applied to the movable and stationary conductors, the energy is stored between the parallel plates due to charge accumulation on the plates. The stored energy causing a pulling electrostatic force between the parallel plates is converted to a current through the displacement of the movable conductor. This is the main idea behind the working principle of the capacitive based sensors.

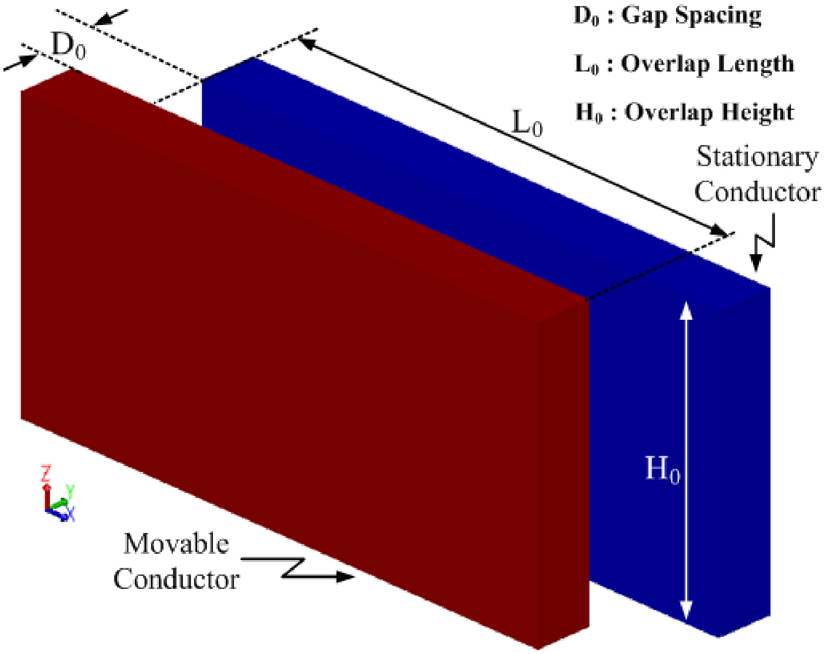

Figure 2.4: Parallel plate capacitor structure used for actuation in the gyroscope.

The capacitance between the parallel plates in Figure 2.4 is calculated through

$$C = \alpha\varepsilon_0 \frac{L(x)H(z)}{D(y)} \tag{2.23-a}$$

Where

$$L(x) = L_0 + x \tag{2.23-b}$$

$$H(z) = H_0 - z \tag{2.23-c}$$

$$D(y) = D_0 - y \tag{2.23-d}$$

In Equation 2.23, α is the parameter coming from the fringing field effect which is taken as a constant in the calculations by ignoring the slight variation of it corresponding to movable conductor displacement for the simplicity, ε_0 is the permittivity of free space. The well-known expression of the stored energy inside the capacitor is

$$E_{stored} = \frac{1}{2}CV^2 \tag{2.24}$$

where V is the difference between the applied potentials to the conductors. The acting electrostatic force on parallel plates of the capacitor can be obtained by taking the derivative of the stored energy with respect to the $x - y - z$ directions as

$$F_{e,x} = \frac{\partial E_{stored}}{\partial x} = \frac{1}{2}\frac{\partial C}{\partial x}V^2 = \frac{1}{2}\alpha\varepsilon_0 \frac{H_0}{D_0}V^2 \tag{2.25-a}$$

$$F_{e,y} = \frac{\partial E_{stored}}{\partial y} = \frac{1}{2}\frac{\partial C}{\partial y}V^2 = \frac{1}{2}\alpha\varepsilon_0 \frac{H_0 L_0}{(D_0 - y)^2}V^2 \tag{2.25-b}$$

$$F_{e,z} = \frac{\partial E_{stored}}{\partial z} = \frac{1}{2}\frac{\partial C}{\partial y}V^2 = -\frac{1}{2}\alpha\varepsilon_0\frac{L_0}{D_0}V^2 \qquad 2.25\text{-c}$$

It can be understood from the sign of the generated electrostatic forces that they try to increase the stored energy by pulling the movable plate toward the stationary plate that enhances the capacitance between the plates. Another observation is that the electrostatic forces in x and z directions are independent from the displacement, but the generated electrostatic force in y direction shows a nonlinear behavior depending on the movable plate displacement, and the amplitude of it, providing that D_0 is smaller than L_0 and H_0, compared to the generated electrostatic forces in x and z directions is higher.

In the light of analysis of the generated forces, shown in Equation 2.25-a, the varying overlap area type capacitors are used to construct the drive mode actuation mechanism because they provide a capability of a large displacement required to reduce the noise floor at the system without degrading linearity. Figure 2.5 shows the varying-overlap area type capacitors used to construct the drive mode actuation mechanism.

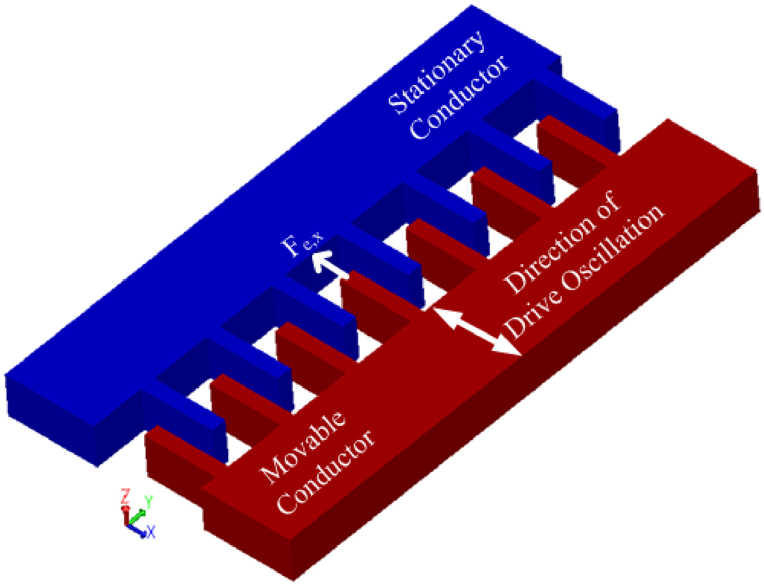

Figure 2.5: Varying-overlap area type capacitors used to construct the drive mode actuation mechanism.

In the drive mode of the gyroscope, there is a continuous movement required to establish the Coriolis coupling between the resonance modes of the gyroscope, discussed in Section 2.1. Therefore, the oscillation at the mechanical resonance frequency of the drive mode is constructed by creating a time-varying potential difference between the movable and stationary conductors. The potential difference is established by applying a fixed potential (V_{DC}) to the movable conductor and a time-varying excitation signal to the stationary conductor. The generated force in x direction can be expressed as

$$F_{e,x} = \frac{1}{2}\frac{\partial C}{\partial x}(V_{DC} + V_{ac}sin(wt))^2 \qquad 2.26$$

where V_{DC} is the fixed DC potential applied to the gyroscope as a proof mass potential, and V_{ac} is the amplitude of the AC excitation signal. Rearranging the terms in Equation 2.26 yields

$$F_{e,x} = \frac{1}{2}\frac{\partial C}{\partial x}\left\{V_{DC}^2 + \frac{V_{ac}^2}{2} + 2V_{DC}V_{ac}\,sin(wt) + \frac{1}{2}V_{ac}^2 cos(2wt)\right\} \qquad 2.27$$

In Equation 2.27, the electrostatic force along x direction has three components presented at DC and frequencies of w and $2w$. The component at w is used to excite the drive mode at its mechanical resonance frequency, and other components are rejected through the drive mode resonator, which behaves like a sharp band-pass filer due to the high quality factor under vacuum condition.

In the design of the sense mode, the varying-gap type capacitors are used to get higher capacitive sensitivity which is required to detect small displacements caused by angular rotation, but the nonlinear behavior of them is the main challenge, shown in Equation 2.25-b. The nonlinearity in the varying-gap capacitors can be minimized to a certain point around zero by satisfying the specific condition of $y \ll D_0$. This condition is satisfied in the sense mode of the gyroscope, in which the displacement caused by an angular rotation input is a few angstroms. The amount of the sense mode displacement is too small when compared it with the amount of the capacitive gap. Figure 2.6 shows the varying-gap type capacitors used to construct the sense mode actuation mechanism.

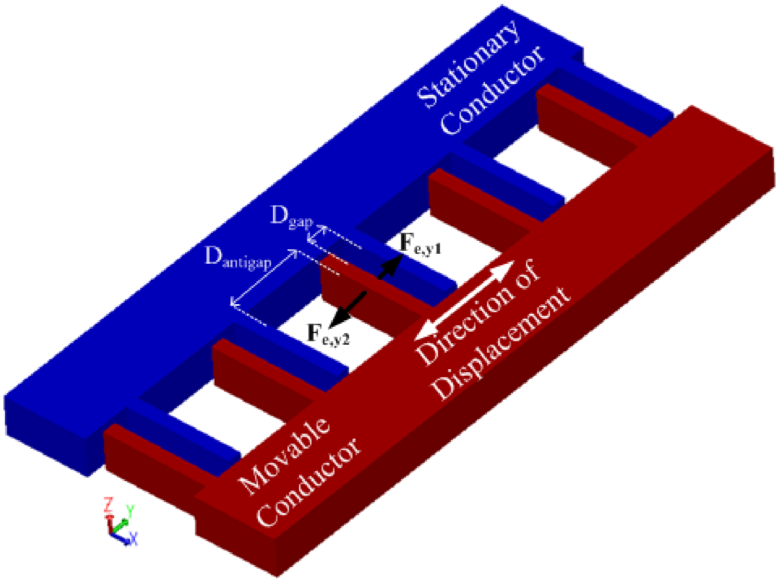

Figure 2.6: Varying-gap type capacitors used to construct the sense mode actuation mechanism.

The electrostatic forces of $F_{e,y1}$ and $F_{e,y2}$ are used to find a net acting force on a single movable finger. The antigap distance, shown in Figure 2.6, is arranged to be higher than the gap distance to decrease the effect of $F_{e,y2}$. The net acting electrostatic force onto the movable conductor can be described as

$$F_{y,net} = F_{e,y1} - F_{e,y2} = \frac{1}{2} N \alpha \varepsilon_0 H_0 L_0 \left(\frac{1}{\left(D_{gap} - y\right)^2} - \frac{1}{\left(D_{antigap} + y\right)^2} \right) V^2 \qquad 2.28$$

where N is the number of capacitance pairs used in the sense mode of the gyroscope.

2.5 Capacitive Sensing Mechanism

Basically, the capacitive sensing mechanism is used for converting the physical displacement at capacitance pairs of the mechanical sensor to a voltage. In the system, there are two signals, drive and sense, required to be obtained through the capacitive sensing mechanism. The drive signal is used as a carrier signal in all of the modulation and demodulation steps at the gyroscope operation. The sense signal provides information about the angular rotation rate. In the capacitive sensing mechanism, first the current is obtained, and then the obtained current is converted to a voltage through the readout electronics, which will be discussed in Section 3.1. The general expression of the current flowing through a capacitor can be expressed as

$$I_{out}(t) = \frac{\partial Q(t)}{\partial \mathrm{t}} = \frac{\partial (C(t)V(t))}{\partial \mathrm{t}} = C(t)\frac{\partial V(t)}{\partial t} + V(t)\frac{\partial C(t)}{\partial \mathrm{t}} \qquad 2.29$$

For the actual gyroscope operation, $C(t)$ and $V(t)$ can be expressed as

$$V(t) = V_{DC} + V_{ac}(t) \qquad 2.30\text{-a}$$

$$C(t) = C_0 + \frac{\partial C(t)}{\partial x}x(t) \qquad 2.30\text{-b}$$

In Equation 2.30-a, V_{DC} is the fixed proof mass potential which is used to create a potential difference between the capacitor plates in the gyroscope, $V_{ac}(t)$ is a time-varying signal resulted from the displacement of sensing capacitors. At the gyroscope operation, $V_{ac}(t)$ is much smaller than V_{DC}. Therefore, it can be ignored. In Equation 2.30-b, C_0 is static capacitance, $\partial C(t)/\partial x$ represents the capacitance change with respect to the displacement, and $x(t)$ refers to the time-varying displacement. Inserting the terms in Equation 2.30 into Equation 2.29, the sensor output current can be found as

$$I_{out}(t) \cong V_{PM}\frac{\partial C(t)}{\partial \mathrm{t}} = V_{PM}\frac{\partial C(t)}{\partial x}\frac{\partial x(t)}{\partial t} \qquad 2.31$$

Equation 2.31 can be expressed in the frequency domain which is mostly used by modeling controllers of the mode-matching system as

$$I_{out}(j\omega) \cong V_{PM}\frac{\partial C(t)}{\partial x}\mathrm{j\omega X(j\omega)} \qquad 2.32$$

2.6 Electrostatic Spring Effect

The main motivation behind the mechanical design of the gyroscope is to achieve 0 Hz frequency split between the resonance modes, called mode-matching. When the resonance modes are perfectly matched, there is an improvement in the performance of the gyroscope during the gyroscope operation due to an increase in sensitivity of the sensor. In the mechanical design of the gyroscope, the resonance frequencies of the drive and sense modes are adjusted to be matched by characterizing the mode frequencies through springs, but it is quite difficult to obtain the desired mode frequencies after fabrication due to fabrication imperfections. The width of the springs cannot be fabricated better than a fabrication tolerance of 10% by using the current standard micromachining technology, which causes a shift higher than 10% at the resonance mode frequencies of the gyroscope, but the amount of shift cannot be the same for the resonance modes due to the non-uniformity in the fabrication. Therefore, the post-processing is required to mechanically tune the mode frequencies in the gyroscope, but methods used for post-processing are not reliable in terms of the long term stability, time, and cost. Instead, the tuning of the resonance mode frequencies in the gyroscope can be electronically achieved with the aid of the varying-gap type capacitors. In the design of the gyroscope, the sense mode is constructed by the varying-gap type capacitors, shown in Figure 2.6, to provide electrostatic tuning capability. The tuning in the sense mode of the gyroscope is accomplished through the electrostatic spring constant which can be expressed by taking the derivative of electrostatic force in Equation 2.28 with respect to the position as

$$\delta k_{electrostatic} = \frac{\partial \mathrm{F}_{e,y}}{\partial \mathrm{y}} = \alpha \varepsilon_0 H_0 L_0 \left(\frac{1}{\left(D_{gap} - y\right)^3} + \frac{1}{\left(D_{antigap} + y\right)^3} \right) V^2 \qquad 2.33$$

It is noteworthy that the electrostatic spring constant depends on the displacement between the capacitor plates with a cubic relation. If the displacement is large, an error in the estimation of the constant electrostatic spring constant will be observed due to the time-varying displacement. The displacement arises from an AC excitation force is kept as small as possible in the sense mode by providing a large DC potential difference across the parallel plates of the capacitor. Therefore, the electrostatic spring constant is assumed to be constant during the gyroscope operation. In the mechanical design of the gyroscope, the sense mode resonance frequency is designed to be higher than the drive mode resonance frequency because it can be only used to soften the effective spring constant in the sense mode of the gyroscope. The effective spring constant is equal to

$$k_{eff} = k_{mech} - \delta k_{electrostatic}$$

$$= k_{mech} - N\alpha\varepsilon_0 H_0 L_0 \left(\frac{1}{\left(D_{gap} - y\right)^3} + \frac{1}{\left(D_{antigap} + y\right)^3} \right) V^2 \qquad 2.34$$

where k_{mech} is the mechanical spring constant and N is the number of the capacitive pairs used in the sense mode. The sense mode resonance frequency can be expressed in terms of the effective spring constant as

$$w_S = \sqrt{\frac{k_{eff}}{m_S}} = \sqrt{\frac{k_{mech} - N\alpha\varepsilon_0 H_0 L_0 \left(\frac{1}{\left(D_{gap} - y\right)^3} - \frac{1}{\left(D_{antigap} + y\right)^3} \right) V^2}{m_S}} \qquad 2.35$$

When tuning the sense mode resonance frequency, it should be noticed that if the potential differences exceeds a critical point, the movable plate of the capacitor collapses onto the stationary plate, which is called pull-in. The static pull-in voltage can be found by equating the mechanical spring constant (k_{mech}) to the electrostatic spring constant ($\delta k_{electrostatic}$). It is expressed in [39] as

$$V_{pullin} = \sqrt{\frac{8 k_S D_{gap}}{27 \alpha \varepsilon_0 H_0 L_0}} \qquad 2.36$$

2.7 Design of Frequency Tuning Electrodes

In the scope of this thesis, there are mainly two approaches used to accomplish mode-matching. In the first approach, the sense mode resonance frequency is tuned with respect to the drive mode resonance frequency by changing the proof mass potential, which provides the effect of softening on the springs of the sense mode discussed above. In the second approach, the frequency matching between the modes of the gyroscope is performed through the frequency tuning electrodes by using the electrostatic tuning capability of the sense mode. The main motivation behind the design of the frequency tuning electrodes is to achieve mode-matching without changing the proof mass potential. Since the proof mass potential is used for constructing a potential difference across the capacitor plates in the gyroscope, the overall system dynamics are directly affected from a change in the proof mass potential. However, the frequency tuning electrodes only affects the sense mode dynamics at the system because they are only used for tuning purpose in the gyroscope. Figure 2.7 shows the configuration of the frequency tuning electrodes.

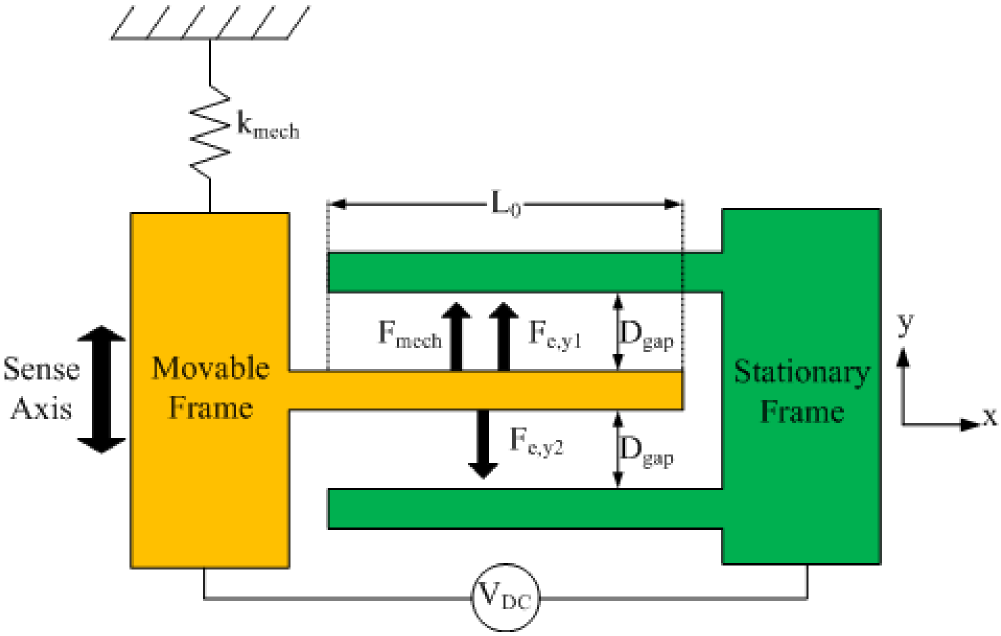

Figure 2.7: Configuration of the frequency tuning electrodes.

At the design stage, the gap, D_{gap}, between the capacitor plates is kept same in the frequency tuning electrodes compared to the electrode structure used in the sense mode, shown in Figure 2.6, to increase the effectiveness of the tuning capability and equalize the generated electrostatic force on the movable frame electrodes. Considering Figure 2.7, there are three dominant forces acting on the movable frame which represents the sense mode frame. These forces, which are the mechanical force caused by the springs in the sense frame, and the electrostatic forces caused by the capacitor plates that is formed by using the sense frame electrodes and frequency tuning electrodes that is represented by the stationary frame in Figure 2.7, can be calculated considering the coordinate frame as

$$F_{mech} = k_{mech} y \qquad 2.37\text{-a}$$

$$F_{e,y1} = \frac{1}{2} \frac{\alpha \varepsilon_0 H_0 L_0}{\left(D_{gap} - y\right)^2} {V_{DC}}^2 \qquad 2.37\text{-b}$$

$$F_{e,y2} = \frac{1}{2} \frac{\alpha \varepsilon_0 H_0 L_0}{\left(D_{gap} + y\right)^2} {V_{DC}}^2 \qquad 2.37\text{-c}$$

In Equation 2.37, V_{DC} is the potential difference across the capacitor plates, and y is the displacement amount on the movable frame, respectively. Total force acting on the sense frame is equal to

$$F_{total} = F_{mech} + F_{e,y1} - F_{e,y2} = k_{eff} y \qquad 2.38$$

where k_{eff} is the effective spring constant in a sense mode. Taking the derivative of the total force in Equation 2.38 with respect to the y position k_{eff} can be expressed as

$$k_{eff} = k_{mech} - \delta k_{electrostatic,1} - \delta k_{electrostatic,2}$$

$$= k_{mech} - \alpha \varepsilon_0 H_0 L_0 \left(\frac{1}{\left(D_{gap} - y\right)^3} + \frac{1}{\left(D_{gap} + y\right)^3} \right) {V_{DC}}^2 \qquad 2.39$$

Equation 2.39 states that the electrostatic spring constants, proportional with square of the potential difference across the capacitor plates, resulting from the electrostatic forces, $F_{e,y1}$ and $F_{e,y2}$, provide softening effect on the mechanical spring constant in the sense mode. The sense mode resonance frequency can be tuned through the frequency tuning electrodes as

$$w_S = \sqrt{\frac{k_{eff}}{m_S}} = \sqrt{\frac{k_{mech} - \alpha \varepsilon_0 H_0 L_0 \left(\frac{1}{\left(D_{gap} - y\right)^3} + \frac{1}{\left(D_{gap} + y\right)^3} \right) {V_{DC}}^2}{m_S}} \qquad 2.40$$

Figure 2.8 shows the simplified structure of the single-mass fully-decoupled gyroscope including the frequency tuning electrodes which is designed and placed in the layout to achieve the frequency matching condition. To better understand the use of frequency tuning electrodes in the mode-matching system, the actual gyroscope operation should be realized. In the actual operation of the gyroscope, there is a proof mass potential always provided to the gyroscope because it is necessary for the actuation and detection in the gyroscope. However, the proof mass potential causes a shift in the sense mode resonance frequency due to the electrostatic spring effect. Therefore, the softening effect of the proof mass potential on the mechanical spring constant is taken into account in the mechanical design of the frequency tuning electrodes because the frequency tuning electrodes provide a tuning of the sense mode resonance frequency in a limited frequency range that is determined by the amplitude of the applied potential, $\pm \Delta V$, to the frequency tuning electrodes and number of them. In the actual gyroscope operation, the sense mode resonance frequency can be expressed considering the effect of varying gap type capacitors in the sense mode and frequency tuning electrodes as

$$w_S = \sqrt{\frac{k_{eff}}{m_S}} =$$

$$\sqrt{\frac{k_{mech} - N_1\left(\frac{\alpha\varepsilon_0 H_0 L_0}{(D_{gap}-y)^3} + \frac{\alpha\varepsilon_0 H_0 L_0}{(D_{antigap}+y)^3}\right){V_{PM}}^2 - N_2\left(\frac{\alpha\varepsilon_0 H_0 L_0}{(D_{gap}-y)^3} + \frac{\alpha\varepsilon_0 H_0 L_0}{(D_{gap}+y)^3}\right)(V_{PM} \pm \Delta V)^2}{m_S}} \qquad 2.41$$

where N_1 represents the number of capacitive pairs in the sense mode, N_2 represents the number of frequency tuning electrodes, $V_{PM}$is the proof mass potential, ΔV is the tuning potential applied to the frequency tuning electrodes.

Figure 2.8: Simplified structure of the single-mass fully-decoupled gyroscope including the frequency tuning electrodes placed in the layout to achieve mode-matching.

2.8 Quadrature Error and Its Cancellation

The mechanical spring imbalances occurred due to fabrication imperfections leads to a substantial error signal, called quadrature error, at the output of the gyroscope, common for all capacitive micromachined gyroscopes fabricated using the current standard micromachining technology [4]. Figure 2.9 shows the conceptual view of the quadrature error induced by misalignment of the proof mass frame of the gyroscope. Figure 2.9-a shows an ideal gyroscope, in which there is no mechanical coupling occurred between the drive and sense modes because the proof mass is restricted to vibrate along the drive axis in response to the drive mode excitation and only along the sense axis in response to Coriolis force induced by an angular rotation rate through the mechanical design. However, it cannot be possible to fabricate the drive and sense axis in the gyroscope as orthogonal to each other due to the fabrication imperfections. Figure 2.9-b shows the fabricated gyroscope, in which there is a mechanical coupling occurred between the drive and sense modes due to the misalignment at the proof mass frame vibrated at an angle ϴ from the designed drive axis. This alignment error at the proof mass frame causes an offset, which is known as zero-rate output (ZRO), at the output of the gyroscope in the absence of an angular rotation rate.

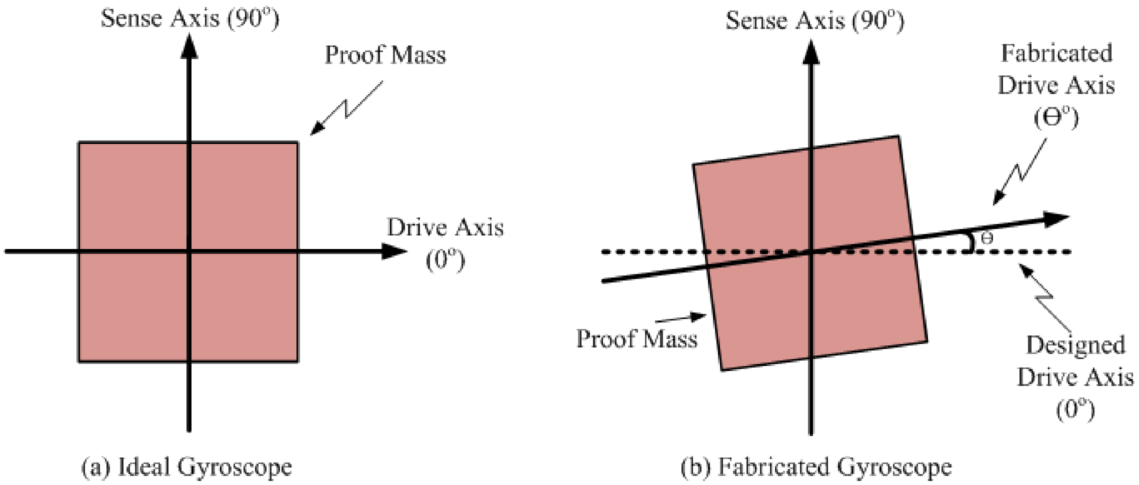

Figure 2.9: Conceptual view of the quadrature error induced by misalignment of the proof mass frame of the gyroscope.

The misalignment at the proof mass causes an oscillatory displacement at the sense mode output of the gyroscope due to the mechanical crosstalk between the drive and sense modes. This oscillatory displacement detected along the sense axis caused by the quadrature error can be expressed considering the proof mass shown in Figure 2.9-b as

$$y_{quadrature}(t) = kX_D \cos(\omega_D t) \qquad 2.42$$

where k is the mechanical coupling ratio of the drive displacement to the sense axis depending on the angle of ϴ, shown in Figure 2.9-b. Equation 2.42 states that the quadrature signal is directly proportional to the sinusoidal drive excitation signal, $X_D \cos(\omega_D t)$, where X_D stands for the amplitude of the drive displacement. However, the displacement induced by Coriolis force is directly proportional to the velocity of the drive displacement. Therefore, there is a phase difference of 90° that always exists between the quadrature and Coriolis induced sense mode signals. In the Coriolis induced sense mode signal detection, this phase difference is used to reject the quadrature error signal at the output of the gyroscope by utilizing the phase sensitive demodulation technique.

The quadrature error is coupled to the sense mode of the gyroscope at the drive mode resonance frequency, shown in Equation 2.42. Therefore, when the gyroscope's mode frequencies are matched, the quadrature error signal maximizes, which results in saturation of all controller blocks except the drive mode controller. Therefore, it is necessary to cancel the quadrature error to achieve the mode-matched gyroscope operation. It should be also noticed that when the gyroscope is operated under the mode-matched condition, there is a 90° shift that occurs in the phase of the Coriolis induced sense mode and quadrature signals compared to the mismatch operation.

In the gyroscopes studied in this study, the quadrature error is cancelled through the dedicated electrode structures containing parallel plate capacitors, which are placed on the proof mass to apply electrostatic forces at the corners of the proof mass frame, shown in Figure 2.8. The applied electrostatic forces generated by applying differential potentials to the quadrature cancellation electrodes provide a rotational movement at the proof mass frame. Thus, the misalignment at the proof mass is corrected with the aid of the electrostatic forces that enables a clockwise or counter clockwise rotation on the proof mass frame. The details of the quadrature cancellation mechanism with the electromechanical modeling can be found in [39].

2.9 Finite-Element Simulations

Finite-element method (FEM) is the well-known computational based simulation method that enables us to analyze the behavior of the complex systems, such as mechanical, thermal/fluidic, electromagnetic systems. In this study, FEM is used to analyze the mechanical behavior of the vibratory gyroscope. Coventorware, which is the simulation program that is suited to analyze MEMS devices with a high accuracy, is used to perform FEM simulations. Mode shapes and their modal frequencies of the MEMS vibratory gyroscope studied in this work are extracted through the FEM simulations.

2.9.1 Modal Analysis

Modal analysis is performed to identify the mode shapes and their modal frequencies of the gyroscope. The drive and sense mode resonance frequencies of the gyroscope are adjusted with hand-calculation during the design, but it is quite difficult to determine the frequencies of higher order modes, such as out-of-plane and rotary modes, with hand-calculation during the design. Therefore, the higher order modes should be identified through the modal analysis to perform the safe gyroscope operation. For the gyroscope operation, it is desired that the drive and sense mode resonance frequencies of the gyroscope should be kept minimally two times lower than frequencies of the undesired modes because they results in an increase of the mechanical coupling between the drive and sense modes.

Modal analysis has been performed for the first 10 modes. Table 2.1 shows the whole frequency list of the simulated resonance modes of the single-mass fully decoupled gyroscope designed in this work, in which the first two represents the drive and sense mode resonance frequencies of the gyroscope, and the third and fourth mode represents the higher parasitic mode frequencies which are considered during the design because they have an ability to affect the gyroscope operation by resulting in spurious vibrations compared to other higher order modes. As can be seen from Table 2.1, the resonance frequencies of the higher order modes are kept two times higher than the drive and sense mode resonance frequencies to ensure proper gyroscope operation.

Table 2.1: Whole frequency list of the simulated resonance modes of the single-mass fully decoupled gyroscope designed in this work.

Mode #	Resonance Frequency (Hz)	Generalized Mass (kg)
1	14814.67	1.024e-7
2	16384.34	8.044e-8
3	32268.40	3.317e-8
4	35230.76	2.522e-8
5	39168.53	1.014e-8
6	39706.77	2.222e-8
7	42240.93	6.095e-9
8	42830.55	6.613e-9
9	44787.92	2.122e-8
10	51278.73	2.201e-8

Figure 2.10 shows the drive and sense mode shapes of the single-mass fully-decoupled gyroscope. Figure 2.11 shows the related higher order mode shapes for the single-mass fully-decoupled gyroscope.

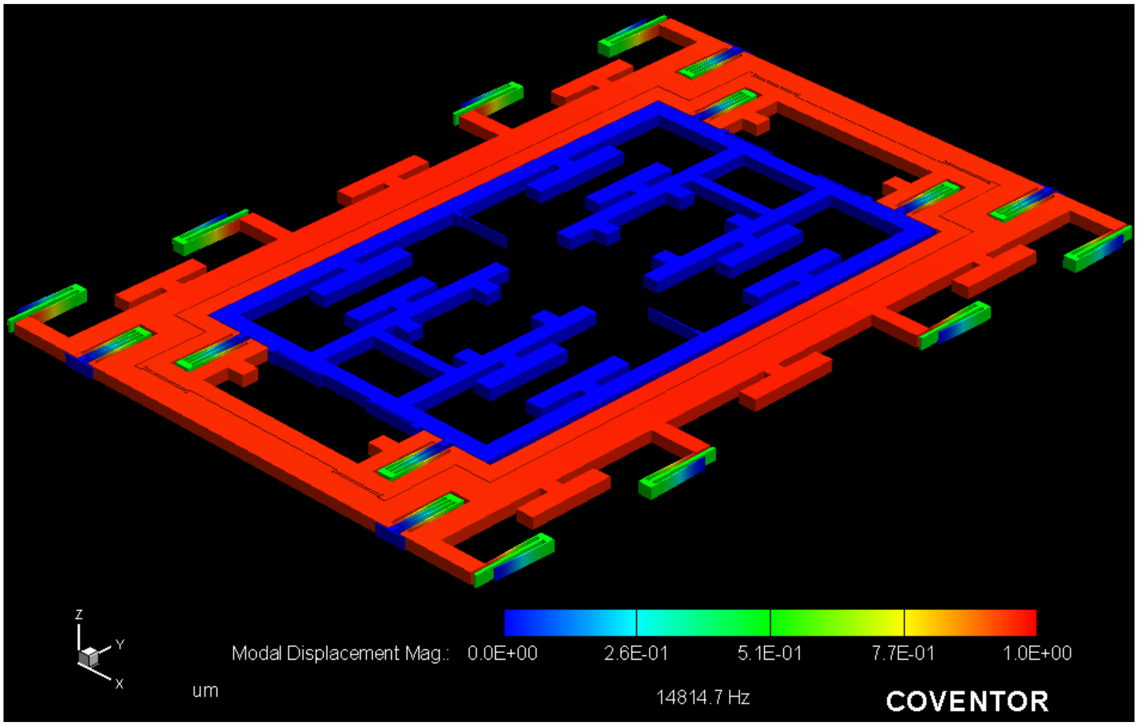

(a)

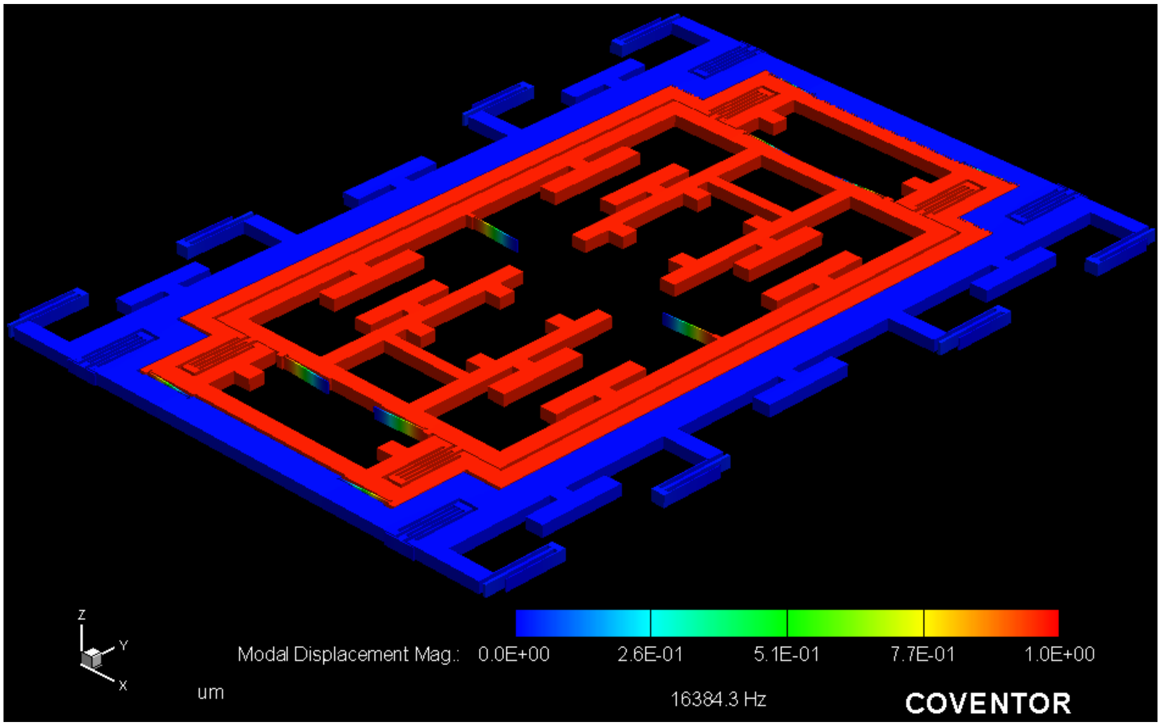

(b)

Figure 2.10: Mode shapes for (a) the drive and (b) sense modes of the single-mass fully-decoupled gyroscope.

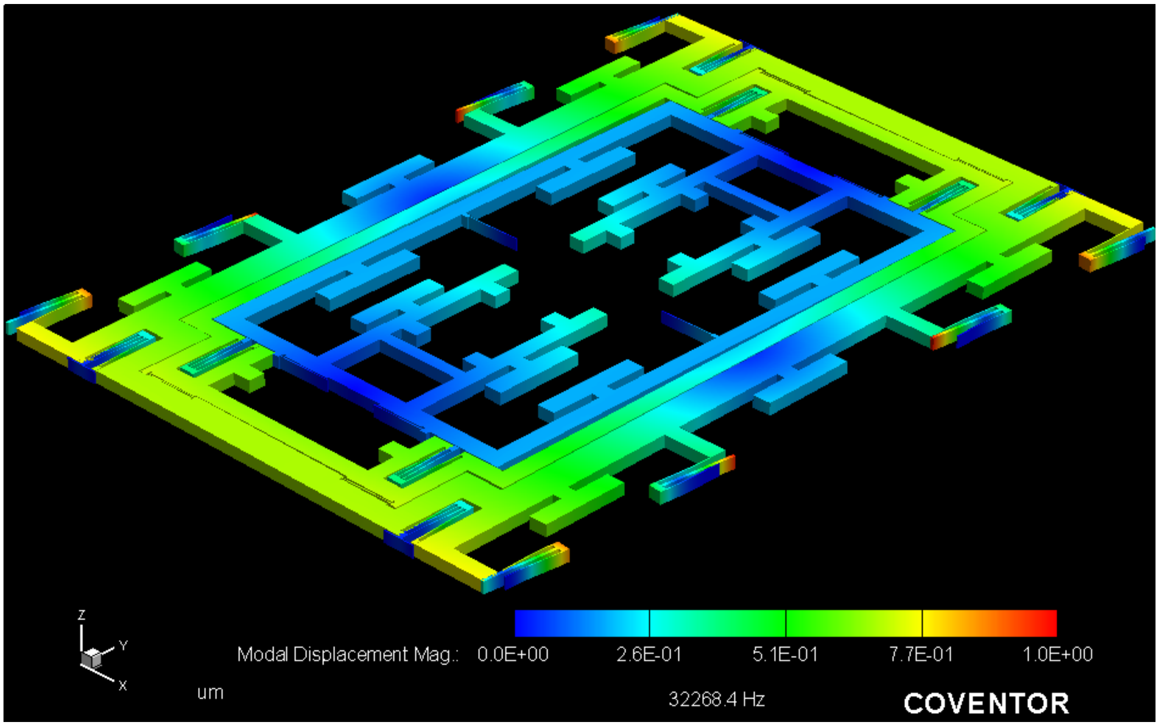

(a)

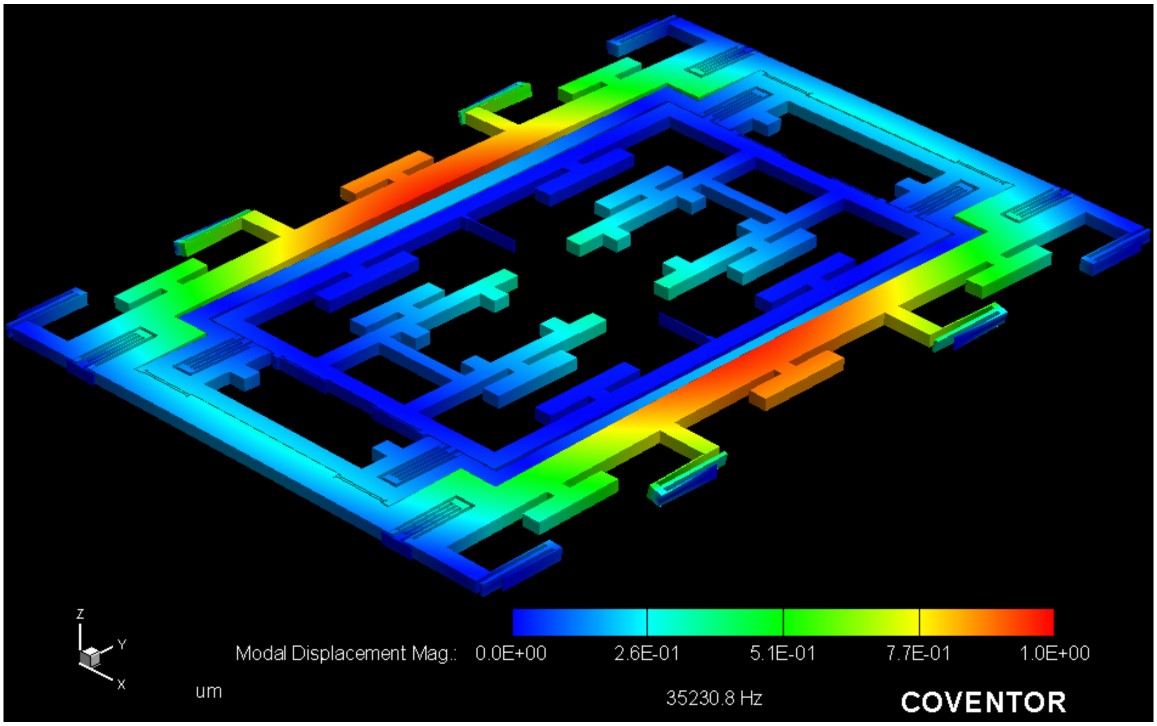

(b)

Figure 2.11: Related higher order mode shapes for the single-mass fully-decoupled gyroscope. (a) Rotary mode. (b) Out-of-plane mode.

2.10 Summary

This chapter provides information about the theory behind the electromechanical design of the MEMS vibratory gyroscopes studied in this thesis. First, the mechanics of the proposed vibratory gyroscopes are modeled. Then, the dynamics of the primary resonance modes, in which the sense mode dynamics are deeply investigated for the mismatched and mode-matched gyroscope operations in the presence of a Coriolis force, are described for the proposed fully-decoupled vibratory gyroscope. Third, the estimation of the spring constant, mass, and damping factor are briefly explained. Next, the actuation and capacitive sensing mechanisms are demonstrated with the idea behind them. The electrostatic spring constant effect used for the resonance frequency tuning in the gyroscope is also examined to understand how mode-matching is achieved. Then, the design of the frequency tuning electrodes used for matching of the sense mode resonance frequency to the drive mode resonance frequency is presented. Following, the definition of quadrature error and its cancellation mechanism are briefly discussed. Finally, FEM simulations are performed to determine the mode shapes and their modal resonance frequencies of the designed single-mass fully decoupled gyroscope.

CHAPTER 3

ELECTRONIC CONTROLLER DESIGN FOR MEMS GYROSCOPES

This chapter presents the details of an electronic controller design for MEMS vibratory gyroscopes studied in this thesis. Section 3.1 demonstrates the front-end electronics, in which capacitive and resistive type preamplifiers are briefly discussed. Section 3.2 introduces the closed loop drive mode controller design providing information about the extraction of the model parameters of the gyroscope. Section 3.3 presents an idea behind the open loop and closed loop rate sensing mechanisms. The closed loop sense mode controller design is also demonstrated in a detailed manner. Section 3.4 describes the closed quadrature cancellation controller electronics. Section 3.5 explains the closed loop mode-matching controller design for two proposed methods. Section 3.6 presents the noise performance analysis of the gyroscope for the mismatched and mode-matched conditions. Section 3.7 gives a summary of this chapter.

3.1 Front-End Electronics

At the front-end electronics of the system, the preamplifier and instrumentation amplifier is used to convert the current coming from the gyroscope to the voltage and to amplify this voltage to a desired signal level, respectively. In the preamplifier stage, the transimpedance amplifier (TIA) is preferred because it provides insensitivity to the total capacitance coming from the output capacitance of the sensor, wire-bonds, pads, and other parasitic capacitances. Since the inverting input of the TIA behaves as a virtual ground due toa high DC gain of the operational amplifier, and the TIA has low input impedance, the current is totally converted to the voltage through the preamplifier impedance without any significant signal loss. Figure 3.1 shows the schematic of the TIA studied in this work.

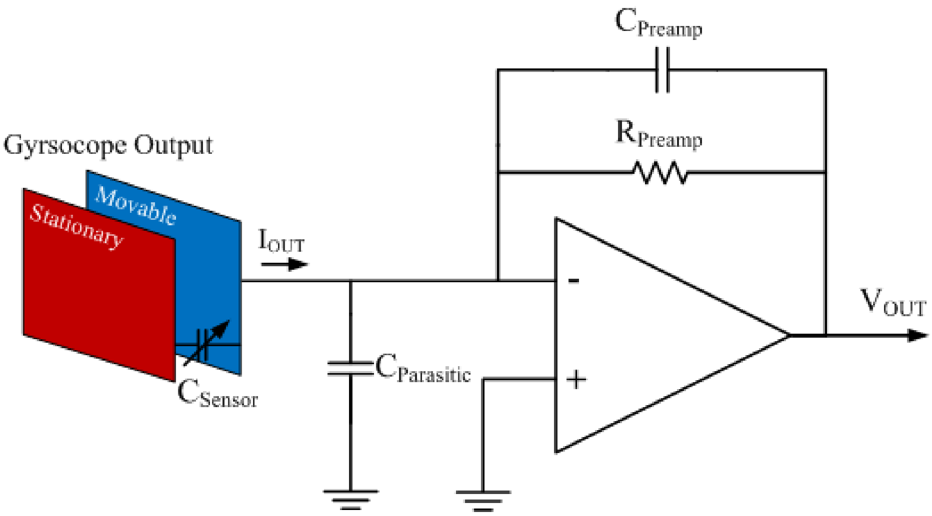

Figure 3.1: Schematic of the TIA studied in this work.

The transfer function of the TIA can be expressed as,

$$\left|\frac{V_{OUT}(s)}{I_{OUT}(s)}\right| = \frac{R_{Preamp}}{1 + sC_{Preamp}R_{preamp}} \qquad 3.1$$

If the multiplication of $sC_{Preamp}R_{preamp}$ is much smaller than 1, the preamplifier type becomes resistive, which is used at the drive mode controller. In the drive mode controller, the current obtained from the drive pick output of the gyroscope is directly converted to the voltage through R_{preamp} of the preamplifier. Although the R_{preamp} causes a thermal noise at the system, the phase of the drive pick signal used as a carrier signal in the system is basically considered by choosing the preamplifier type.

If the multiplication of $sC_{Preamp}R_{preamp}$ is adjusted to be much greater than 1, the preamplifier type becomes capacitive used in the sense mode controller. In the sense mode controller, the current coming from the sense pick output of the gyroscope is converted to the voltage through the impedance of $1/sC_{Preamp}$. The advantage of the capacitive preamplifier is low noise because the noise contribution of the preamplifier resistance is quite small compared to the resistive preamplifier. Therefore, it is preferred in the sense mode controller design.

3.2 Design of Drive Mode Controller for MEMS Vibratory Gyroscopes

The nature of the gyroscope operation states that the quadrature and Coriolis forces are directly proportional with the drive displacement and derivative of it, respectively. Therefore, the drive displacement must be kept stable and constant over time in order to achieve short and long term stability at the gyroscope operation. When the drive displacement shows a variation during the gyroscope operation, the scale factor stability and performance parameters of the system, ARW and bias instability, are directly affected from this variation, which generally results from environmental condition variations, such as temperature and vacuum level.

The main idea behind the operation of the drive mode controller is an amplitude controlled positive feedback mechanism. The drive mode of the gyroscope locks its resonance frequency by entering self-oscillation with the aid of the positive feedback mechanism because it is a very high-Q system. The drive mode quality factor of the gyroscope reaches a few tens of thousands under the vacuum condition. When the gyroscope enters the self-oscillation, the amplitude of the drive displacement is fixed to a certain level by controlling the amplitude of the drive mode oscillation. Thus, a change at the amplitude of the drive displacement due to environmental condition variations is significantly suppressed with the amplitude control mechanism.

The drive mode controller is mainly responsible for producing a sinusoidal signal, named as drive pick signal, by actuating the drive mode of the gyroscope with the amplitude controlled square wave signal. Figure 3.2 shows the simplified block diagram of the closed loop drive mode controller. First, the drive signal is directly picked from the drive pick output of the gyroscope through the preamplifier. The carrier signal and input of the demodulator are adjusted to be the same signal by using the resistive preamplifier to prevent the phase error coming from the demodulation and modulation. So the obtained drive signal is demodulated with itself and then the output of the demodulator is filtered by using a second order low pass filter to detect the amplitude information of the drive displacement. The resultant DC potential at the output of the low pass filter is compared with the reference DC potential, which sets to the desired drive displacement level. Since the reference potential is a band gap reference, which is considerably insensitive to environmental condition variations, the drive displacement is kept constant over time. Then, the error signal coming from the instrumentation amplifier is fed to the PI controller to generate the DC potential which determines the amplitude of the drive motor signal. Since the used modulator/demodulator is a switching type, the obtained drive motor signal is a square wave. The square wave signal consists of harmonics of the drive mode resonance frequency. However, at vacuum the drive mode of the gyroscope behaves like a sharp band pass filter because it is a very high-Q system, and its center frequency is located at the drive mode resonance frequency which is the first harmonic of the square wave signal. Therefore, all other harmonics except the first harmonic are rejected by the drive mode of the gyroscope. As a result, the drive of the gyroscope is locked to its resonance frequency.

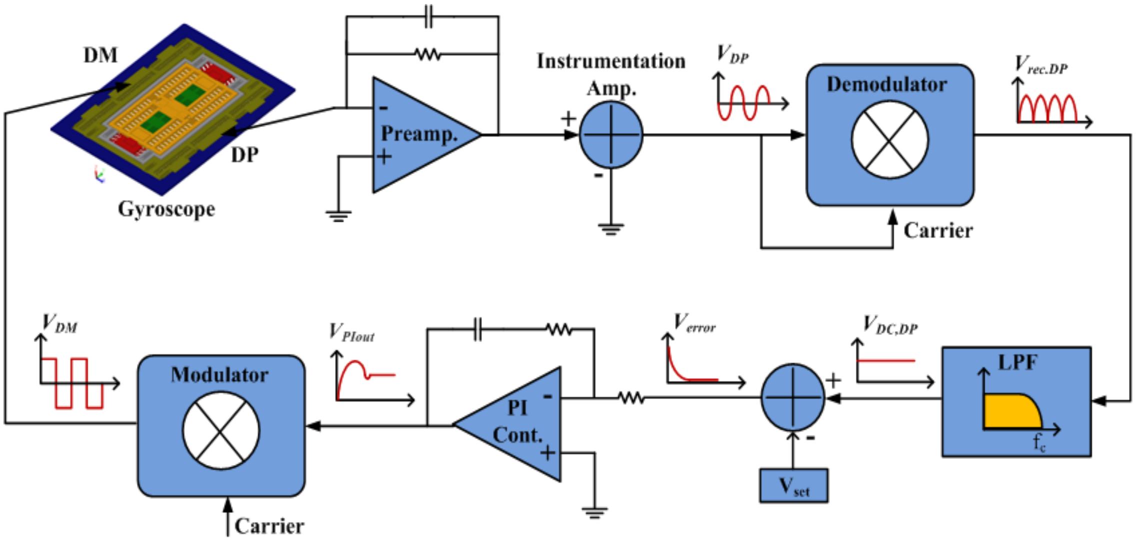

Figure 3.2: Simplified block diagram of the closed loop drive mode controller.

In the closed loop design of the drive mode, stability is the main concern. In that respect, there are four parameters, which are phase margin, settling time, overshoot, and steady state error, which should be considered by designing the controller and adjusting its parameters. To obtain a stable system, the phase margin should be adjusted to be greater than 60° [40]. Another consideration is the settling time that determines the speed of the system, and it is directly related with the bandwidth of the system. For high end of tactical grade applications, the settling time should be minimized to decrease the response time of the system. It should be kept as small as possible. The overshoot is other important criterion by adjusting the maximum drive displacement. In this study, the studied gyroscope has the maximum drive displacement of 8 μm, but it is the drive displacement limit of the gyroscope. Since the sensor can be damaged around the maximum drive displacement, the overshoot should be under control by adjusting the system parameters. The steady state error prevents to obtain the desired amount of the drive displacement. The steady state error becomes zero when the DC gain of the system reaches to infinite. Therefore, the integral based controller should be used to eliminate the steady state error in this work.

To analytically analyze the closed loop behavior of the drive mode controller, the open loop transfer function parameters of the gyroscope should be firstly extracted from the resonance tests and design specifications. Resonance tests give explicit information about the frequency response of the gyroscope. Figure 3.3 shows the simplified view of the drive mode resonance test schematic.

At the essence of the gyroscope operation, the gyroscope can be realized as three blocks, which are voltage to force conversion, force to displacement conversion, and displacement to current conversion blocks, as shown in Figure 3.3. The drive motor (DM) of the gyroscope is excited by a sinusoidal input whose frequency sweeps around the drive mode resonance frequency. The applied sinusoidal input voltage is converted to an actuation force through the DM capacitances. The actuation force results in a drive displacement, and then the drive displacement is converted to the current with the aid of the capacitive sensing mechanism. The current coming from the drive pick output of the gyroscope is transferred to the system as a drive pick signal after converting it to the potential through the preamplifier and instrumentation amplifier. The output and input ratio in the frequency domain give the frequency response of the drive mode of the gyroscope. The quality factor, resonance frequency, and gain are directly extracted from the frequency response characteristics of the gyroscope.

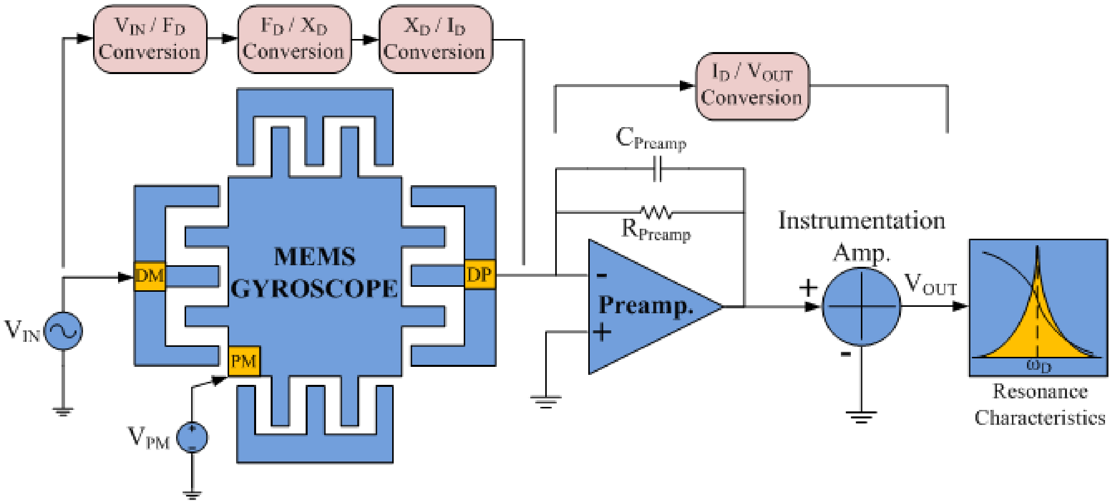

Figure 3.3: Simplified view of the drive mode resonance test schematic.

The dynamics of the gyroscope is partitioned to the conversion blocks for the simplification by deriving the transfer function of it. Considering these conversions, the drive mode open loop transfer function of the gyroscope can easily be expressed as

$$\frac{V_{OUT}(s)}{V_{IN}(s)} = \frac{F_D(s)}{V_{IN}(s)} \frac{X_D(s)}{F_D(s)} \frac{I_D(s)}{X_D(s)} \frac{V_{OUT}(s)}{I_D(s)} \qquad 3.2$$

By combining Equation 2.3, 2.25, 2.27, 2.32, and 3.1, the drive mode open loop transfer function of the gyroscope can be represented in terms of the sensor parameters as

$$\frac{V_{OUT}(s)}{V_{IN}(s)} = V_{PM}\frac{\partial C_{DM}}{\partial x}\frac{1/m_D}{\left(s^2 + \frac{\omega_D}{Q_D}s + \omega_D^2\right)}V_{PM}\frac{\partial C_{DP}}{\partial x}sZ_{preamp.}A_{inst.amp.} \qquad 3.3$$

The multiplication of the drive motor ($\partial C_{DM}/\partial x$) and drive pick ($\partial C_{DP}/\partial x$) sensitivity is determined under the drive mode resonance condition by equating the resonance gain to the right side of the Equation 3.3. From this multiplication value, the sensitivity of them is individually found from the ratio between $\partial C_{DM}/\partial x$ and $\partial C_{DP}/\partial x$ extracted from the design parameters. The drive mass (m_D) of the gyroscope are analytically calculated from the design. The proof mass potential (V_{PM}) is adjusted around 10 V in this work by regarding the operation modes of the gyroscope, mode-matched and mismatched mode. The other parameters, which are the quality factor, resonance frequency, and gain, are known parameters as a result of resonance test.

The drive displacement is directly proportional with the drive pick signal, shown in Equation 3.4. After setting the drive pick signal, the amplitude of the drive pick signal is adjusted by changing the gain of the low pass filter or the gain of the modulator, used in the closed loop drive mode controller. In this work, the drive displacement is adjusted around 4 µm, which is in the safe region. For higher drive displacement values the performance of the gyroscope improves but it cannot be safe during the gyroscope operation when the overshoot is taken into account.

$$V_{DP}(j\omega) = V_{PM}\frac{\partial C_{DP}}{\partial x}j\omega X_D Z_{preamp.}A_{inst.amp.} \qquad 3.4$$

Adjusting the drive displacement, another critical factor is the resonance frequency variation of the gyroscope with changing temperature. At resonance the drive pick signal is directly proportional with the drive mode resonance frequency of the gyroscope clearly shown in Equation 3.4. Since the drive pick signal is always constant at the system, the drive displacement changes in response to the resonance frequency shift.

However, the variation at the amount of the drive displacement is kept infinitesimally small because the resonance frequency of the studied gyroscope is around 13 kHz, and it changes only a few Hz in the temperature range from -40 ºC to +80 ºC. The details will be given in Chapter 5.

Before analyzing the closed loop behavior of the controller, the open loop response of the controller should be analyzed to adjust the phase margin, settling time, and overshoot. The gyroscope model is a second order, but the analysis of it gets very complicated during the controller design. At resonance the second order gyroscope model can be simplified to a first order system which is the envelope model of the modulated system. The first order model of the gyroscope between the modulator and demodulator can be equated to

$$H_D(s) = \frac{A_D}{1 + s/\beta_D} \qquad 3.5$$

where $A_D$is the resonance gain of the drive mode with the front-end electronics, and β_D is the low frequency pole, and is represented as

$$\beta_D = \frac{\omega_D}{2Q_D} \qquad 3.6$$

The low frequency pole coming from the gyroscope model deteriorates the bandwidth and phase margin of the system. Therefore, this pole is eliminated by cancelling it with the zero of the PI controller. The detailed analysis of pole-zero cancellation can be found in [40].

The “Butterworth” type second order low pass filter with a multiple feedback topology is used in all controllers designed in this study. The cut-off frequency of it is chosen as 100 Hz, which satisfies the specifications of the most of the gyro applications. After determining the controller parameters, the open loop transfer function of the controller can be expressed as

$$H_{OL}(s) = \frac{A_D}{1 + s/\beta_D} K_{Demod.} H_{LPF}(s) \frac{K_I(1 + s\,K_P/K_I)}{s} K_{Mod.} \qquad 3.7$$

where $K_{Demod.}$ and $K_{Mod.}$ is the gain of the demodulator ad modulator, respectively. Also, K_P and K_I is the proportional and integral gain of the PI controller. Since the low frequency pole coming from the first order envelope model of the gyroscope is cancelled with the zero of the PI controller, the open loop characteristic of the drive mode controller can be considered as a third order system, in which two poles comes from the low pass filter, and the other comes from the integral control part of the PI controller.

To obviously understand the behavior of the system, the open loop characteristic was examined by using the real sensor parameters. Table 3.1 shows model parameters of the gyroscope (C05) obtained through the resonance test for the drive mode.

Table 3.1: Model parameters of the drive mode of the gyroscope (C05) used during the design of the closed loop drive mode controller for 10 V_{PM}.

Model Parameter (Drive Mode)	**Value**
Resonance Frequency (f_D)	11805Hz
Quality Factor (Q_D)	22702
Resonance Gain (A_D)	0.8dB (1.1)

The open loop transfer function is evaluated to adjust the phase margin, settling time, and overshoot by using the real controller and sensor parameters. The open loop transfer function with the real controller and sensor parameters can be expressed as

$$H_{OL}(s) = \frac{1.1}{1 + s/1.63} * \frac{2}{\pi} * \frac{8 * 394784}{s^2 + 881.1s + 394784} * \frac{K_I(1 + s\,K_P/K_I)}{s} * \frac{4}{\pi} \qquad 3.8$$

From the Equation 3.8, it is clearly observed that the modulator and low pass filter gain are adjusted as 1 and 8, respectively, to set the peak to peak potential level of the drive pick signal at 800 mV corresponding to the drive displacement of 4 μm for the studied gyroscope C05. The gain of $2/\pi$ and $4/\pi$ comes from by finding the RMS value of the rectified drive pick signal and the first harmonic of the square wave drive motor signal. To obtain the sufficient phase margin for stability, minimum settling time, and minimum overshoot, after a few iterations in "MATLAB" program, K_P is found as 45.4, and K_I is found as 74.1 by performing the pole-zero cancellation. Figure 3.4 shows the bode diagram of the drive mode open loop transfer function.

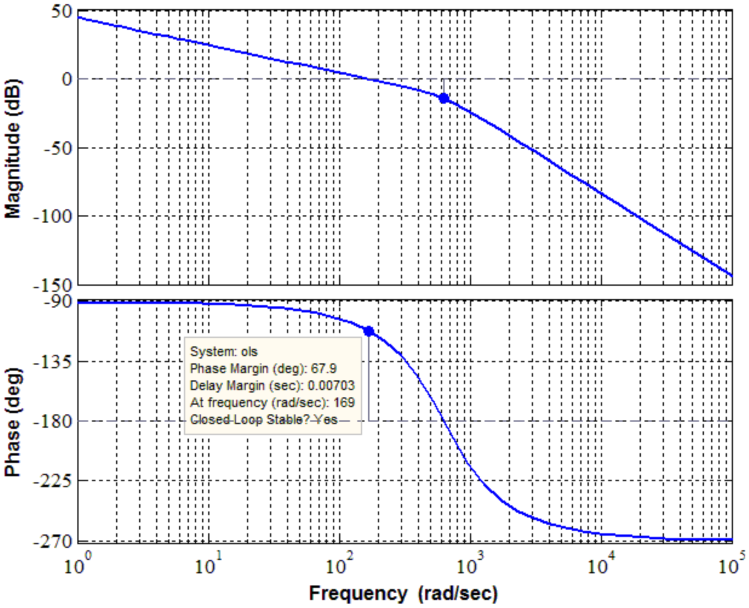

Figure 3.4: Bode diagram of the drive mode open loop transfer function. These plots were generated in the "MATLAB" environment by using the real controller and sensor parameters.

As can be shown in Figure 3.4, the phase margin of the system is higher than 60°, which guarantees that the system stability is sustained. Correspondingly, the closed step response of the open loop transfer function is analyzed to determine the settling time and overshoot at the system. Figure 3.5 shows the closed loop step response of the drive mode controller.

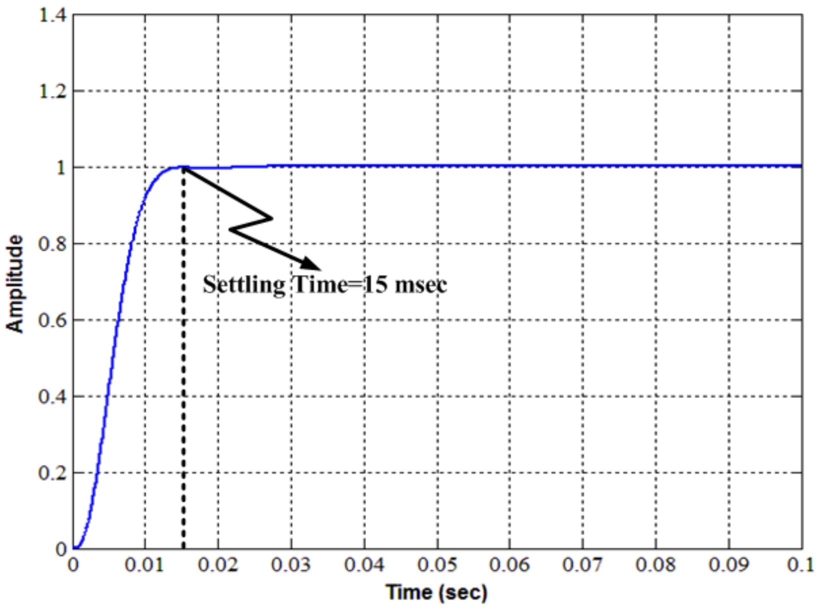

Figure 3.5: Closed loop step response of the drive mode controller.

The system settles in a 15 msec without any overshoot. The overshoot at the system is eliminated by considering the open loop gain of the system.

To analyze the transient closed loop behavior of the system, it is examined in the “MATLAB SIMULINK” program by using the open loop controller parameters. Figure 3.6 shows the SIMULINK model of the closed loop drive mode controller. In the SIMULINK model, the exact second order model of the gyroscope, shown in Equation 3.3, is used instead of the first order envelope model of it to achieve a consistency between the simulation and experiment. The other parts of the SIMULINK model are constructed by using the real parameters of the circuitry.

Figure 3.7 shows the drive pick signal obtained from the realistic SIMULINK model. The consistency between the closed and open loop analysis is obviously verified by controlling the settling time of the system, which is equal to 15 msec within the error band of ±1%. The peak to peak value of the drive pick signal is adjusted as 800 mV for the drive displacement of 4 μm mentioned above.

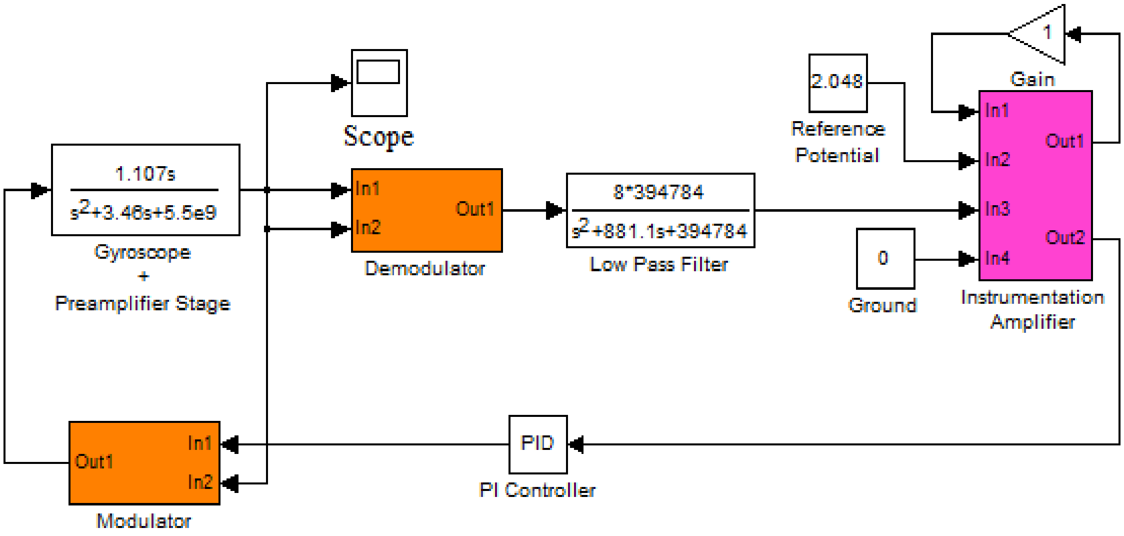

Figure 3.6: SIMULINK model of the closed loop drive mode controller constructed using the exact model of the gyroscope (C05) and real parameters of the circuitry.

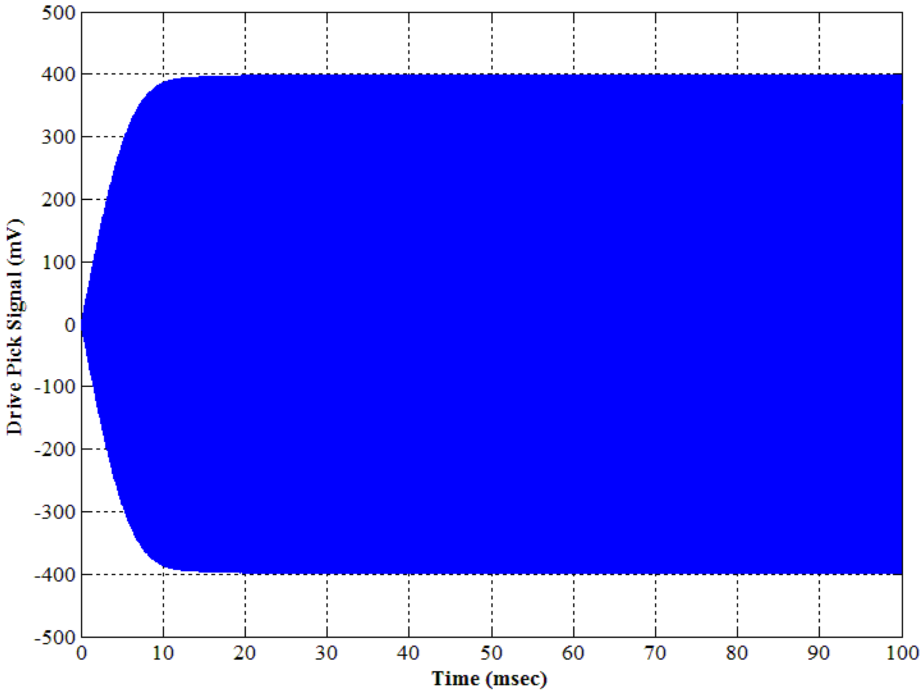

Figure 3.7: Drive pick signal obtained from a realistic SIMULINK model.

3.3 Sense Mode Controller

Rate sensing at the sense mode of the gyroscope can be performed using open loop or closed loop controller mechanisms. Details of the open loop and closed loop controller mechanisms for the mode-matched gyroscope operation are discussed considering the related problems in the following subsections.

3.3.1 Open Loop Rate Sensing Mechanism

Open loop rate sensing is an approach that enables to obtain the angular rate information through the phase sensitive demodulation. Ideally, there is a signal, called sense pick signal, exists at the sense mode output of the gyroscope, and it is directly proportional with the amount of the angular rotation rate, but in practice the sense pick signal is sum of two signals, Coriolis and quadrature error signals. There is always 90° phase difference exists between the Coriolis and quadrature signals. Therefore, the phase sensitive demodulation is required to get rate information from the sense mode output of the gyroscope. Figure 3.8 shows the schematic of the open loop rate sensing mechanism.

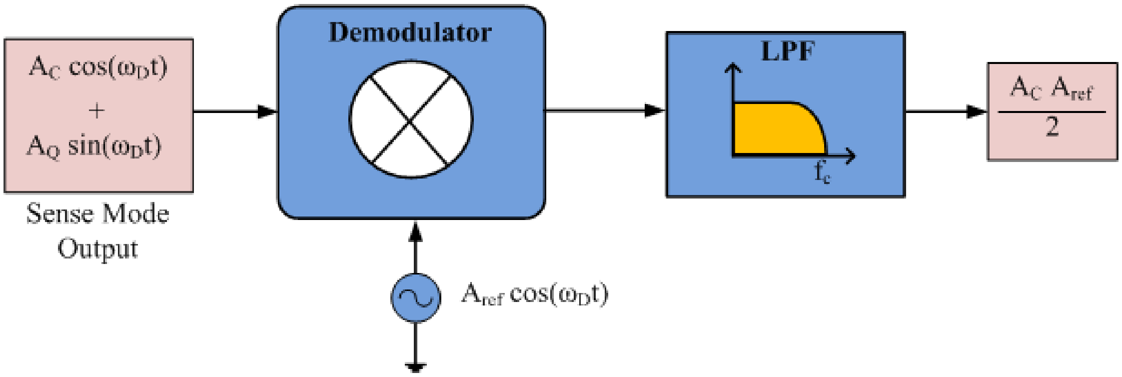

Figure 3.8: Schematic of the open loop rate sensing mechanism.

In Figure 3.8, A_C and A_Q at the sense mode output of the gyroscope represent the amplitude of the Coriolis and quadrature error signals, respectively. Also, A_{ref} stands for the constant amplitude of the carrier signal used for demodulation. Under the assumption that there is no phase error during the demodulation, the output of the low-pass filter can be equated to

$$A_{out} = \left[A_C \cos(\omega_D t) + A_Q \sin(\omega_D t)\right] \times A_{ref} \cos(\omega_D t)$$

$$\xrightarrow{Demodulation} \frac{A_C A_{ref}}{2}[\cos(2\omega_D t) + \cos(0)] + \frac{A_Q A_{ref}}{2}[\sin(2\omega_D t) + \sin(0)] \qquad 3.9$$

$$\xrightarrow{LPF} \frac{A_C A_{ref}}{2}$$

Equation 3.9 states that there is only a Coriolis signal obtained rejecting the quadrature error term through the simple phase sensitive demodulation, providing no phase error during the demodulation.

In the open loop rate sensing mechanism, the mode-matched gyroscope operation brings some problems related with the sense mode quality factor that directly affects the scale factor and system bandwidth. It is noticed from Equation 3.9 that the output of the low pass filter can be defined as the scale factor for an angular rotation rate of 1 °/s. Referring to Equation 2.32 and 2.17, the Coriolis term, A_C, inside the scale factor is directly proportional with the sense mode quality factor under the mode-matched gyroscope operation. Therefore, when there is a change exists in the sense mode quality factor due to ambient variations, such as temperature and vacuum, a deviation occurs in the scale factor, which cannot be prevented in the open loop rate sensing mechanism. The deviation in the scale factor deteriorates the long-term stability of the gyroscope operation. Therefore, the open loop rate sensing is not a reliable method for the long-term gyroscope operation.

In the open loop operation of the gyroscope, the system bandwidth is limited with the mechanical bandwidth of the sensor, which can be expressed as

$$f_{BW} = \frac{f_S}{2Q_S} \qquad 3.10$$

where f_S and Q_S are the sense mode resonance frequency and quality factor, respectively. In high-Q systems, the mechanical bandwidth is only in the order of a few Hz. Therefore, it cannot be precisely controlled during the mode-matched gyroscope operation in the presence of ambient variations that leads to a substantial change in the sense mode quality factor. Also, the system bandwidth mechanically defined by the sensor, which limits the application areas of the gyroscope, such as consumer and automotive applications, which commonly require a system bandwidth of 50 Hz.

Closed loop feedback mechanism is commonly used in the controller electronics of the gyroscopes to overcome the problems associated with the open loop rate sensing mechanism. It also provides an improvement in a dynamic range and linearity, as well as an improvement in the system bandwidth and scale factor stability [44]. Especially, the mode-matching implementation in high-Q gyroscopes requires feedback mechanisms to ensure proper operation. Therefore, in this study, the closed loop rate sensing mechanism is constructed using force-feedback electrodes.

3.3.2 Closed loop Rate Sensing Mechanism

The main motivation behind the closed loop rate sensing mechanism is to extract the rate information without sacrificing the scale factor stability and bandwidth during the mode-matched gyroscope operation. Dynamic range and linearity are also concerned during the design of the closed loop feedback mechanism. Figure 3.9 shows the block diagram of the proposed closed loop sense mode controller. The sense mode signals caused by a Coriolis force are differentially picked from the sensor through the capacitive preamplifiers, and then the phase sensitive demodulation with the low-pass filter is performed, similar with the open loop rate sensing mechanism, to obtain the DC rate information. Next, the DC rate, called error signal, is fed to the PI controller that generates a DC potential required to stop the sense mode displacement with the aid of the force-feedback electrodes. The generated DC potential is a measure of the applied angular rotation rate, but in this study the actual rate information is obtained after multiplying the generated DC potential with a gain provided by an amplifier.

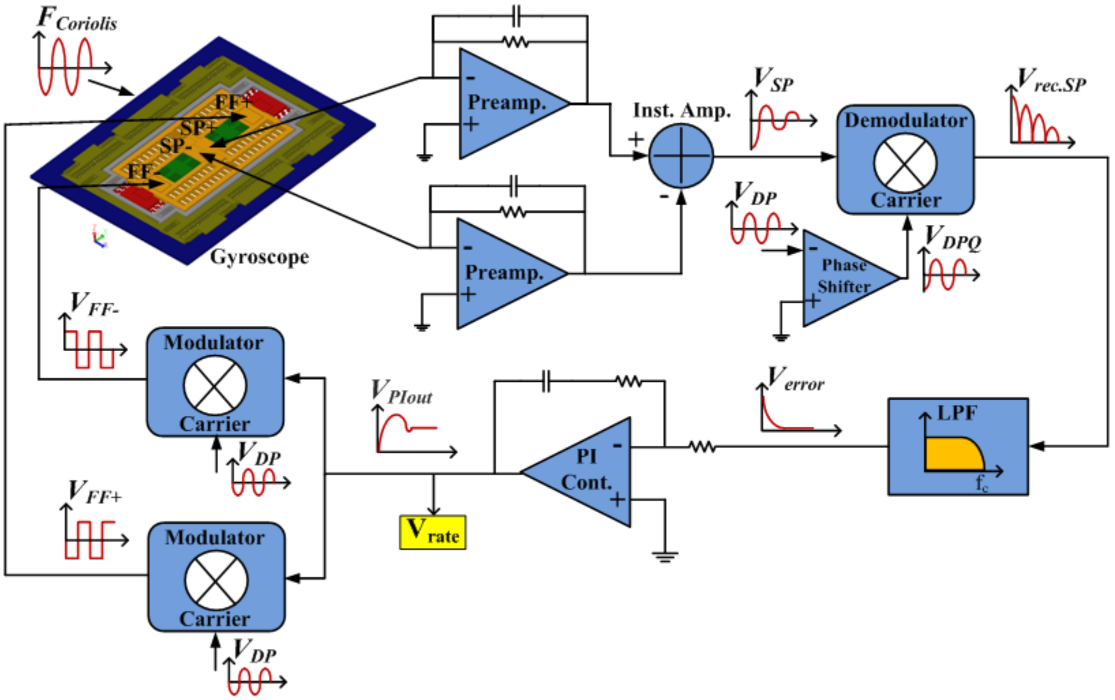

Figure 3.9: Block diagram of the proposed closed loop sense mode controller.

Force-feedback electrodes are widely used in the closed loop gyroscope operations to prevent the sense mode displacement of the gyroscope [44, 45]. When the sense mode of the gyroscope is subject to a high Coriolis force, the resultant displacement causes a nonlinearity at the sense mode output of the gyroscope due to the nonlinear behavior of varying-gap type sensing electrodes. It should be noted that the sense mode displacement maximizes due to the sensitivity improvement when the mode frequencies of the gyroscope is matched. Therefore, the sense mode displacement should be stopped during the mode-matched gyroscope operation to achieve an improvement in linearity and dynamic range. The proposed closed loop force-feedback mechanism shown in Figure 3.9 eliminates the sense mode displacement by generating an electrostatic force with the same amplitude of the Coriolis force through the force-feedback electrodes. The condition required to eliminate the sense mode displacement is derived in [41] as

$$V_{PM}\frac{\partial C_{FF}}{\partial y}V_{FF}=2m_{PM}\Omega_z j\omega_D X_D \qquad \text{3.11-a}$$

$$V_{FF}=\frac{2m_{PM}\Omega_z j\omega_D X_D}{V_{PM}\frac{\partial C_{FF}}{\partial y}} \qquad \text{3.11-b}$$

In Equation 3.11, $\partial C_{FF}/\partial y$ denotes the sensitivity of the force-feedback electrodes, and V_{FF} represents the amplitude of the AC signal applied to the force-feedback electrodes. The applied rate is directly proportional with the amplitude of V_{FF}, which is not affected from the ambient variations because the terms inside Equation 3.11 are not directly dependent on the quality factor of the gyroscope's modes. Therefore, the scale factor at the closed loop force-feedback controller is observed to be more stable compared to the open loop sense mode controller.

Bandwidth is another important criterion designing the sense mode controller. In the open loop operation, the system bandwidth is defined by the mechanical sensor. However, the use of the proposed closed loop feedback mechanism provides an opportunity to control the system bandwidth as an independent of the mechanical sensor with the aid of the PI controllers, which eliminates the mechanical bandwidth limitation compared to the open loop sense mode controller. Through the pole-zero cancellation method described in Section 3.2, the closed loop feedback mechanism guarantees an improvement in the transient response time of the system, which results in a bandwidth extension at the system. The pole-zero cancellation is accomplished by adjusting the PI controller parameters of the sense mode controller. Figure 3.10 shows the closed loop sense mode dynamics with a typical value of 4 Hz mechanical sensor bandwidth, and its rate equivalent sense mode dynamics with greater than a system bandwidth of 50 Hz.

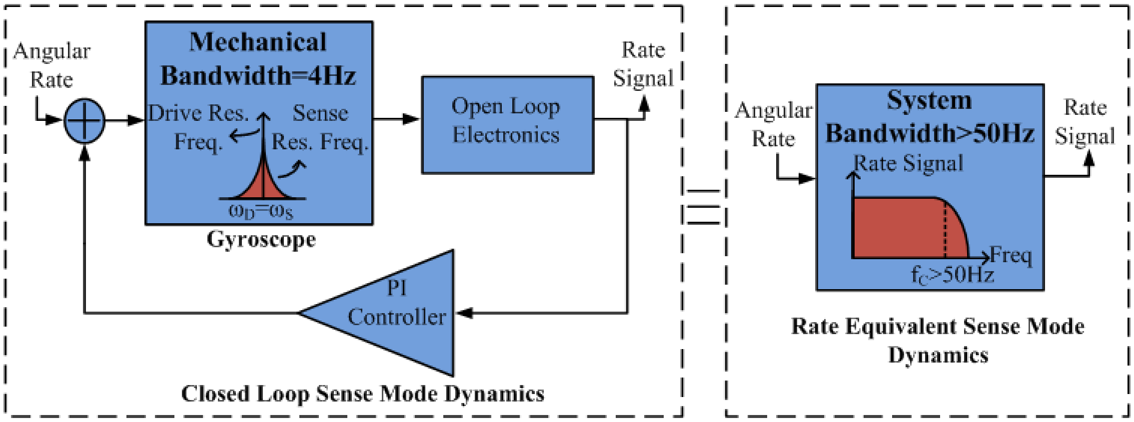

Figure 3.10: Closed loop sense mode dynamics with a typical value of 4 Hz mechanical sensor bandwidth (on the left), and its rate equivalent sense mode dynamics with greater than a system bandwidth of 50 Hz (on the right).

To analyze the closed loop behavior of the sense mode controller, the sense mode dynamics of the gyroscope should be extracted considering the related conversions, illustrated in Figure 3.3. Considering the electromechanical conversion blocks in the sense mode, similar with the drive mode, the transfer function of the gyroscope for the sense mode can be expressed with the same relation shown in Equation 3.2 by changing the subscript “$_{\mathrm{D}}$” (denotes drive mode) with “$_{\mathrm{S}}$” (denotes sense mode). Inserting the corresponding terms inside in Equation 3.2, the sense mode transfer function can be equated to

$$\frac{V_{SP}(s)}{V_{FF}(s)} = V_{PM}\frac{\partial C_{FF}}{\partial y}\frac{1/m_S}{\left(s^2+\frac{\omega_S}{Q_S}s+\omega_S{}^2\right)}V_{PM}\frac{\partial C_{SP}}{\partial y}sZ_{preamp.}A_{inst.amp.} \qquad 3.12$$

Under the sense mode resonance condition, Equation 3.12 is simplified to

$$A_S = \left.\frac{V_{SP}}{V_{FF}}\right|_{\omega=\omega_S} = \frac{1}{m_S}V_{PM}{}^2\frac{\partial C_{FF}}{\partial y}\frac{Q_S}{\omega_S}\frac{\partial C_{SP}}{\partial y}Z_{preamp.}A_{inst.amp.} \qquad 3.13$$

In Equation 3.13, the parameters of $\partial C_{FF}/\partial y$, sensitivity of the force-feedback electrodes, and $\partial C_{SP}/\partial y$, sensitivity of the sense pick electrodes, are directly extracted through the resonance gain, A_S , which has been performed similar with the drive mode. The only difference between the drive and sense modes of the gyroscope are the input and the output configuration, which are designed to be differential in the sense mode, differently from the drive mode, which provides an opportunity to suppress the effect of capacitive coupling on the sense mode and increase noise immunity.

The sense mode of the gyroscope is operated at resonance under the mode-matched condition. Therefore, the sense mode transfer function of the gyroscope shown in Equation 3.12 is simplified to a first order envelope model between the demodulator and modulator, similarly in the drive mode. The first order envelope model of the sense mode can be expressed as

$$H_S(s) = \frac{A_S}{1 + s/\beta_S} \qquad 3.14$$

where A_S is the resonance gain of the sense mode, and β_S, the low-frequency pole, can be found by

$$\beta_S = \frac{\omega_S}{2Q_S} \qquad 3.15$$

The low frequency pole, β_S, coming from the first order envelope model of the sense mode slows down the transient settling of the closed loop sense mode controller which directly leads to a reduction in the system bandwidth. Therefore, this pole is eliminated through the zero provided to the system adjusting the parameters of the PI controller, which is called pole-zero cancellation. Hence, the system bandwidth is significantly extended, independent of the mechanical sensor bandwidth, due to an increase in the gain-bandwidth product (GBW) of the proposed closed loop sense mode controller. After the pole-zero cancellation, GBW can also be adjusted changing the closed loop gain of the sense mode controller, which is directly achieved by changing the integral gain of the PI controller. The control of GBW product provides “adjustable system bandwidth” in the mode-matching system.

A similar algorithm is followed as in the drive mode designing the closed loop sense mode controller. The open loop analysis of closed loop sense mode controller is first performed during the design of the controller using the real controller and sensor parameters to achieve a consistency between the simulation and experiment. The phase margin, settling time, and overshoot are optimized through the open loop analysis to ensure stable gyroscope operation under the mode-matched condition. The model parameters of the gyroscope (C05), used during the design of the closed loop sense mode controller, are given in Table 3.2.

Table 3.2: Model parameters of the gyroscope (C05) used during the design of the closed loop sense mode controller.

Model Parameter (Sense Mode)	Value
Resonance Frequency (f_S), Hz	11805
Quality Factor (Q_S)	1350
Resonance Gain (A_S)	25dB (17.8)

The open loop transfer function of the sense mode controller for the gyroscope (C05) can be expressed as

$$H_{OL}(s) = \underbrace{\frac{17.8}{1 + s/27.56}}_{H_S(s)} * \underbrace{\frac{4}{\pi}}_{K_{Demod.}} * \underbrace{\frac{6.56 * 394784}{s^2 + 881.1s + 394784}}_{H_{LPF}(s)} * \underbrace{\frac{K_I(1 + s\,K_P/K_I)}{s}}_{H_{PI}(s)} * \underbrace{\frac{4}{\pi}}_{K_{Mod.}} \qquad 3.16$$

In Equation 3.16, $4/\pi$ represented by $K_{Demod.}$ is the RMS value of the rectified sense pick signal with a demodulator gain of 2, $4/\pi$ denoted by $K_{Mod.}$ is the first harmonic of the force-feedback signal with a unity modulator gain. The low pass filter is used with the gain of 6.56 and cut-off frequency of 100 Hz in the proposed closed loop sense mode controller. The parameters of the PI controller are adjusted to eliminate the zero coming from the first order envelope model of the gyroscope, $H_S(s)$, by equating the term of K_I/K_P to 27.56, β_S. After finding the ratio of K_I/K_P, the phase margin, settling time, overshoot, and bandwidth are adjusted through the parameter of K_I.

It should be noted that the settling time of the closed loop system is directly related to the gain-bandwidth product (GBW) of the closed loop sense mode controller. When GBW increases, the settling time decreases, and corresponding to the decrease in the settling time, the bandwidth of the sense mode controller improves because the settling time is directly associated with the bandwidth. Therefore, after setting the ratio of K_I/K_P that provides the pole-zero cancellation, the bandwidth can be controlled changing the closed loop gain of the sense mode controller through the adjustment of the amplitude of the PI controller parameter, K_I. To conclude, the pole-zero cancellation and the adjustment of the closed loop gain of the sense mode controller allow controlling the system bandwidth, independently from the mechanical sensor bandwidth, in the mode-matching system.

In this work, after a few iterations in “MATLAB” program, K_I is adjusted to be 0.1, and K_p is adjusted to be 0.0036 to achieve sufficient phase margin, minimum settling time, and minimum overshoot, which are required for the stable gyroscope operation with a high system bandwidth.

Figure 3.11 shows the bode diagram of the open loop sense mode analysis. The phase margin is adjusted to be 67.9°, which is sufficiently high to ensure proper gyroscope operation.

Figure 3.12 shows the closed loop step response of the sense mode controller. The settling time of the system is adjusted to be 15 msec without any overshoot. The obtained settling time ensures higher than 50 Hz system bandwidth under the second order system approximation for the proposed closed loop sense mode controller.

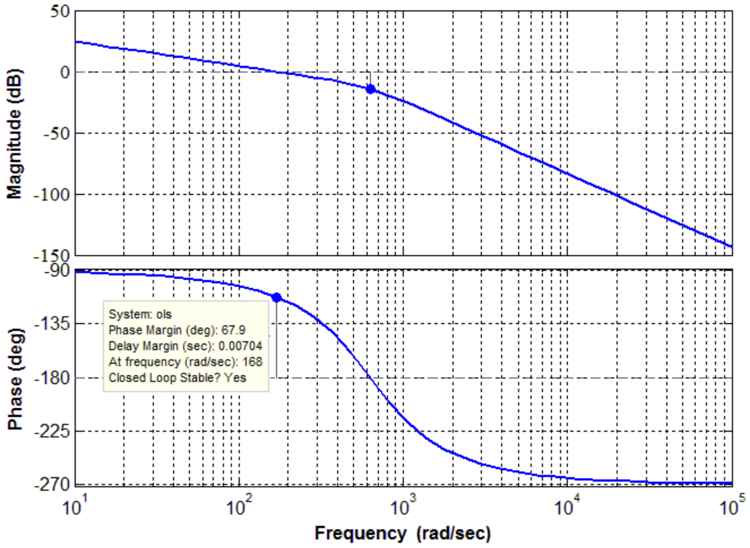

Figure 3.11: Bode diagram of the open loop sense mode analysis.

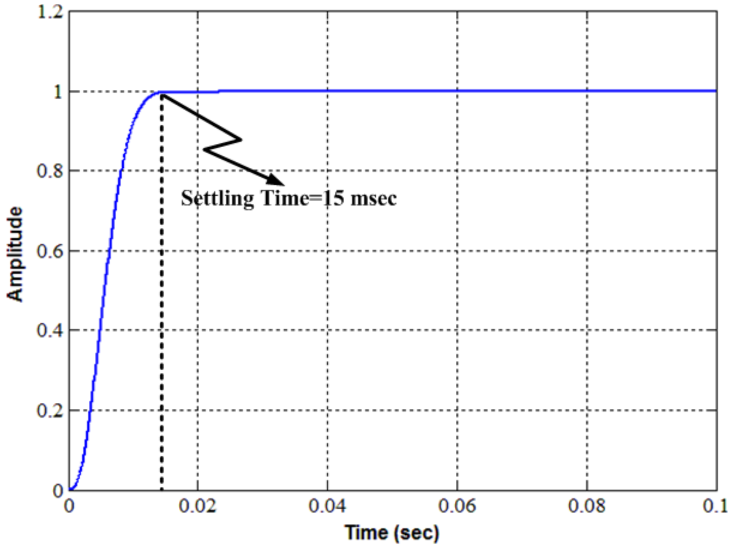

Figure 3.12: Closed loop step response of the sense mode controller.

To analyze the transient behavior of the system, the SIMULINK model for the closed loop sense mode controller, shown in Figure 3.13, is constructed using the real sensor and controller electronics parameters to establish a consistency between the simulation and experiment. In the SIMULINK model, a Corolis signal is applied to the system as an angular rotation rate.

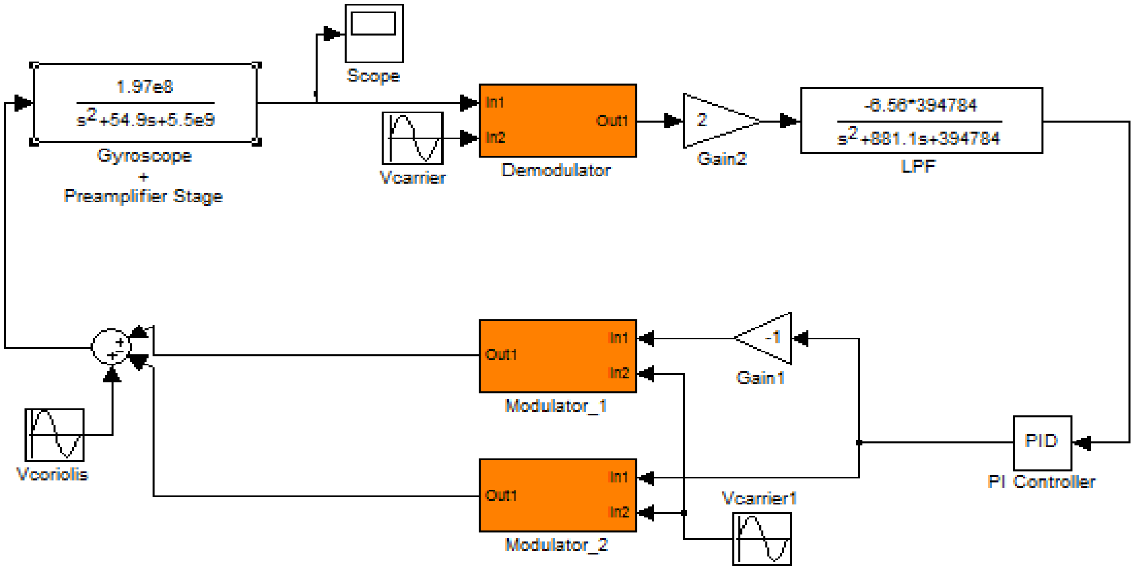

Figure 3.13: SIMULINK model for the closed loop sense mode controller.

Figure 3.14 shows the settling behavior of the closed sense mode controller. The settling time of the closed loop sense mode controller is 15 msec, which is consistent with the open loop sense mode analysis.

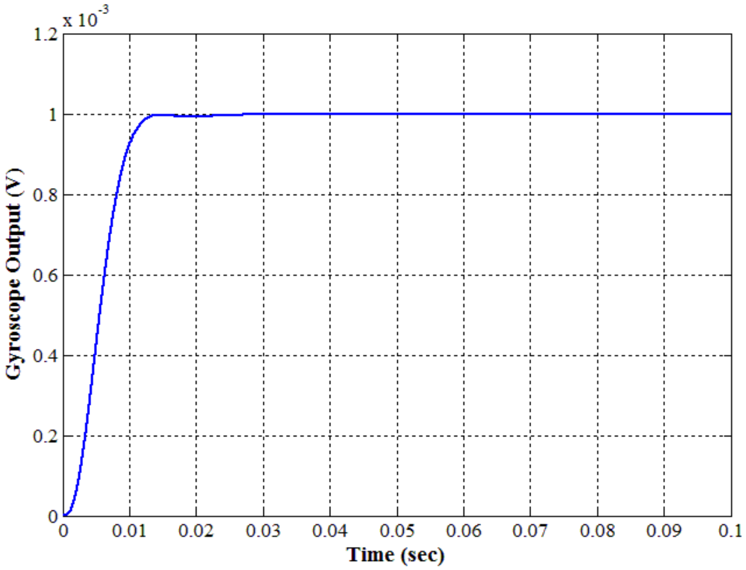

Figure 3.14: Settling behavior of the closed sense mode controller.

Figure 3.15 shows the transient behavior of the sense pick signal in response to the Coriolis signal. The sense pick signal directly provides information about the sense mode displacement, which maximizes when the system reaches to steady-state, and then its amplitude goes to zero with the aid of the force-feedback electrodes. The amount of the sense pick signal is not critical after the start-up because the rate information is carried by the PI controller output. In addition, the transient behavior of the sense pick signal indicates and shows that the sense mode displacement is stopped in a short time, which provides linearity at the gyroscope operation.

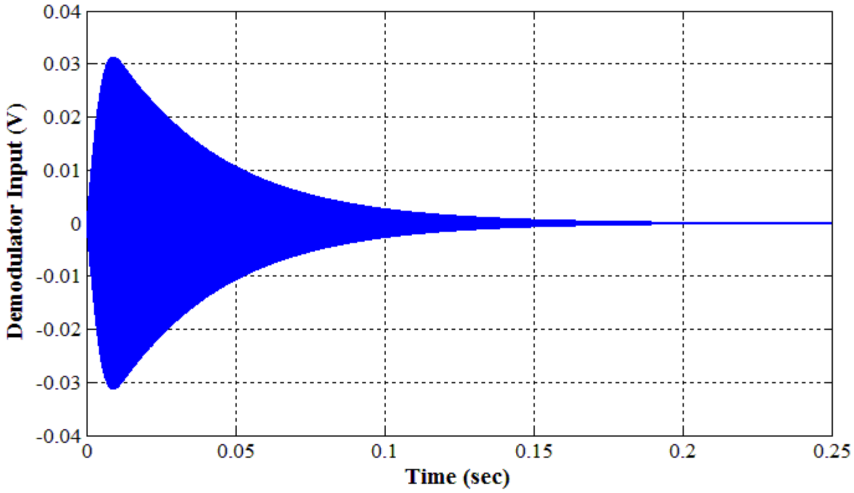

Figure 3.15: Transient behavior of the sense pick signal in response to a Coriolis signal.

A sinusoidal angular rate signal, whose frequency ramps from 0 Hz to 60 Hz in a time, is applied to the input of the gyroscope as a Coriolis signal to obtain the frequency response of the sense mode controller. Figure 3.16 shows the frequency response characteristics of the closed loop sense mode controller for different K_I and K_p parameters, which shows the simulated bandwidth of the mode-matching system. The 3-dB points correspond to the system bandwidth. The simulation results verify that the system bandwidth can be adjusted using the pole-zero cancellation and changing the closed loop gain of the sense mode controller simultaneously, independently from the mechanical sensor bandwidth, with the aid of the PI controller parameters.

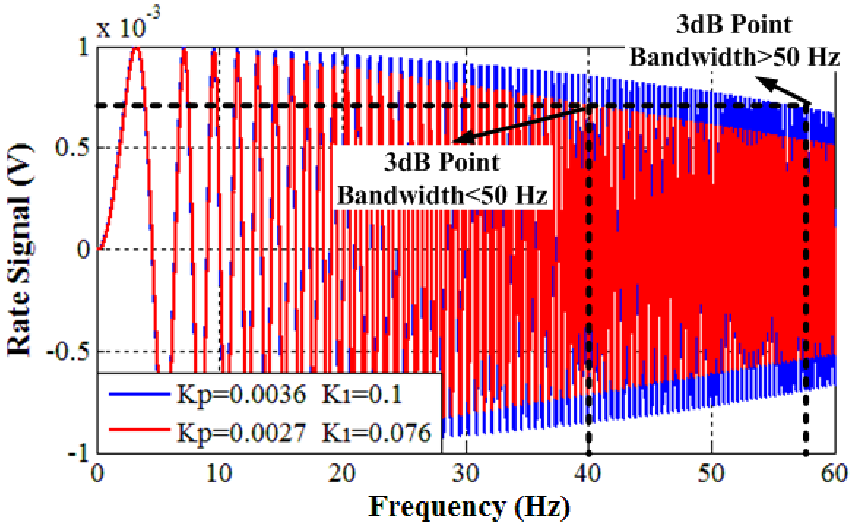

Figure 3.16: Frequency response characteristics of the closed loop sense mode controller that shows the simulated bandwidth of the mode-matching system for different K_I and K_p parameters.

3.4 Design of Quadrature Cancellation Controller

Quadrature cancellation mechanism is mainly based on the phase sensitive demodulation, similarly used in the sense mode. Figure 3.17 shows the schematic of the proposed closed loop quadrature cancellation controller. First, the quadrature signal directly picked from the sense mode output of the gyroscope through preamplifiers is demodulated with the drive pick signal to obtain the envelope of the quadrature signal, but, in the sense mode controller design, the sense pick signal is modulated with the 90° phase shifted version of the drive pick signal to extract rate information due to the phase difference between the quadrature and Coriolis signals, always equal to 90°. Next, the envelope of the quadrature signal is low-pass filtered to get the amplitude information of the quadrature error, and then the output of the low pass filter is compared to the pre-determined offset signal, which provides an opportunity to adjust the amount of the residual quadrature signal used to achieve the mode-matched gyroscope operation in this study. The resultant signal, called error signal, is fed to PI controller to generate a DC potential that is applied to the quadrature electrodes together with the inverted version of it in order to cancel the quadrature error by creating a rotational torque on the proof mass frame of the gyroscope.

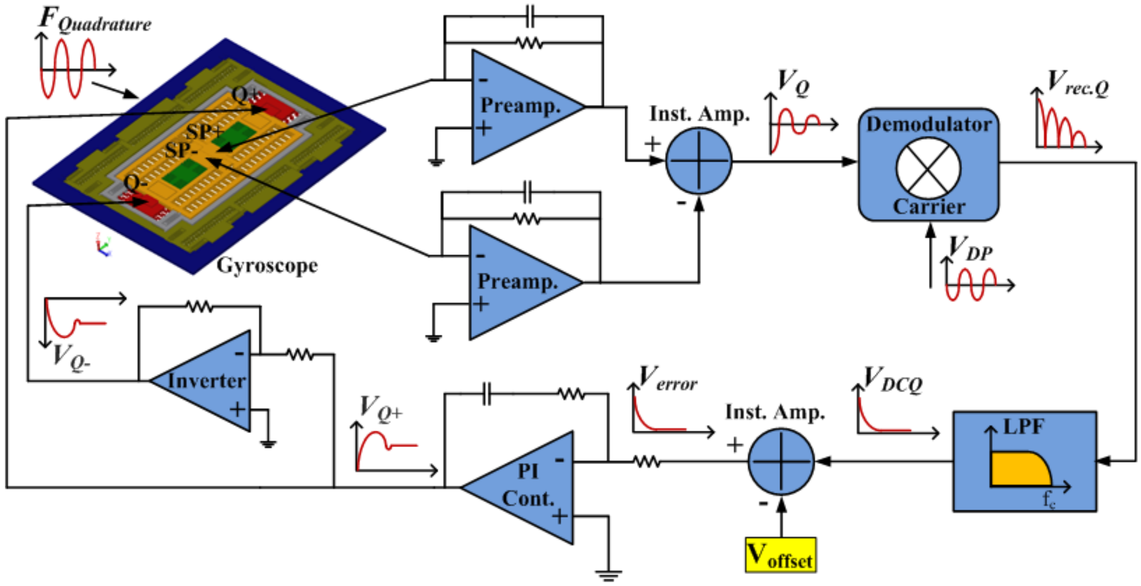

Figure 3.17: Schematic of the proposed closed loop quadrature cancellation controller.

The main motivation behind the quadrature cancellation controller relies on the electrostatic forces, differentially generated by constructing a potential difference on the quadrature electrodes. The generated electrostatic force on the quadrature electrodes is derived in [39] as

$$F_{Quad.} = n\frac{4V_{PM}\Delta V\varepsilon X H_0}{D_0^2} \qquad 3.17$$

where n denotes the total number of the quadrature electrode placed in the gyroscope, ΔV is the applied potential to the quadrature electrodes, H_0 is the height of the quadrature electrodes, and D_0 is the gap spacing across the capacitors in the quadrature electrodes. The generated quadrature force directly acts on the sense mode dynamics to eliminate the mechanical crosstalk between the individual resonance modes of the gyroscope. Therefore, considering the related conversion mechanisms in the sense mode of the gyroscope implied in Section 3.2, the gyroscope can be modeled as

$$\frac{V_{SP,Quad.}(s)}{F_{Quad.}(s)} = \frac{1/m_S}{\left(s^2 + \frac{\omega_S}{Q_S}s + \omega_S{}^2\right)} V_{PM} \frac{\partial C_{SP}}{\partial y} sZ_{preamp.}A_{inst.amp.} \qquad 3.18$$

Under resonance condition, Equation 3.18 is simplified to

$$A_Q = \left.\frac{V_{SP,Quad.}}{F_{Quad.}}\right|_{\omega=\omega_S} = \frac{1}{m_S}\frac{Q_S}{\omega_S} V_{PM} \frac{\partial C_{SP}}{\partial y} Z_{preamp.}A_{inst.amp.} \qquad 3.19$$

where the parameter of $\partial C_{SP}/\partial y$, sensitivity of the sense pick electrodes, and other parameters are directly obtained from the sense mode resonance test of the gyroscope. Under the mode-matched condition, the second order sense mode dynamics of the gyroscope shown in Equation 3.18 is simplified to a first order envelope model represented as

$$H_{S,Q}(s) = \frac{A_Q}{1 + s/\beta_S} \qquad 3.20$$

In Equation 3.20, β_S is the low frequency pole and is calculated in Equation 3.15. This low frequency pole degrades the settling time of the closed loop quadrature cancellation electronics. To increase the settling time, the pole-zero cancellation method, similarly used in the design of the drive and sense mode controller, is utilized. The fast settling behavior in the quadrature electronics is required to instantly cancel the quadrature signal when the phase difference between the drive and quadrature signals converges to zero during the mode-matching operation. If the quadrature signal is not cancelled at the time instant of no phase difference, the mode-matched gyroscope operation cannot be accomplished since the controller blocks, except the drive mode controller, saturates due to the quadrature signal that maximizes when the mode frequencies of the gyroscope are matched. Furthermore, a bandwidth is not considered during the design of the closed loop quadrature cancellation electronics since the quadrature error always exists at the drive mode resonance frequency in the system.

Considering the electronic blocks shown in Figure 3.17 and the first order envelope model of the sense mode of the gyroscope, the open loop transfer can be written as

$$H_{OL}(s) = \underbrace{\frac{A_Q}{1 + s/\beta_S}}_{H_{S,Q}(s)} K_{Demod.} H_{LPF}(s) \underbrace{\frac{K_I(1 + s\,K_P/K_I)}{s}}_{H_{PI}(s)} K_{Quad.} \qquad 3.21$$

In Equation 3.21, $K_{Demod.}$ is the demodulator gain, $H_{LPF}(s)$ is the transfer function of the second order low-pass filter, $H_{PI}(s)$ is the PI controller transfer function, and $K_{Quad.}$ is the voltage-to-force conversion gain at the quadrature electrodes that is obtained taking the derivative of $F_{Quad.}$ shown in Equation 3.17 with respect to ΔV which is the applied potential to the quadrature electrodes.

A similar approach, used in the drive and sense modes, is followed to optimize the behavior of the closed loop quadrature controller. The open loop analysis is first performed using the model parameters of the gyroscope (C05) shown in Table 3.2. The open loop transfer function of the quadrature controller can be written for the gyroscope (C05) as

$$H_{OL}(s) = \frac{8.1 * 10^7}{1 + s/27.56} * \frac{2}{\pi} * \frac{1 * 394784}{s^2 + 881.1s + 394784} * \frac{K_I(1 + s\,K_P/K_I)}{s} * 9.36 * 10^{-8} \qquad 3.22$$

where $2/\pi$ is the RMS value of the rectified quadrature signal with a unity demodulator gain. The gain of the low-pass filter is adjusted to be 1 with a cutoff frequency of 100 Hz. The main goal at the design of the quadrature controller is to obtain fast transient response time without degrading controller stability. During the design, first, the pole-zero cancellation is performed by adjusting the PI controller parameters to increase the settling time of the controller, and then the overshoot and phase margin are arranged to ensure controller stability through the adjustment of the amplitude of K_I. The parameters of K_I and K_P are adjusted to be 14.8 and 0.53, respectively, which provides sufficient phase margin, low settling time and small overshoot. Figure 3.18 show the bode plot of the open loop quadrature control electronics. The phase margin is set to 65.4°, which is in safe region for the stability. Figure 3.19 shows the step response of the closed loop quadrature controller. The quadrature cancellation controller settles in 16 msec with an overshoot of 5%.

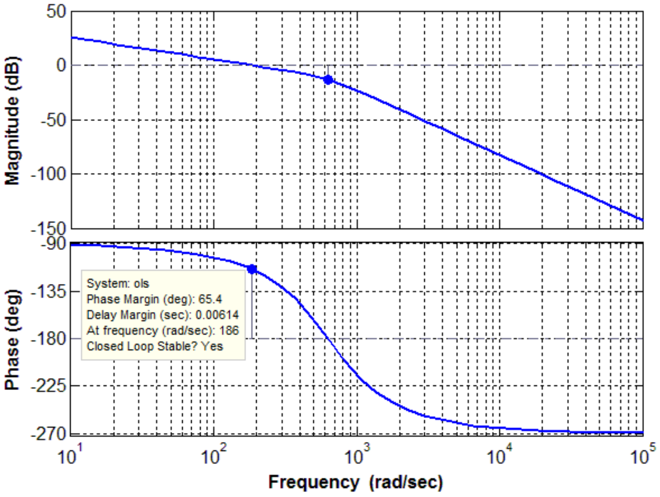

Figure 3.18: Bode plot of the open loop quadrature control electronics.

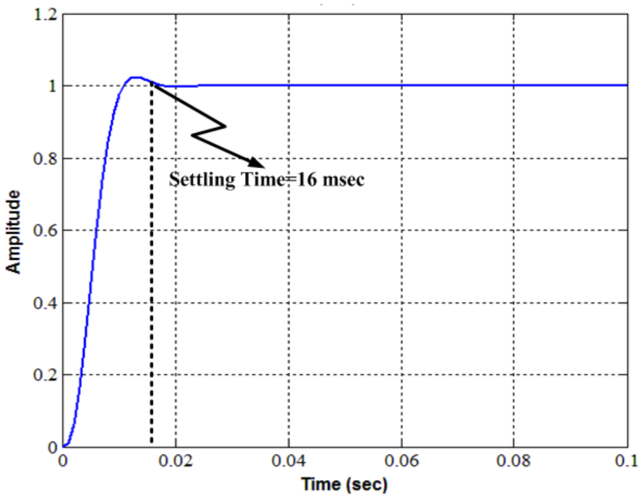

Figure 3.19: Step response of the closed loop quadrature controller.

The SIMULINK model, shown in Figure 3.20, is constructed to observe the transient response behavior of the quadrature controller. The aim of the controller is to cancel the quadrature error as high as possible to ensure proper mode-matching operation.

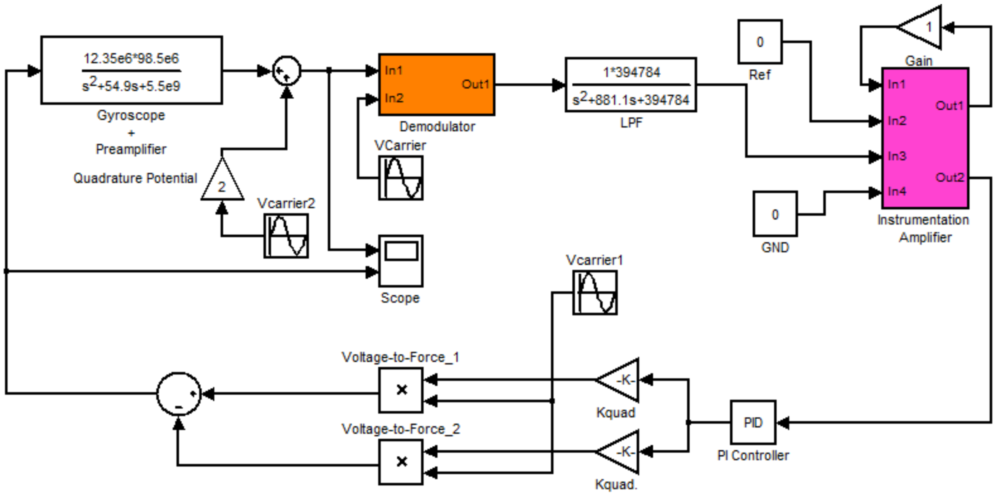

Figure 3.20: SIMULINK model of the closed loop quadrature controller.

Figure 3.21 shows the applied quadrature force to stop the sense mode displacement caused by the quadrature error at the system. The applied force is about 7x10^{-9} N under the mode-matched condition. The settling time of the closed loop quadrature controller is 16 msec, which is consistent with the result obtained by the open loop analysis.

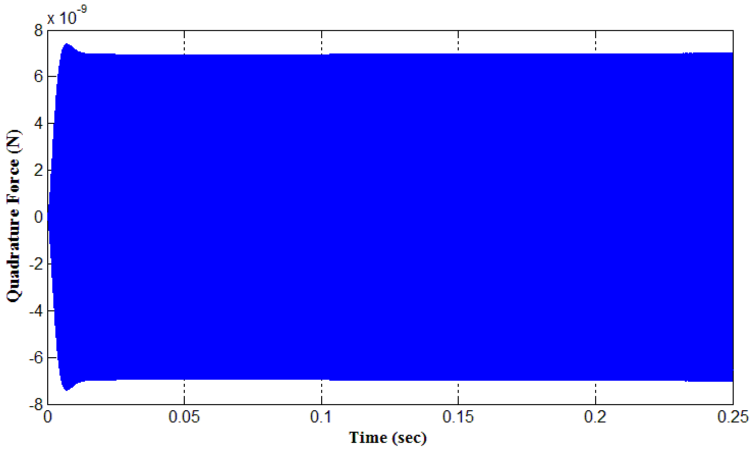

Figure 3.21: Applied quadrature force using to eliminate quadrature error at the system.

Figure 3.22 shows the sense pick signal in the presence of the applied quadrature force. The sense pick signal directly provides information about the quadrature error signal under the zero-rate condition. After the applied quadrature force, the sense pick is attenuated in time, and finally goes to zero as expected. This means that the sense mode displacement caused by the quadrature error is eliminated with the aid of the applied quadrature force created by applying differential DC potential to the quadrature cancellation electrodes.

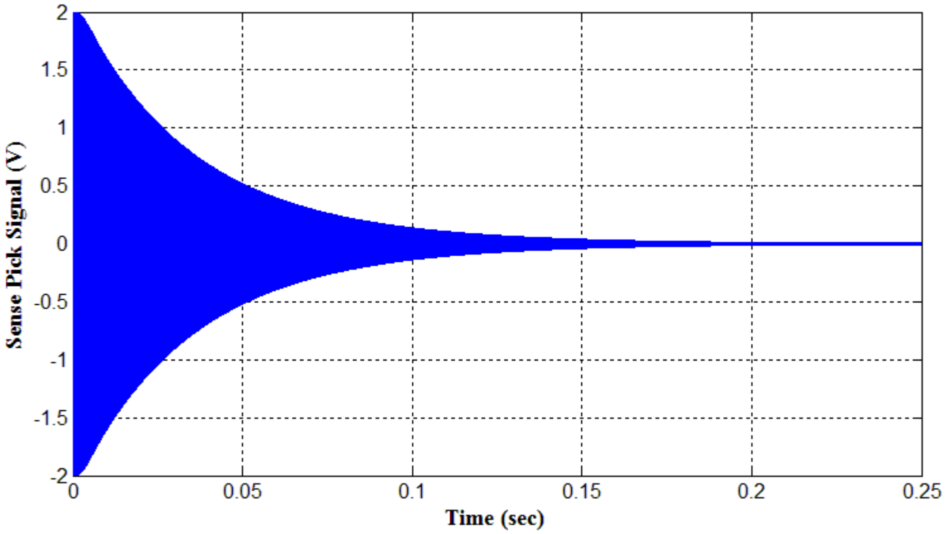

Figure 3.22: Sense pick signal in the presence of the applied quadrature force.

3.5 Mode-Matching Controller

The proposed automatic mode-matching system relies on the phase relationship between the drive and residual quadrature signals. The phase difference information between these signals is basically used as an indicator of the frequency mismatch amount between the resonance modes. The phase of the drive signal is always constant at the mode-matching system, but the quadrature signal phase can be changed via tuning capability of the sense mode. The phase behavior of the quadrature signal can be obtained from the sense mode dynamics since the quadrature error directly acts on the sense mode of the gyroscope. The sense mode of the gyroscope can be governed in the presence of the quadrature error by the following equation:

$$\frac{\mathrm{Y}(s)}{F_Q(s)} = \frac{1/m_S}{\left(s^2 + \frac{\omega_S}{Q_S}s + \omega_S{}^2\right)} \qquad 3.23$$

where $\mathrm{Y}(s)$ stands of the resultant sense mode displacement caused by the residual quadrature error force, and $F_Q(s)$ represents the residual quadrature error force. The residual quadrature error force directly acts on the sense mode dynamic at the drive mode resonance frequency, ω_D. Therefore, under the condition of the frequency mismatch, $\omega_D \neq \omega_S$, between the resonance modes, Equation 3.23 is equated to

$$\frac{\mathrm{Y}(j\omega_D)}{F_Q(j\omega_D)} = \frac{1/m_S}{-\omega_D{}^2 + j\frac{\omega_D\omega_S}{Q_S} + \omega_S{}^2} \qquad 3.24$$

From Equation 3.24 the nominal phase delay, $\emptyset_0$, at the quadrature signal can be directly derived from the sense mode response as

$$\emptyset_0 = \angle\left(\frac{\mathrm{Y}(j\omega_D)}{F_Q(j\omega_D)}\right) = -\tan^{-1}\left(\frac{1}{Q_S}\frac{\omega_D\omega_S}{(\omega_S{}^2 - \omega_D{}^2)}\right) \qquad 3.25$$

Equation 3.25 states that phase delay of the quadrature signal can be adjusted using the effect of the electrostatic spring constant on the sense mode of the gyroscope. Considering the electrostatic spring effect, the sense mode resonance frequency can be tuned as

$$\omega_S = \sqrt{\underbrace{\frac{k_{mech}}{m_S}}_{w_{S,mech}^2} - \frac{\alpha\varepsilon_0 H_0 L_0}{m_S {D_{gap}}^3} {V_t}^2} \qquad 3.26$$

In Equation 3.26, k_{mech} is the mechanical spring constant, α is the fringing field correction factor, ε_0 is the permittivity of free space, V_t is the tuning potential. Also, D_{gap} is the gap spacing, H_0 is the overlapped height, and L_0 is the overlapped length for the tuning electrodes. Inserting Equation 3.26 into Equation 3.25 the effective phase delay at the quadrature signal can be computed as

$$\emptyset_{eff} = -\tan^{-1}\left(\frac{1}{Q_S}\frac{\omega_D\sqrt{{w_{S,mech}}^2 - \frac{\alpha\varepsilon_0 H_0 L_0}{m_S {D_{gap}}^3}{V_t}^2}}{\left({\omega_{S,mech}}^2 - \frac{\alpha\varepsilon_0 H_0 L_0}{m_S {D_{gap}}^3}{V_t}^2 - {\omega_D}^2\right)}\right) \qquad 3.27$$

The effective phase delay expression for the quadrature signal clarifies the use of the residual quadrature signal for mode-matching. For the mode-matched gyroscope operation, the quadrature signal is adjusted to be in-phase with the drive signal by changing the phase of the quadrature signal with the aid of the tuning capability of the sense mode. Therefore, the main motivation behind the proposed automatic mode-matching architecture is to tune the sense mode resonance frequency with respect to the drive mode resonance frequency. In the scope of this thesis, there are two methods used to achieve tuning of the sense mode resonance frequency.

In the first phase of this study, the mode-matching is accomplished adjusting the proof mass potential of the modified fully-decoupled gyroscope shown in Figure 1.3. The fully-decoupled gyroscope does not have special frequency tuning electrodes. The proof mass potential provides an opportunity to tune the sense mode resonance frequency with respect to the drive mode resonance frequency with the aid of the varying gap type electrodes used in the sense mode. Figure 3.23 shows the simplified block diagram of the closed loop mode-matching controller that provides an ability to perform mode-matching by changing the proof mass potential. First, the residual quadrature and drive signals are directly obtained from the sense pick and drive pick electrodes through the preamplifiers. Then, the residual quadrature signal is demodulated with the 90° shifted version of the drive pick signal, which results in the rectified quadrature signal at the output of the demodulator. Next, the phase difference information between the residual quadrature and drive signals is obtained as a DC potential, called error signal, after low-pass filtering the envelope of the residual quadrature signal. The low pass filer together with the demodulator operates as a phase detector. The error signal is fed to the PI controller that generates a DC tuning potential. Following, the DC tuning potential is applied to the proof mass of the gyroscope after summing it with a fixed DC potential. The fixed DC proof mass potential is always supplied to the gyroscope in order to initiate the mode-matching operation. Hence, the proposed mode-matching controller provides the tuning of the sense mode resonance frequency until the phase difference between the residual quadrature and drive signals converges to zero, which indicates that the mode-matching has been accomplished.

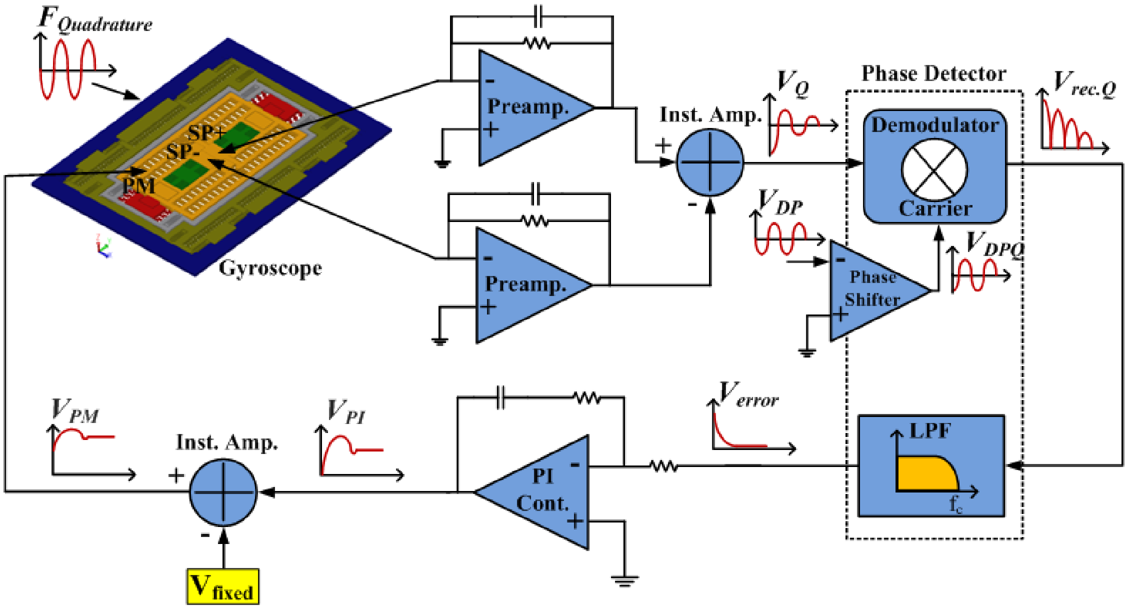

Figure 3.23: Simplified block diagram of the closed loop mode-matching controller that provides an ability to perform mode-matching by changing the proof mass potential.

In the proposed closed loop mode-matching controller, the proof mass variation directly affects the sense mode dynamics regarding the sense mode resonance frequency variation. The sense mode resonance frequency variation is resulted from a change in the sense mode electrostatic spring constant. Considering the effect of electrostatic spring constant on the sense mode resonance frequency, the sense mode dynamics with the preamplifier stage can be expressed by referring to Figure 3.23 under the zero-rate condition as

$$\frac{V_{SP,Quad.}(s)}{F_{Quad.}(s)} = \frac{1/m_S}{\left(s^2 + \frac{\omega_S}{Q_S}s + \left(\frac{k_{mech}}{m_S} - \left(\frac{N_1\alpha\varepsilon_0 H_0 L_0}{m_S {D_{gap}}^3} + \frac{N_1\alpha\varepsilon_0 H_0 L_0}{m_S {D_{antigap}}^3}\right)(V_{PM} \pm \Delta V)^2\right)\right)} \tag{3.28}$$

$$* \, (V_{PM} \pm \Delta V)\frac{\partial C_{SP}}{\partial y} s Z_{preamp.} A_{inst.amp.}$$

where ΔV is the tuning potential that is added to the fixed proof mass potential during mode-matching, ω_S/Q_S is a constant, which is not affected from the electrostatic spring constant variation because it is directly related with the damping factor and sense frame mass, and N_1 is the number of varying-gap type electrodes, used in the sense mode.

During mode-matching, the proof mass voltage changes until the frequency split between modes converges to zero, which states that the parameters of the sense mode dynamics vary until the mode-matching controller reaches the steady-state condition. Therefore, to understand the behavior of the proposed mode-matching controller and adjust the PI controller parameters, the closed loop analysis is performed for the modified fully-decoupled gyroscope of J01 instead of the open loop analysis. Table 5.1 and 5.2 show the model parameters of the modified fully-decoupled gyroscope (J01), which has a drive mode resonance frequency of 13906 Hz and sense mode quality factor of 2442. Figure 3.24 shows the SIMULINK model of the closed loop mode-matching controller that uses the proof mass potential to achieve mode-matching. In the SIMULINK model, the gyroscope is considered as a feedback mechanism, in which the sense mode resonance frequency is automatically updated by changing the proof mass potential until the phase difference between the residual quadrature and drive signals converges to zero. Also, the SIMULINK model includes the complete model of the gyroscope (J01), second order low-pass filter with 100 Hz cutoff frequency and gain of 1, and demodulator with a unity gain.

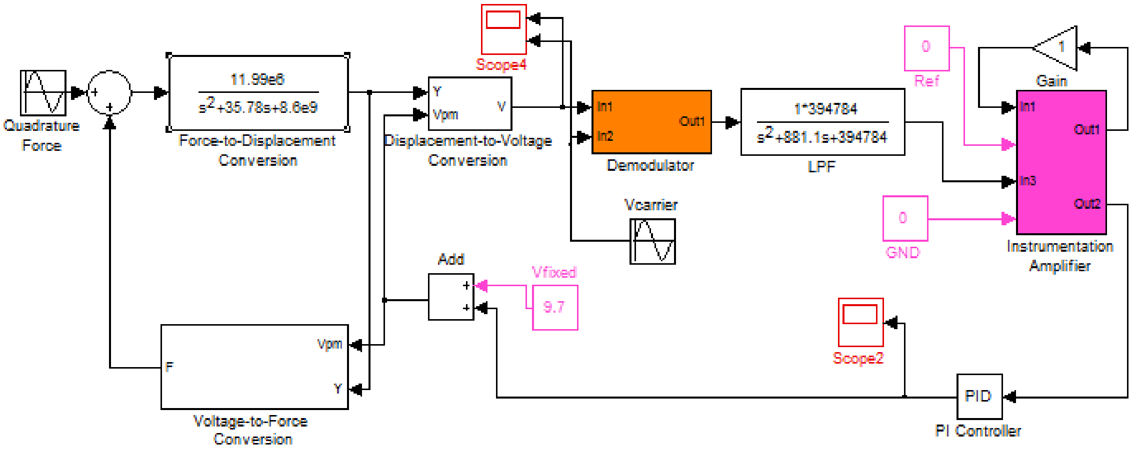

Figure 3.24: SIMULINK model of the closed loop mode-matching controller that uses the proof mass potential to achieve mode-matching.

Figure 3.25 and 3.26 show the simulated tuning potential and phase detector output for the mode-matching controller, shown in Figure 3.23, during the mode-matching operation as the initial frequency split between the modes changes with 50, 100, and 150 Hz, respectively. Referring to Figure 3.25 and 3.26, the settling time of the controller directly depends on the initial frequency split between the resonance modes of the gyroscope. When the initial frequency split is higher at the start-up of the mode-matching system, the mode-matching system requires more time to settle. When the controller reaches the steady-state condition, the phase difference between the residual quadrature and drive signals converges to zero as expected, which is clearly shown in Figure 3.26. Considering the transient response characteristic of the proposed closed loop mode-matching controller, the proportional and integral gain parameters are adjusted to 0.7 and 10, respectively.

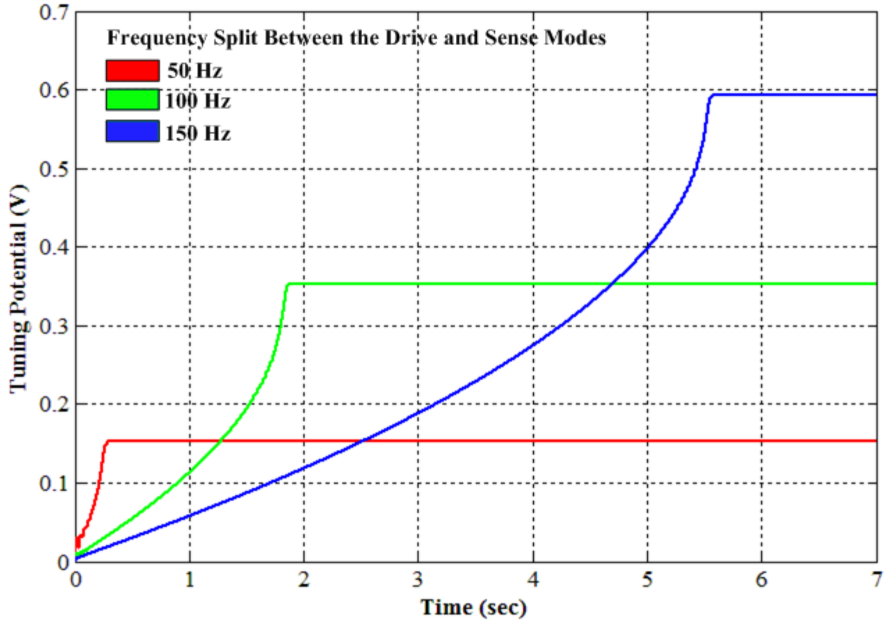

Figure 3.25: Simulated tuning potential for the mode-matching controller, shown in Figure 3.23, during the mode-matching operation as the initial frequency split between the resonance modes of the gyroscope changes with 50, 100, and 150 Hz, respectively.

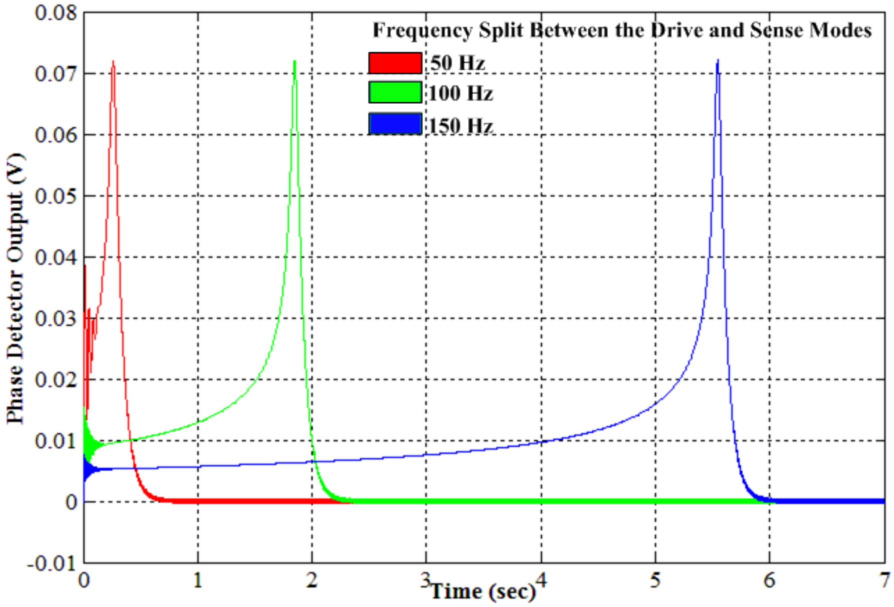

Figure 3.26: Simulated phase detector output for the mode-matching controller, shown in Figure 3.23, during the mode-matching operation as the initial frequency split between the resonance modes of the gyroscope changes with 50, 100, and 150 Hz, respectively.

In the second phase of this study, mode-matching is performed using the special frequency tuning electrodes, demonstrated in Section 2.7. The frequency tuning electrodes (FTEs) provide an opportunity to automatically tune the sense mode resonance frequency, independently from the proof mass potential. The gain of the gyroscope at resonance directly depends on the proof mass potential, clearly shown in Equation 3.3, 3.12, 3.18, and 3.28. Therefore, the proof mass potential variation leads to a change at the closed loop gain of the mode-matching controller, which might degrade the stability of the mode-matching controller reducing the phase margin of the controllers. The proposed closed loop mode-matching controller described above does not suffer from the proof mass potential variation since the tuning potential, added to the fixed proof mass potential, is quite small compared to the fixed proof mass potential, which does not cause significant closed loop gain variations at the mode-matching system. To totally eliminate the proof mass dependency of the mode-matching system, the frequency tuning electrodes are designed and placed in the single-mass fully-decoupled gyroscope, shown in Figure 2.8. Figure 3.27 shows the proposed closed loop mode-matching controller that is capable of matching the resonance mode frequencies of the gyroscope using the frequency tuning electrodes that also improves the operational stability in the presence of environmental vacuum or temperature variations because the sensitivity of the scale factor to the proof mass potential is totally eliminated with the aid of the frequency tuning electrodes. The operation principle of the proposed closed loop mode-matching controller is similar with the mode-matching controller shown in Figure 3.23. However, in this case, the PI controller output is directly applied to the frequency tuning electrodes to tune the sense mode resonance frequency with respect to the drive mode resonance frequency, differently from the mode-matching implementation based on the proof mass potential described above. The proof mass potential is always supplied to the gyroscope during the mode-matching operation, similar with the first method, because it is always required to initiate the mode-matching operation, but it is kept constant to eliminate the closed loop gain variations of all controllers used in the mode-matching system for stability concern.

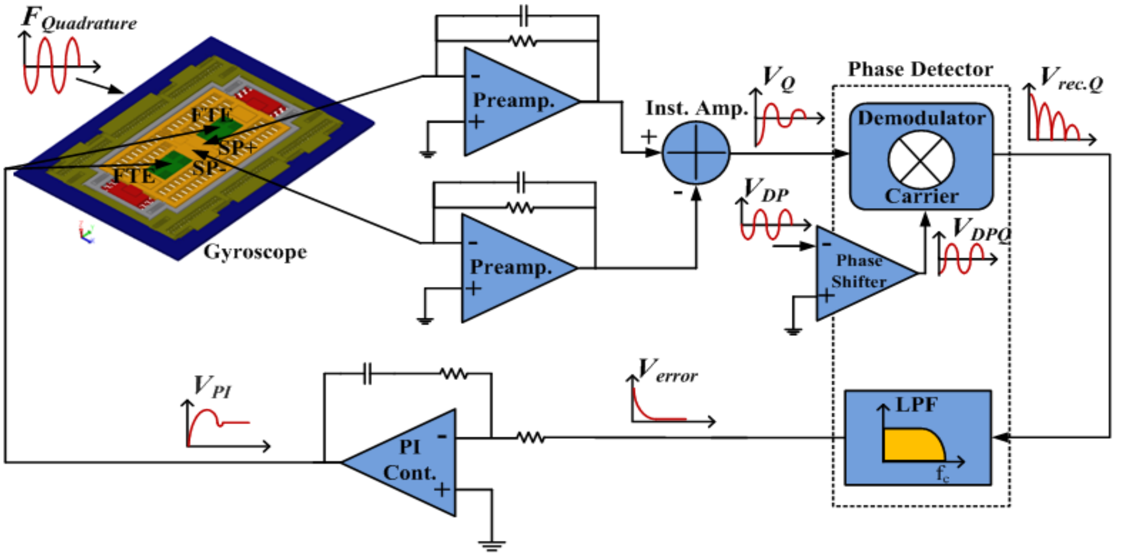

Figure 3.27: Proposed closed loop mode-matching controller that is capable of matching the resonance modes of the gyroscope using the frequency tuning electrodes.

Considering the effect of frequency tuning electrodes on the sense mode resonance frequency of the gyroscope, the sense mode dynamics with the preamplifier stage can be written by referring to Figure 3.27 under the zero-rate condition as

$$\frac{V_{SP,Quad.}(s)}{F_{Quad.}(s)} =$$

$$\frac{1/m_S}{\left(s^2+\frac{\omega_S}{Q_S}s+\left(\frac{k_{eff}}{m_S}-2\frac{N_2\alpha\varepsilon_0 H_0 L_0}{m_S D_{gap}{}^3}(V_{PM}\pm\Delta V)^2\right)\right)}V_{PM}\frac{\partial C_{SP}}{\partial y}sZ_{preamp.}A_{inst.amp.} \tag{3.29}$$

where N_2 is the number of the frequency tuning electrodes, ΔV is the tuning potential applied to the frequency tuning electrodes, and k_{eff} is the effective spring constant for the sense mode, which can be expressed without ignoring the effect of antigap at the sense mode electrodes as

$$k_{eff} = k_{mech} - N_1\alpha\varepsilon_0 H_0 L_0\left(\frac{1}{\left(D_{gap}-y\right)^3}+\frac{1}{\left(D_{antigap}+y\right)^3}\right)V_{PM}{}^2 \tag{3.30}$$

In Equation 3.30, N_1 is the number of the sense electrodes. It is clearly shown in Equation 3.29 that the only changing parameter is the sense mode resonance frequency in the sense mode dynamics thanks to the proof mass potential that is kept constant during the mode-matching operation.

To analyze the behavior of the proposed closed loop mode-matching controller and adjust the PI controller parameters, the closed loop analysis is performed using the parameters of the single-mass fully-decoupled gyroscope (C05) instead of the open loop analysis constructing a SIMULINK model due to the nonlinear sense mode dynamics, shown in Equation 3.29. Figure 3.28 shows the SIMULINK model of the closed loop mode-matching controller, in which the tuning of the sense mode resonance frequency is performed using the frequency tuning electrodes. In the SIMULINK model, the effect of the electrostatic spring constant on the sense mode resonance frequency is modeled considering the tuning potential applied to the frequency tuning electrodes and proof mass potential. Also, the SIMULINK model includes the complete model of the gyroscope (C05), second order low-pass filter with 100 Hz cutoff frequency and gain of 1, and demodulator with a unity gain.

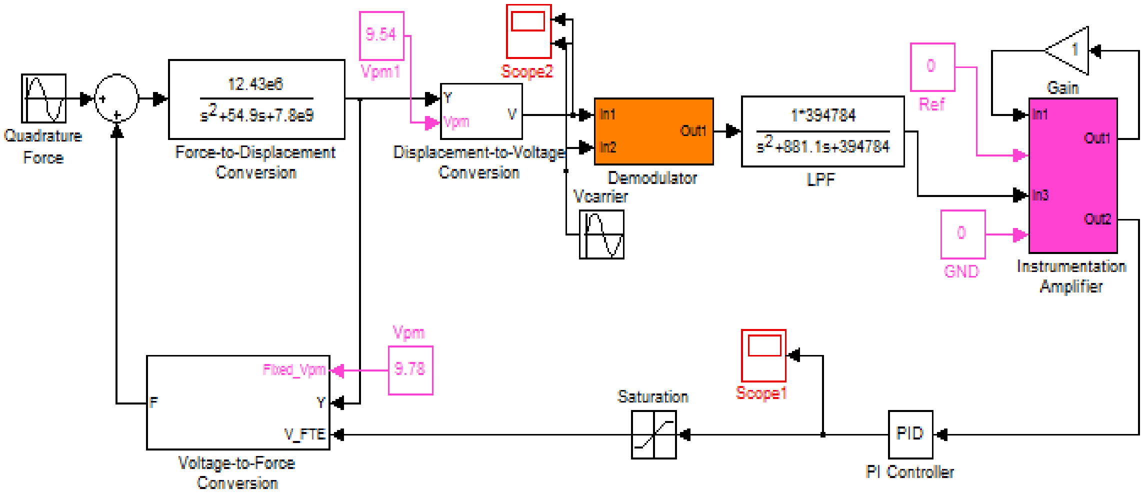

Figure 3.28: SIMULINK model of the closed loop mode-matching controller, in which the tuning of the sense mode resonance frequency is performed using the frequency tuning electrodes.

Figure 3.29 shows the simulated tuning potential and phase detector output for the mode-matching controller, shown in Figure 3.27, during the mode-matching operation as the initial frequency split between the resonance modes of the gyroscope changes with 50, 100, and 150 Hz, respectively.

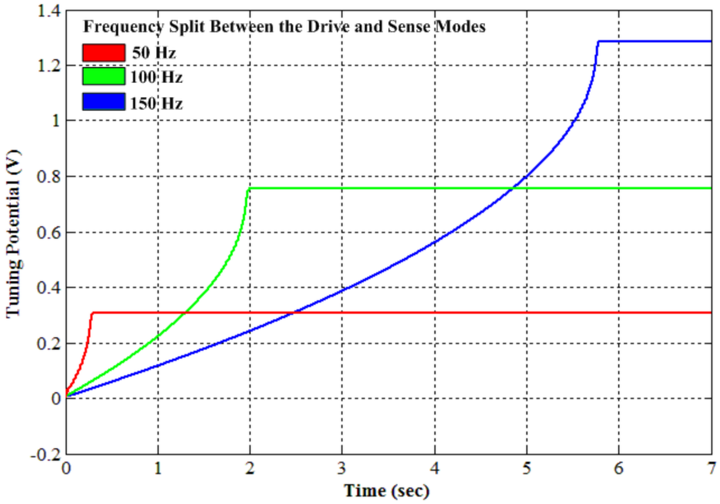

Figure 3.29: Simulated tuning potential for the mode-matching controller, shown in Figure 3.27, during the mode-matching operation as the initial frequency split between the resonance modes changes with 50, 100, and 150 Hz, respectively.

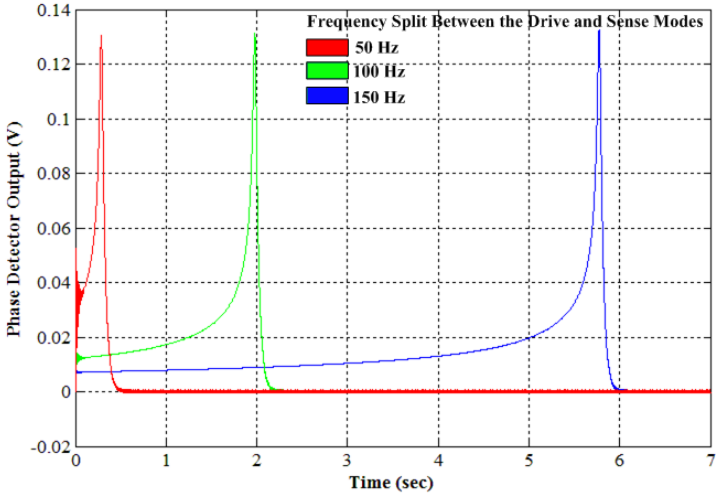

Figure 3.30: Simulated phase detector output for the mode-matching controller, shown in Figure 3.27, during the mode-matching operation as the initial frequency split between the resonance modes of the gyroscope changes with 50, 100, and 150 Hz, respectively.

The effect of the sense mode electrodes on the electrostatic spring constant is nearly two times higher than the frequency tuning electrodes for the same tuning potential due to the number of electrodes used to tune the sense mode resonance frequency. Therefore, the amplitude of the required tuning potential applied to the frequency tuning electrodes, shown in Figure 3.29, is nearly two times higher than the tuning potential applied to the sense mode electrodes, shown in Figure 3.25. Referring to Figure 3.30, the phase detector output converges to zero when mode-matching is accomplished as expected. The proportional and integral gain parameters are adjusted to 0.54 and 15, respectively.

It should be noted that the settling time of the mode-matching controller, used in the proposed two methods for matching of the resonance mode frequencies, can be decreased by increasing the closed loop gain of the mode-matching controller through the adjustment of the integral (K_I) and proportional (K_P) gains of the PI controller. When increasing the closed loop gain of the mode-matching controller, the steady-state stability should be monitored because the phase margin of the controller may degrade at the steady-state condition. Figure 3.31 shows the simulated tuning potential for the mode-matching controller with different values of K_P and K_I, shown in Figure 3.27, in the presence of 50 Hz initial frequency split.

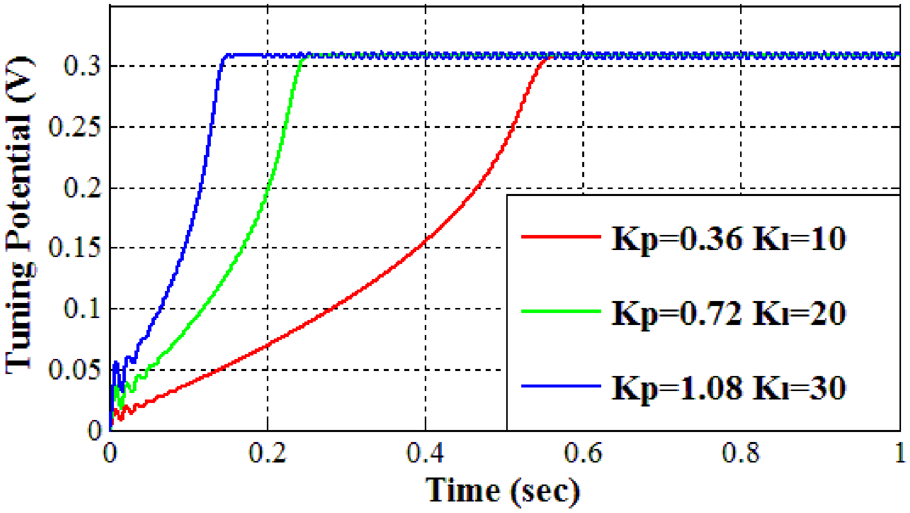

Figure 3.31: Simulated tuning potential for the mode-matching controller, shown in Figure 3.27, with different values of K_P and K_I in the presence of 50 Hz initial frequency split.

As seen in Figure 3.31, the settling time of the mode-matching controller decreases with increasing K_P and K_I values thanks to an increase of the closed loop gain. However, the controller stability degrades with increasing closed loop gain under the steady-state condition due to the degradation of the phase margin of the controller. This degradation results in an oscillation around the required tuning potential for K_P of 1.08 and K_I of 30. If K_P and K_I are increased further above 1.08 and 30, respectively, the amplitude of the oscillation increases, which interferes with the frequency matching condition. Therefore, the closed loop gain should be adjusted considering the stability of the controller under the steady-state condition.

Figure 3.32 shows the simulated transient behavior of the drive and sense mode outputs of the gyroscope in the presence of the Coriolis force during the mode-matching operation that is performed for an initial frequency split of 60 Hz. As observed, when the frequency split between the modes converges to zero, the amplitude of the sense mode output significantly increases due to the sensitivity improvement, and the phase difference between the sense and drive mode signals becomes 90°, which ensures that mode-matching is accomplished.

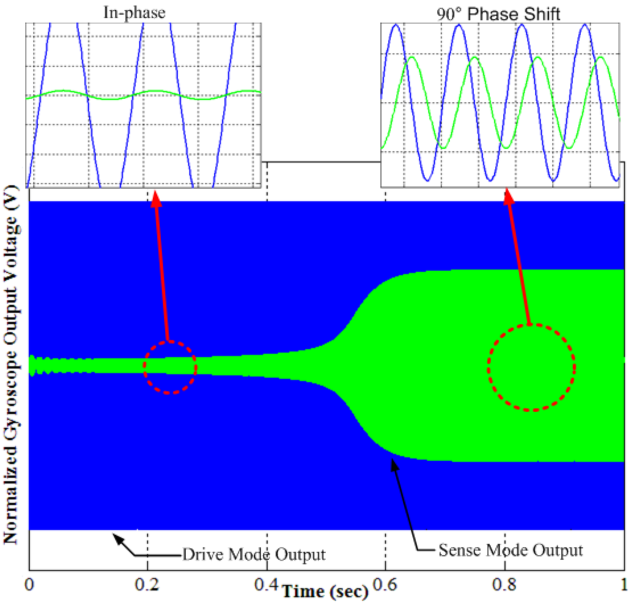

Figure 3.32: Simulated transient behavior of the drive and sense mode outputs of the gyroscope in the presence of a Coriolis force during the mode-matching operation that is performed for an initial frequency split of 60 Hz.

3.6 Noise Performance Analysis of the Mode-Matching System

Noise performance of the gyroscope directly affects the amount of a minimum detectable angular rotation rate. Therefore, it is a major concern in the gyroscope operation. The drive mode controller has an ignorable effect on the noise performance of the system, so the noise performance of the system is directly determined through the analysis of the sense mode controller. There are two major noise components, which are the electronic noise and mechanical (Brownian) noise, exist in the gyroscope operation. Figure 3.33 shows the closed loop sense mode controller of the gyroscope with an associated noise sources.

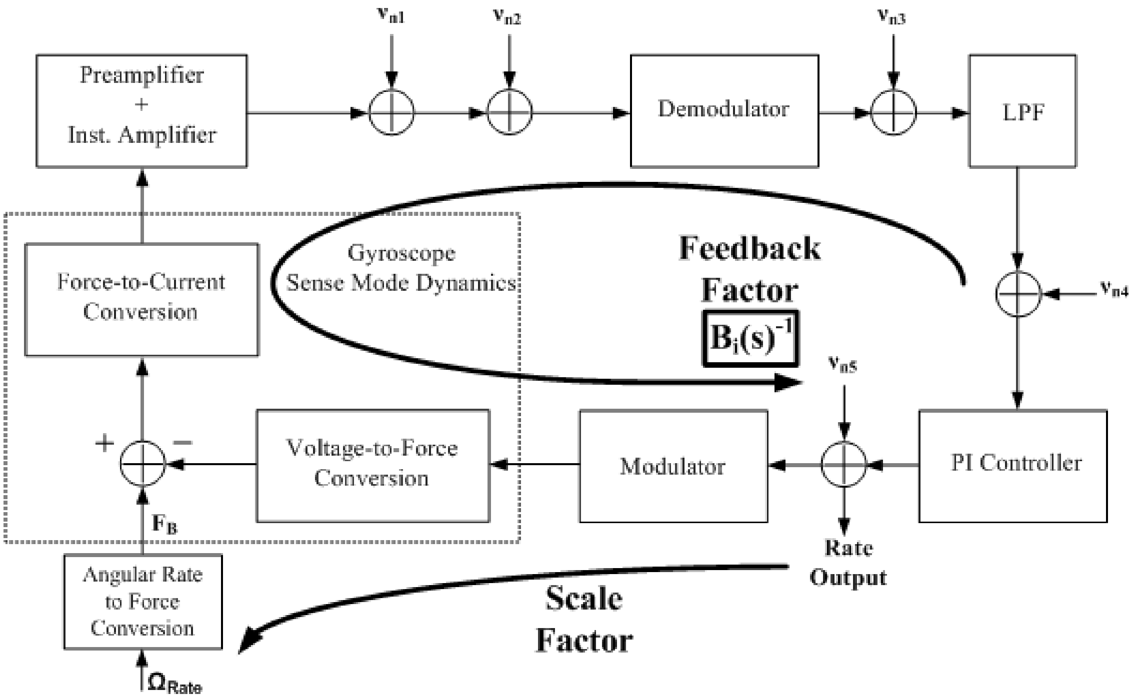

Figure 3.33: Closed loop sense mode controller of the gyroscope with an associated noise sources.

Each of the noise sources contribute to the rate output with a different loop gain due to the feedback mechanism. Referring to Figure 3.33, the noise transfer function for a declared noise sources, $v_{n,i}$, can be expressed with a well-known equation as

$$H_i(s) = \frac{A_i(s)}{1 + \beta_i(s) A_i(s)} \tag{3.31}$$

where $A_i(s)$ and $\beta_i(s)$ are the feed-forward gain and feedback factor for each individual noise source, respectively. In Equation 3.31, the multiplication of the feed-forward gain and feedback factor represents the gain of the open loop transfer function that is much greater than unity gain in the proposed sense mode controller. Therefore, Equation 3.31 for each individual noise sources can be simplified as a simple gain stage to

$$H_i(s) = \frac{1}{\beta_i(s)} \tag{3.32}$$

The system bandwidth is determined by the sense mode controller described in Section 3.3. All of the electronic blocks show a flat gain response within the system bandwidth except of the PI controller, but the PI controller does not have any effect on the feedback path. Furthermore, on the condition of low frequency mismatch between the modes of the gyroscope sense mode dynamics of the gyroscope behaves as a first order system. Therefore, the gain response of the gyroscope is dependent on the frequency due to the resonance characteristics of the first order sense mode dynamics. Therefore, the feedback factor gain, $\beta_i(s)$, is represented as a frequency dependent function under the low frequency mismatch condition. However, if the frequency mismatch increases, it can be simplified to a simple gain stage since the frequency dependent characteristic substantially disappears.

At the proposed mode-matching system, the noise performance of the system is analyzed with the following procedure. Referring to Figure 3.33, first, the noise sources, associated with the sense mode controller, are specifically determined, and then these noise sources are referred to the rate output after dividing them by the feedback gain, $\beta_i(s)$. Next, the rate-equivalent input referred noise is found after dividing the rate-equivalent output referred noise by the scale factor. Table 3.3 shows the noise sources associated with the sense mode controller and the feedback factor gains for each of the individual noise sources.

Table 3.3: Noise sources associated with the sense mode controller and the feedback factors for each of the individual noise sources.

$\boldsymbol{v_{n,i}}$	**Noise Source**	**Feedback Factor Gain, $\boldsymbol{\beta_i(s)}$**
$\boldsymbol{v_{n1}}$	Output Referred Noise of the Preamplifier and Instrumentation Amplifier	$K_s(s) * K_{Mod.}$
$\boldsymbol{v_{n2}}$	Input Referred Noise of the Demodulator	$K_s(s) * K_{Mod.}$
$\boldsymbol{v_{n3}}$	Input Referred Noise of the Low-Pass Filter	$K_s(s) * K_{Mod.} * K_{Demod.}$
$\boldsymbol{v_{n4}}$	Input Referred Noise of the PI Controller	$K_s(s) * K_{Mod.} * K_{Demod.} * K_{LPF}$
$\boldsymbol{v_{n5}}$	Input Referred Noise of the Modulator	1
$\boldsymbol{F_B}$	Mechanical Brownian Noise	$K_{V/F} * K_{Mod.}$

In Table 3.3, $K_s(s)$ is the frequency dependent sensor gain including the effect of the preamplifier and instrumentation amplifier, $K_{Mod.}$ is the modulator gain, $K_{Demod.}$ is the demodulator gain, K_{LPF} is the low-pass filter gain, and finally, $K_{V/F}$ is the gain of the voltage-to force conversion block.

To make a quantitative noise analysis at the system, the values of the noise sources declared in Table 3.3 should be separately extracted. First, the electronic noise contributions to the rate output of the sense mode controller are performed. The front-end electronics are composed of the preamplifier and instrumentation amplifier, constructed using AD8608 (Preamplifier) and AD8222 (Instrumentation amplifier) from Analog Devices, respectively. Referring to Figure 3.1, the noise expression of the output referred noise of the front-end electronics can be presented as

$$v_{n1} = \left[2i_{n,preamp}{}^{2}\left(\frac{1}{sC_{preamp.}}\right)^{2} + 2i_{n,Rpreamp.}{}^{2}\left(\frac{1}{sC_{preamp.}}\right)^{2} \right.$$

$$\left. +2v_{n,preamp}{}^{2}\left(1+\frac{\left(C_{SP}+C_{Par.}+C_{in,AD8608}\right)}{C_{preamp.}}\right)^{2} + v_{n,Inst.Amp.}{}^{2}\right]^{1/2} G_{Inst.Amp.} \qquad 3.33$$

In Equation 3.33, the multiplication constant of 2 comes from the differential reading of the sense mode controller. Table 3.4 shows the electronic noise densities associated with the front-end electronics with typical sensor parameters.

Table 3.4: Electronic noise densities associated with the front-end electronics with typical sensor parameters [46, 47].

Parameter	Description	Value
$\boldsymbol{\omega_S}$	Operating Frequency	12 kHz
$\boldsymbol{C_{preamp.}}$	Preamplifier Capacitance	3.9 pF
$\boldsymbol{C_{SP}}$	Sense Mode Output Capacitance	5.4 pF
$\boldsymbol{C_{in,AD8608}}$	Input Capacitance of AD8608	11.4 pF
$\boldsymbol{C_{Par.}}$	Parasitic Capacitance (Wire Bonding)	1 pF
$\boldsymbol{i_{n,preamp.}}$	Input Referred Current Noise Density of AD8608	10fA/√Hz
$\boldsymbol{v_{n,preamp}}$	Input Referred Voltage Noise Density of AD8608	6.5nV/√Hz
$\boldsymbol{i_{n,Rpreamp.}}$	Input Referred Current Noise Density of Preamplifier Resistance	5.94fA/√Hz
$\boldsymbol{v_{n,Inst.Amp.}}$	Input Referred Voltage Noise Density of AD8222	8.81nV/√Hz
$\boldsymbol{G_{Inst.Amp.}}$	Instrumentation Amplifier Gain	20.3

Inserting the values in Table 3.4 into Equation 3.33, the output referred noise of the front-end electronics is calculated to be 1.49µV/√Hz, which is not the effective noise at the output of the front-end electronics due to the noise folding effect of the switching demodulator. The effective output referred noise of the front-end electronics, v_{n1}, is calculated to be 1.97µV/√Hz for the same circuitry regarding the effect of noise folding as described in [48]. After the front-end electronics, AD630 (Modulator/Demodulator) and AD8630 (Low-pass filter/PI controller) are used in the sense mode controller. However, there is no available noise information in the datasheet of the AD630 [49], but it can recover signal from 100dB noise. Therefore, it is assumed to be the noise contribution of taken to be zero during the noise calculations. After the demodulation, the AC signal is converted to DC through the low-pass filter. At DC-band, the flicker noise becomes a dominant noise source, but AD8630, used to construct low-pass filter, has a corner frequency of 1.2 Hz calculated in [39]. This corner frequency makes it a better choice for DC signal processing. The flicker noise contribution of AD8630 is ignored during the noise calculations thanks to the corner frequency that is quite smaller than the corner frequency of the typical op-amps, around 500Hz. Only voltage noise density of it is taken into account during the noise calculations, which is equal to 22nV/√Hz [50]. In addition, AD8630 is also used to construct PI controller for DC signal processing. Noise density of the PI controller is similar with the low-pass filter.

The total electronic noise at the rate output of the sense mode controller can found by separately summing the contribution of the each noise source, shown in Figure 3.33, in the power domain since the noise sources are uncorrelated with each other. Considering the feedback factor gains, the total electronic noise at the rate output can be calculated using the following expression.

$$v_{n,total} = \sqrt{\left(\frac{v_{n1}}{\beta_1(s)}\right)^2 + \left(\frac{v_{n2}}{\beta_2(s)}\right)^2 + \left(\frac{v_{n3}}{\beta_3(s)}\right)^2 + \left(\frac{v_{n4}}{\beta_4(s)}\right)^2 + \left(\frac{v_{n5}}{\beta_5(s)}\right)^2} \qquad 3.34$$

Dividing Equation 3.34 by the scale factor, the rate-equivalent input referred electronic noise can be directly expressed as

$$\Omega_{n,electronics} = \frac{v_{n,total}}{Scale\ Factor} \qquad 3.35$$

The rate-equivalent input referred noise directly indicates the amount of the minimum detectable angular rotation rate. Therefore, the rate-equivalent input referred noise is taken to be criterion to evaluate the quality of the system.

Besides the electronic noise, the mechanical Brownian noise denoted by F_B, shown in Figure 3.33**,** has an effect on the rate output of the sense mode controller. It can be formulated in terms of force by

$$F_B = \sqrt{4k_B T \frac{m_S \omega_S}{Q_S}} \tag{3.36}$$

where k_B is the Boltzmann's constant, and T is the ambient temperature. The rate-equivalent input referred mechanical Brownian noise can be directly calculated by dividing it to a Coriolis force. For a unity angular rotation rate (π/180), it can be expressed as

$$\Omega_{n,mechanical} = \frac{\sqrt{4k_B T \frac{m_S \omega_S}{Q_S}}}{2m_{PM}(\pi/180)\omega_D X_D} \tag{3.37}$$

Rearranging the terms inside Equation 3.37, the rate-equivalent input referred mechanical noise, $\Omega_{n,mechanical}$, can be simplified to

$$\Omega_{n,mechanical} = \frac{180}{\pi X_D} \sqrt{\frac{k_B T}{Q_S \sqrt{k_S m_S}} \frac{m_S \omega_S}{m_{PM} \omega_D}} \tag{3.38}$$

Total rate-equivalent input referred noise at the system is calculated by combining the mechanical Brownian and electronic noises in the power domain since they are uncorrelated. It can be expressed as

$$\Omega_{n,total} = \sqrt{\Omega_{n,mechanical}{}^2 + \Omega_{n,electronics}{}^2} \tag{3.39}$$

Referring to Equation 3.35, 3.38, and 3.11, the mechanical and electronic noises are inversely proportional with the drive mode displacement, X_D. Therefore, the reduction of the total rate-equivalent noise at the rate output can be achieved by increasing the drive mode displacement. Also, the increment at the sense mode quality factor, Q_S, provides an improvement in total rate-equivalent input referred noises. In the aspect of the electronic noise, the increment of sense mode quality factor provides an enhancement at the feedback factor gains, which resulting in a reduction at the electronic noise. In the aspect of the mechanical noise, Equation 3.38 states that the mechanical noise improves at the rate output with an increase in the sense mode quality factor.

To better understand the effect of the mode-matching on the noise performance, the noise analysis is performed using the single-mass fully-decoupled gyroscope of C05 under the condition of the mode-matched and 200 Hz mismatched conditions. Table 3.5 shows the parameters of the gyroscope (C05) used in noise calculations.

Table 3.5: Parameters of the gyroscope (C05) used in noise calculations.

Parameter	**Value**
Operating Frequency, ω_D	11805 Hz
Sense Mode Quality Factor, Q_S	1350
Mass of Sense Frame, m_S	8.04e-8 kg
Mass of Proof mass Frame, m_{PM}	3.41e-8 kg

In order to achieve a consistent comparison between the mismatch and mode-matched conditions, feedback factor gains should be simplified to a simple gain stage as an independent of the frequency for the mode-matched case. On the condition of a constant angular rate input applied to the system, feedback factor gains can be represented as a simple gain stage. Providing the constant angular rate to the system, the feedback factors and noise densities of each related electronic noise sources for the mode-matched and 200 Hz mismatched gyroscope operations are presented in Table 3.6.

Table 3.6: Feedback factors and noise densities of each related electronic noise source.

Parameter	**Noise Density**	**Feedback Factor Gain, β_i**	
		Mode-Matched	**Mismatch (200 Hz)**
$\boldsymbol{v_{n1}}$	1.97μV/√Hz	$\underbrace{48.5}_{K_S} * \underbrace{4/\pi}_{K_{Mod.}}$	$\underbrace{1.05}_{K_S} * \underbrace{4/\pi}_{K_{Mod.}}$
$\boldsymbol{v_{n2}}$	0	$\underbrace{48.5}_{K_S} * \underbrace{4/\pi}_{K_{Mod.}}$	$\underbrace{1.05}_{K_S} * \underbrace{4/\pi}_{K_{Mod.}}$
$\boldsymbol{v_{n3}}$	22nV/√Hz	$\underbrace{48.5}_{K_S} * \underbrace{4/\pi}_{K_{Mod.}} * \underbrace{4/\pi}_{K_{Demod.}}$	$\underbrace{1.05}_{K_S} * \underbrace{4/\pi}_{K_{Mod.}} * \underbrace{(4/\pi)}_{K_{Demod.}}$
$\boldsymbol{v_{n4}}$	22nV/√Hz	$\underbrace{48.5}_{K_S} * \underbrace{4/\pi}_{K_{Mod.}} * \underbrace{4/\pi}_{K_{Demod.}} * \underbrace{6.56}_{K_{LPF}}$	$\underbrace{1.05}_{K_S} * \underbrace{4/\pi}_{K_{Mod.}} * \underbrace{4/\pi}_{K_{Demod.}} * \underbrace{6.56}_{K_{LPF}}$
$\boldsymbol{v_{n5}}$	0	1	1

Using Equation 3.34 and the parameters listed in Table 3.5, the total rate-equivalent output referred noise is first calculated to be 0.032μV/√Hz for the mode-matched condition and 1.474μV/√Hz for the 200 Hz mismatched condition. The rate-equivalent input referred electronic noise can be obtained using Equation 3.35. Using Equation 3.11, the scale factor of the gyroscope is calculated to be 2.2mV/°/sec for the drive mode displacement of 4.5μm and proof mass potential of 10 V. The scale factor is same for the mode-matched and mismatched conditions thanks to the frequency tuning electrodes. The rate-equivalent input referred electronic noise is obtained as 0.052 °/hr/√Hz for the mode-matched condition and 2.412 °/hr/√Hz for the 200 Hz mismatched condition.

Second, using Equation 3.38 and parameters listed in Table 3.5, the rate-equivalent input referred mechanical noise is calculated to be 2.445 °/hr/√Hz for the mode-matched condition and 2.507 °/hr/√Hz for the 200 Hz mismatched condition. Table 3.8 shows the summary of the calculated total-rate equivalent input referred electronic and mechanical Brownian noise densities of the gyroscope (C05) for the mode-matched and 200 Hz mismatched conditions.

Table 3.7: Summary of the calculated total-rate equivalent input referred electronic and mechanical Brownian noise densities of the gyroscope (C05) for the mode-matched and 200 Hz mismatched conditions.

Gyro ID	**Rate-Equivalent Electronic Noise Density (°/hr/√Hz)**		**Rate-Equivalent Mechanical Noise Density (°/hr/√Hz)**	
	Mismatch (200 Hz)	**Mode-Matched**	**Mismatch (200 Hz)**	**Mode-Matched**
C05	2.412	0.052	2.507	2.445

Using Equation 3.39, the total rate-equivalent noise is calculated to be 2.445 °/hr/√Hz for the mode-matched condition and 3.478 °/hr/√Hz for the 200 Hz mismatched condition. As a rule of thumb, the angle random walk (ARW) performance of the gyroscope can be expressed as

$$ARW = \Omega_{n,total}(White\ Noise\ Density) * \left(\sqrt{2}\right)^{-1} \qquad 3.40$$

Table 3.8 shows the summary of the calculated total-rate equivalent input referred noise densities and the corresponding ARW values of the gyroscope (C05) for the mode-matched and 200 Hz mismatched conditions.

Table 3.8: Summary of the calculated total-rate equivalent input referred noise densities and the corresponding ARW values of the gyroscope (C05) for the mode-matched and 200 Hz mismatch conditions.

Gyro ID	**Rate-Equivalent Total Noise Density**		**ARW**	
	Mode-Matched	**Mismatch (200 Hz)**	**Mode-Matched**	**Mismatch (200 Hz)**
C05	3.478 °/hr/√Hz	2.445 °/hr/√Hz	~0.041 °/√hr	~0.029 °/√hr

It is verified from the theoretical noise analysis that the rate-equivalent electronic noise is almost totally suppressed under the mode-matched gyroscope operation compared to the mismatched gyroscope operation thanks to the sensitivity improvement of the sensor. Also, all of the electronic noises, including flicker and white noises, are shaped by the resonance characteristics of the gyroscope under the mode-matched condition.

3.7 Summary

This chapter mainly provides a detailed analysis of the controller design for the vibratory MEMS gyroscopes. First, resistive and capacitive type preamplifiers are discussed regarding the operation principles. Then, the closed loop drive, sense, and quadrature controller design are introduced with the following procedures. 1) The transfer function of the gyroscope is derived identifying the model parameters of the gyroscope through the resonance tests. 2) Open loop analysis is performed to determine the controller parameters, which are required to ensure stable gyroscope operation. 3) Closed loop analysis is performed to investigate the transient behavior of the proposed closed loop controllers by constructing SIMULINK model, in which the complete model of the sensor is used. Next, the proposed mode-matching method with associated mathematical equations and the mode-matching controller design is introduced in a detailed manner. Closed loop analysis of it is performed by constructing SIMULINK model to ensure stable mode-matched gyroscope operation. Finally, the noise performance of the mode-matching system is carried out using the parameters of the gyroscope (C05) for mode-matched and mismatch conditions.

CHAPTER 4

FABRICATION OF MEMS GYROSCOPES

The gyroscopes studied in this thesis are fabricated through SOG (silicon-on-glass) micromachining process using an SOI (silicon-on-insulator) wafer. Basically, the SOG process is the way of fabricating the sensors, such as accelerometers, resonators, and gyroscopes, by means of an anodic bonding of a silicon wafer to a glass wafer. In the process, first, the glass wafer is processed to form recesses and pad metallization, and then it is anodically bonded with the silicon wafer. The formation of the device layer is performed after the anodic bonding using deep-reactive-ion-etching (DRIE) that enables to achieve high-aspect-ratio structures in the micromachining technology. However, in this process, the etching at the formation of the device layer cannot be controlled due to the effect of an over-heating problem on the substrate, which leads to a problem for determining the critical feature size in the structure [42]. Therefore, the SOI-based SOG process is developed in METU to eliminate the over-heating problem on the substrate during the structural layer formation performed using DRIE. In the SOI-based SOG process, first, the glass and SOI wafers are separately processed to form recesses and pad metallization in the glass wafer and the device layer in the SOI wafer, and then these are combined together through the anodic bonding. The use of SOI wafer brings some advantages, such as a uniform etch profile on the structure, higher yield, and lower proof mass voltage required for the gyroscope operation, compared to the classical SOG process. This chapter provides detailed information about the SOI-based SOG process used for fabrication explained in Section 4.1, and fabrication results presented in Section 4.2.

4.1 Fabrication of the Gyroscopes Using SOI-based SOG Process

The SOI-based SOG process is started with an empty Pyrex glass wafer with thickness of 500 μm for forming anchor regions and pad metallization. The first step is the anchor formation, in which the bonding regions required to perform successful bonding of the glass to the silicon are formed on the glass wafer. The anchor formation begins with the roughening of the glass surface using BHF (buffered hydrofluoric acid) that is obtained with lower etch rate compared to pure HF by diluting HF inside NH_4F (ammonium fluoride) within a certain ratio. The roughening of the glass surface is required to have a good adhesion before depositing the masking materials, Cr/Au, onto the glass surface. After roughening, Cr/Au is deposited on a glass wafer with a ratio of 100 A°/1500 A°, respectively, as a masking layer. The Cr/Au is then patterned using wet and selective metal etchants. Next, the glass wafer is put inside pure HF to perform glass etch. The effect of undercut occurred due to the isotropic etching characteristic of HF should be considered when designing the area of the anchor regions. The ratio of the undercut measured after the glass etching is 1:1.3. After completing the anchor formation, the Cr/Au is stripped to prepare the glass wafer for the next step.

The second step is the pad metallization. This step is started with the surface roughening of the glass wafer using BHF, similar with the first step, to ensure the roughness of the glass surface before the deposition of Cr/Au used for the pad metallization that provides electrical connections to the device structure. Then, Cr/Au is deposited onto the surface of the glass wafer with a thickness of 100 A°/1500 A°, respectively. The thickness of the Cr/Au is kept as thin as possible considering the resistance of the metal lines to achieve successful bonding. Next, the metals are patterned using selective chemical metal etchants. Finally, the piranha solution composed of H_2SO_4:H_2O_2 with ratio of 1:1 is applied to the glass wafer prior to the anodic bonding to ensure the cleanness of the glass wafer.

The process is continued with the SOI wafer with a structural layer thickness of 35 μm to form the device layer of the gyroscope. DRIE is used to form the device layer because it provides deep and anisotropic etching. The DRIE etching is performed up to the buried oxide layer of the SOI wafer because it behaves as a passivation layer, but the time of etch period is crucial to prevent the effect of notching occurred due to charge accumulation on the buried oxide layer. The etching using DRIE is based on the successive etching and polymer coating steps. The coated polymer is removed by using piranha solution. Then, BHF is applied to the SOI wafer to remove native oxide grown on the surface of the silicon, which commonly leads to a contact problem in the sensor [39]. Now, the SOI wafer is ready for bonding.

After completing the process of the glass and SOI wafers, these wafers are anodically bonded by using the method proposed in [43]. Then, the handle layer of the SOI wafer is removed by means of DRIE. Again, the buried oxide layer is used as a passivation layer to stop etching. Following, the device layer of the sensors is released by dissolving the buried oxide inside BHF solution. The fabrication of the gyroscopes is finalized with the removal of the buried oxide layer.

The fabrication process is totally composed of three masks, in which two of them, namely anchor formation and pad metallization mask, used for glass process, and the other, called structure mask, is used for the formation of the structural layer of the gyroscope. Figure 4.1 shows the fabrication steps of the gyroscope studied in this thesis.

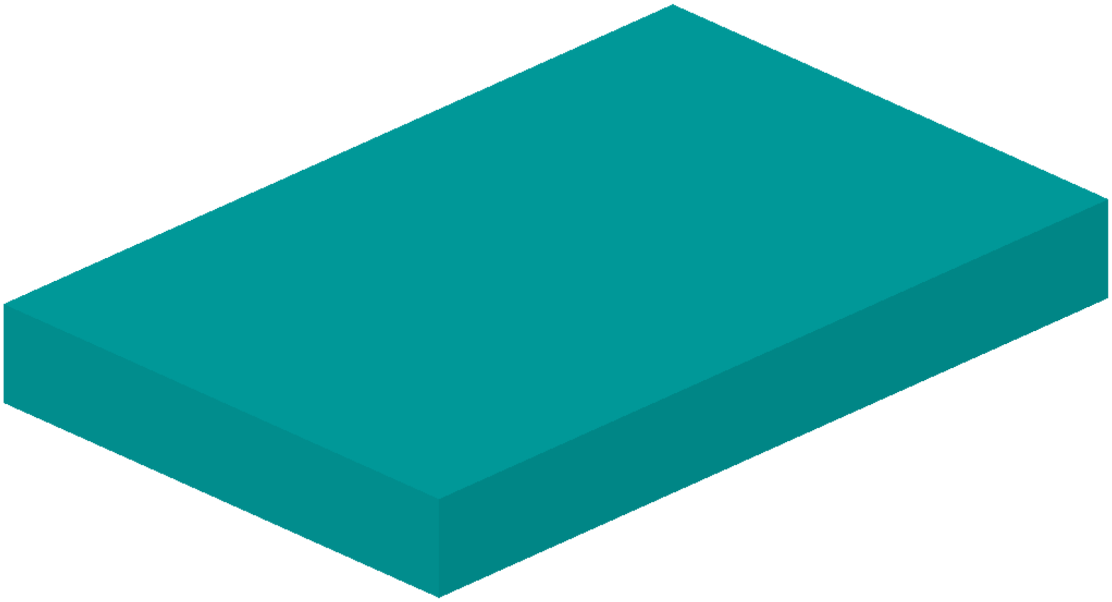

(a) Apply BHF to empty Pyrex glass wafer for roughening of the glass surface

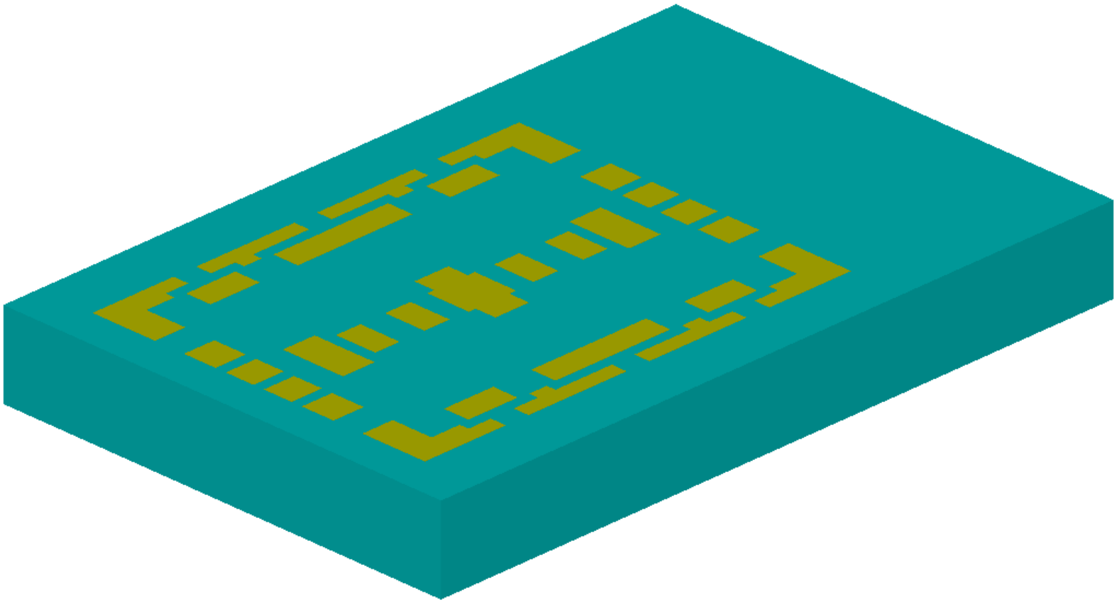

(b) Deposit and pattern Cr/Au using selective metal etchants for anchor formation

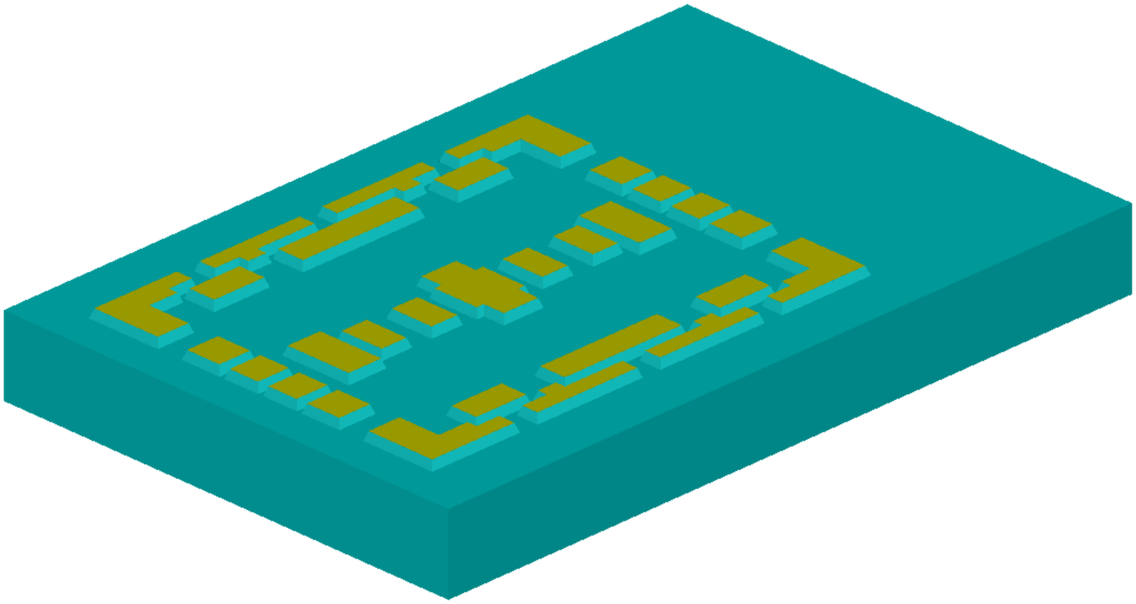

(c) Perform glass etch using HF for anchor formation

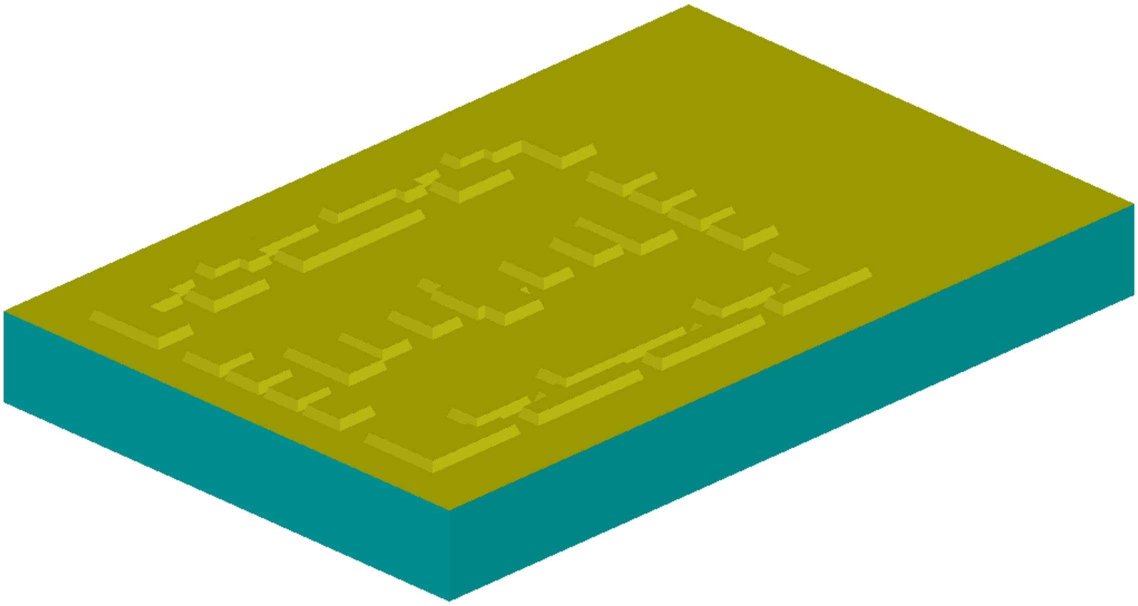

(d) Deposit Cr/Au for pad metallization

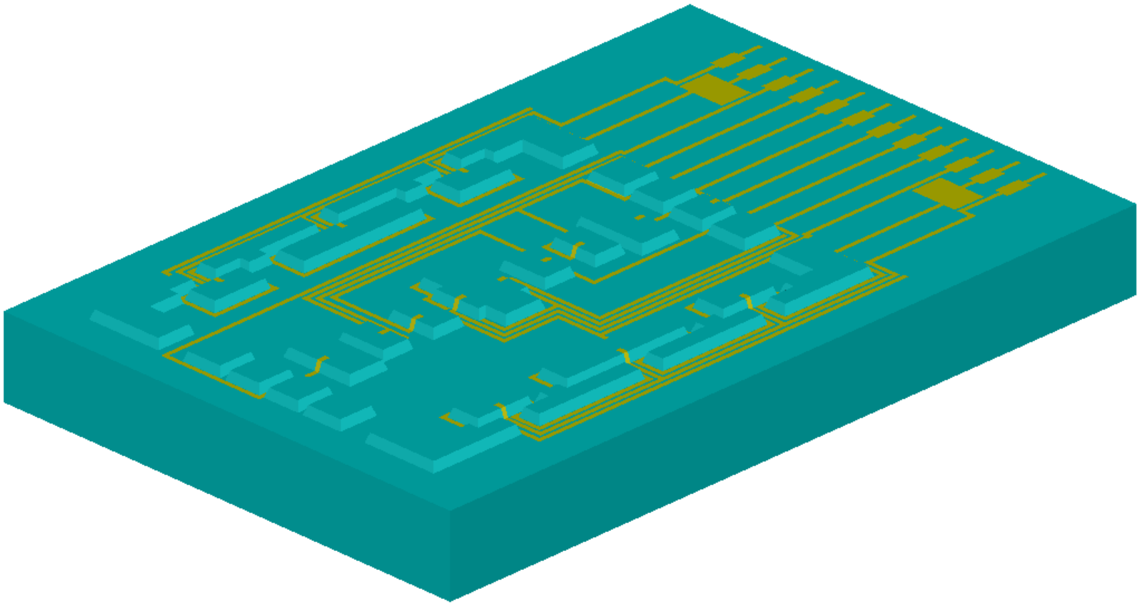

(d) Pattern Cr/Au using selective metal etchants for pad metallization

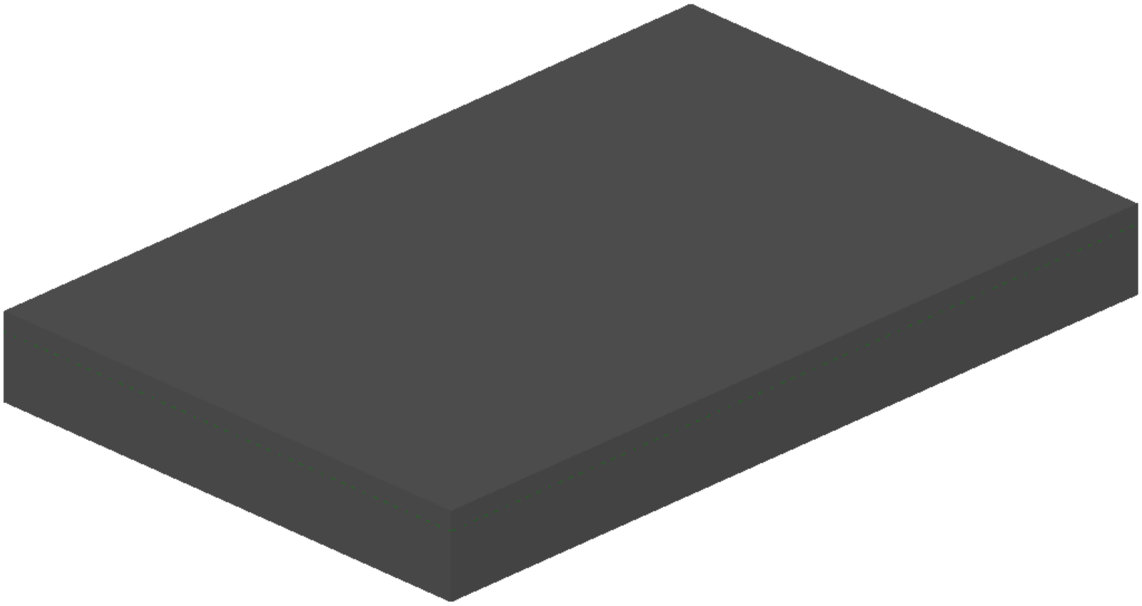

(e) Take SOI wafer for the formation of the device layer

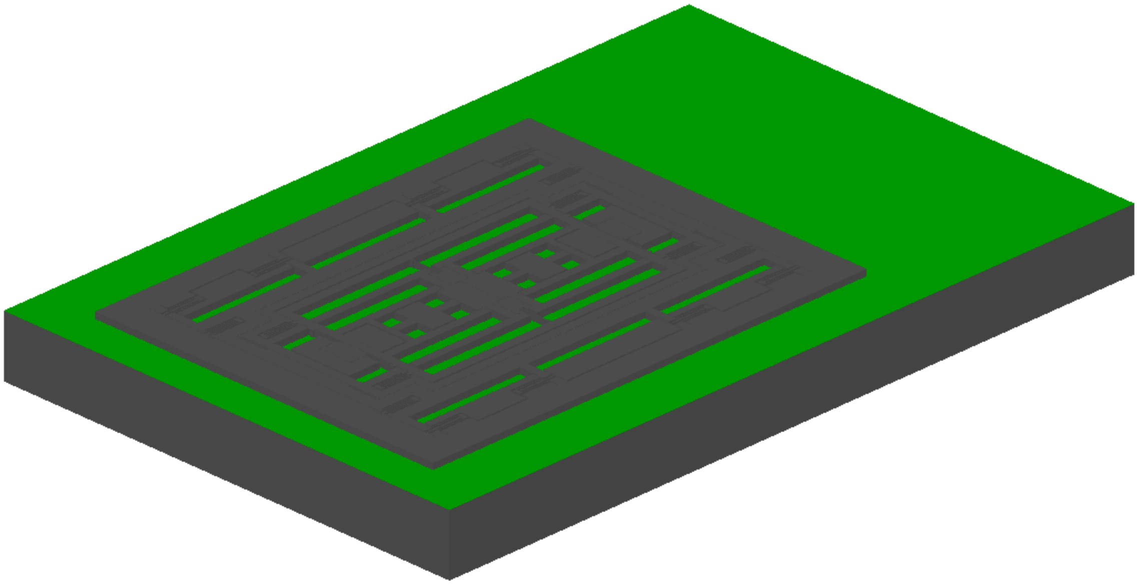

(e) Pattern the device layer using DRIE

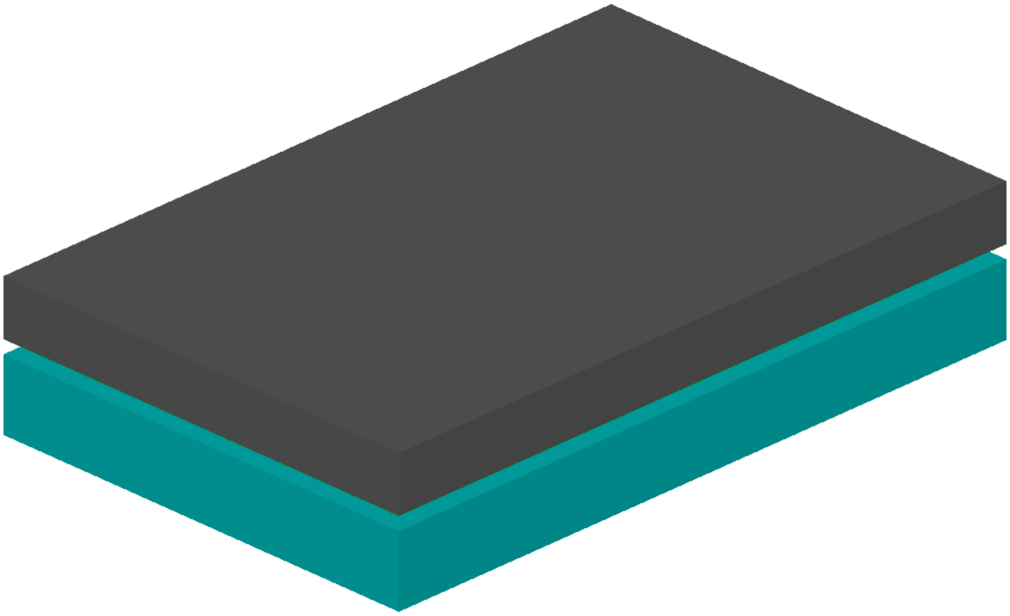

(f) Perform anodic bonding of the glass and SOI wafers

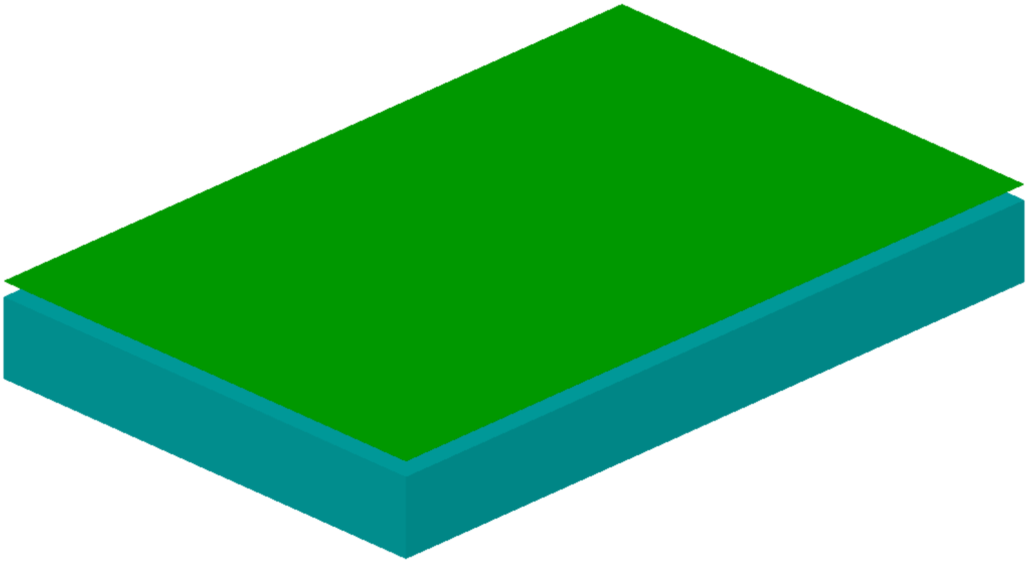

(g) Remove the handle layer of the SOI wafer using DRIE

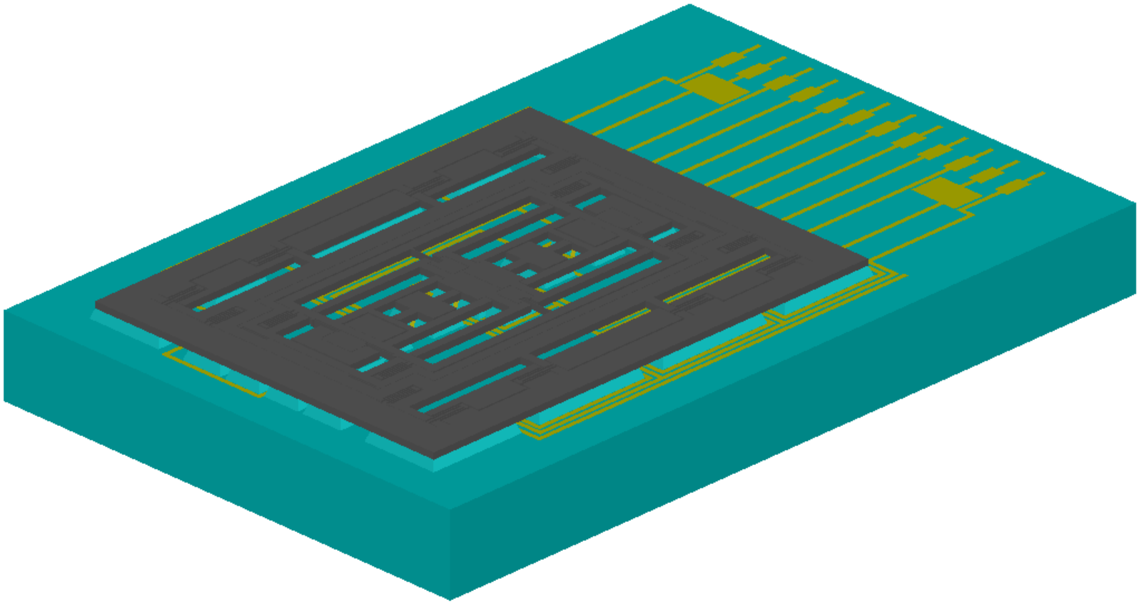

(h) Remove the buried oxide layer through BHF for releasing of the device layer

Figure 4.1: Fabrication steps of the gyroscope studied in this thesis.

4.2 Fabrication Results

All of the fabrications steps are completely optimized during the process of the gyroscope, but it cannot be possible to prevent fabrication imperfections when patterning the device layer of the gyroscope. These fabrication imperfections lead to two main problems, which are notching and critical dimensions loss problems, on the structure of the gyroscope. The effect of notching occurred due to charge accumulation on the buried oxide layer of the SOI wafer is significantly minimized by adjusting the period of the DRIE etch. However, the critical dimension loss cannot be prevented at the formation of the device layer of the gyroscope due to the lithography tolerances and finite lateral etch during DRIE. It is a main obstacle against the mechanical mode-matching because the width of the mode springs are not fabricated as designed, which directly affects the mechanical mode resonance frequencies of the gyroscope. Figure 4.2 shows SEM pictures of double-folded and half-folded springs used in the drive mode, and the clamped-guided-end spring used in the sense mode after the fabrication.

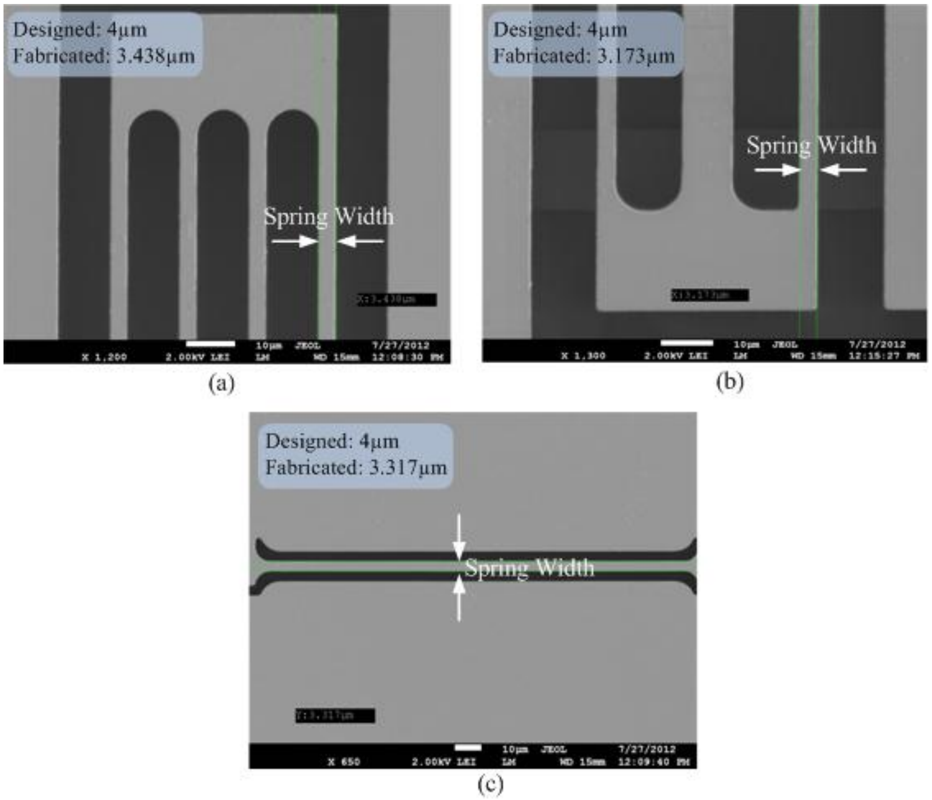

(a) (b)

(c)

Figure 4.2: SEM pictures of (a) double-folded and (b) half-folded springs used in the drive mode, and (c) the clamped-guided-end spring used in the sense mode after fabrication.

Although the width of the drive and sense mode springs are designed to be 4 µm, it becomes narrower after fabrication. The change in the width of the springs causes a shift in the mechanical spring constants of the gyroscope, which leads to a resonance frequency deviation in the resonance modes of the gyroscope.

In this study, the gap dimensions between the sense, quadrature, and frequency tuning electrodes except the drive electrodes are also so critical for the mode-matched gyroscope operation to get better performance, higher quadrature suppression effect within a certain potential range, and higher frequency tuning capability within a certain potential range. Since the drive electrodes consist of the varying overlap area type capacitors, the capacitive sensitivity in the drive mode is not substantially affected from the change at the gap of the drive electrodes because it is directly proportional with the inverse of the gap dimension, ${D_0}^{-1}$. However, the capacitive sensitivity of the sense, quadrature, and frequency tuning electrodes are directly proportional with the inverse square of the gap dimension, ${D_0}^{-2}$. Figure 4.3 shows the SEM pictures of the sense, quadrature, and frequency tuning electrodes after fabrication.

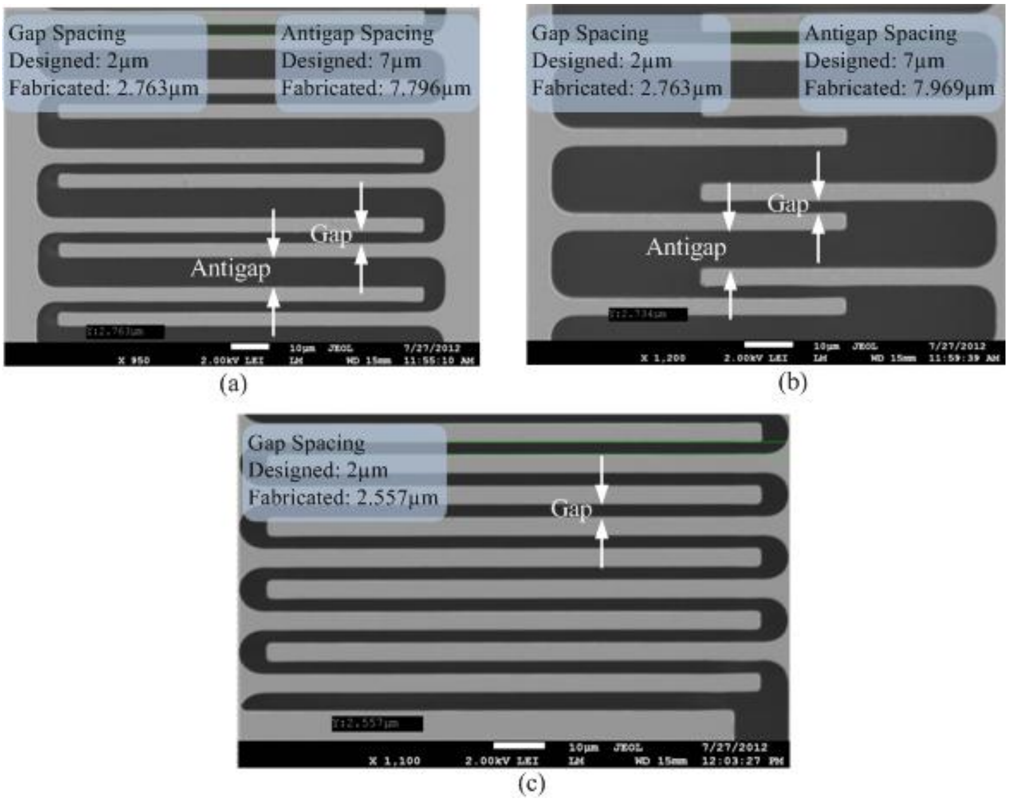

Figure 4.3: SEM pictures of (a) the sense, (b) quadrature, and (c) frequency tuning electrodes after fabrication.

Although the gaps and antigaps between capacitive plates are designed to be 2 and 7 μm in the gyroscope, respectively, they are obtained wider after fabrication as expected.

Ideally, the mode frequencies of the gyroscope are designed to be nearly matched considering the electrostatic spring effect for the proof mass potential of 10V. However, the change in capacitive gap dimension and width of the springs causes a non-uniform shift in the resonance mode frequencies of the gyroscope. Table 4.1 shows the comparison of designed and measured spring constants and resonance frequencies for the resonance modes of the gyroscope. The comparison in Table 4.1 proves that the designed parameters are consistent with the measured parameters when the change in the capacitive gap dimensions and width of the springs are taken into account.

Table 4.1: Comparison of designed and measured spring constants and resonance frequencies for the modes of the gyroscopes. (Design and measurement are made for 10V proof mass potential).

Parameter	**Designed**		**Measured (Average)**	
	Drive Mode	**Sense Mode**	**Drive Mode**	**Sense Mode**
Effective Spring Constant, N/m	923	724	661	528
Resonance Frequency, Hz	15108	15105	12787	12890

Figure 4.4 shows SEM pictures of the fabricated single-mass fully-coupled gyroscope and zoomed views of the frequency tuning electrodes used to electrostatically tune the sense mode resonance frequency for the mode-matching.

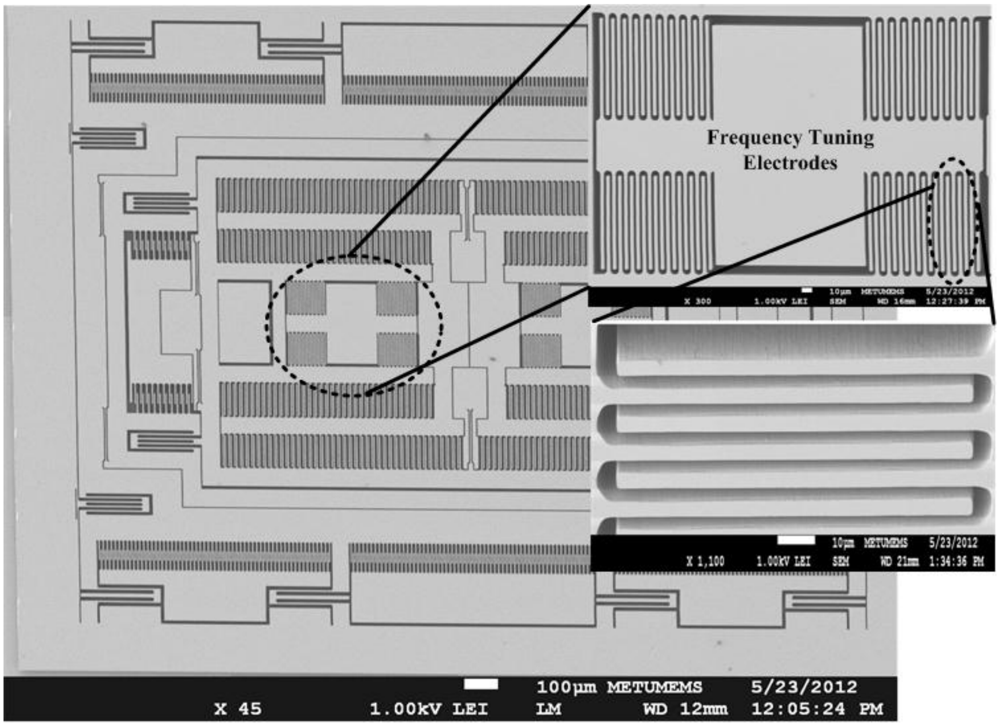

Figure 4.4: SEM pictures of the fabricated single-mass fully-coupled gyroscope and zoomed views of the frequency tuning electrodes used to electrostatically tune the sense mode resonance frequency for the mode-matching.

4.3 Summary

This chapter first provides information about the fabrication of the studied gyroscope with detailed process steps. Second, fabrication imperfections occurred on the device layer of the gyroscope during DRIE etch are briefly discussed. Finally, the comparison of the designed and measured parameters for the fabricated single-mass fully-decoupled gyroscope is presented.

CHAPTER 5

TEST RESULTS

This chapter presents the test results of the studied MEMS gyroscopes. Section 5.1 explains the resonance characterization and test procedure for studied gyroscopes, and Section 5.2 describes the system level test setup and method for the studied gyroscopes. Next, the tests results of the studied gyroscope for the mode-matched and mismatch gyroscope operations are provided in Section 5.3. Section 5.4 demonstrates performance test results of the studied gyroscopes under different temperature and vacuum conditions. Following, Section 5.5 presents the experimental system bandwidth verification. Finally, Section 5.6 gives a summary of this chapter.

5.1 Resonance Characterization and Test Procedure for MEMS Gyroscopes

After completing the fabrication of MEMS gyroscopes, wafer level resonance tests are first performed by randomly choosing the gyroscopes from the wafer to decide whether the sensor wafer is worth dicing or not. If the drive and sense modes of the gyroscopes are properly working as a result of wafer level resonance tests, the gyroscopes are separated to dies by dicing. Then, die level resonance tests are performed to observe whether the gyroscopes are functional or not after dicing because the gyroscopes can damage during dicing. The die level resonance tests are performed under the atmospheric pressure condition. Figure 5.1 shows the test setup that is used extract the drive and sense mode resonance characteristics of the gyroscopes. As seen in Figure 5.1, the special probes are used to build an electrical connection between the gyroscope and measurement devices. In the resonance tests, an AC signal whose frequency can be swept in the desired range is provided to the gyroscope using a dynamic signal analyzer.

The AC signal results in a current at the output of the gyroscope creating an excitation. The resultant current is fed to the dynamic signal analyzer after converting it to voltage through the preamplifier. Taking a ratio between the output and input of the gyroscope in the frequency domain, the resonance characteristics of the gyroscope is extracted by the dynamic signal analyzer. The gain, resonance frequency, and quality factor of the gyroscope for both drive and sense modes are directly obtained through the resonance test. As a result of die level resonance tests performed under the condition of atmospheric pressure, some gyroscopes having the desired resonance frequency and gain are chosen.

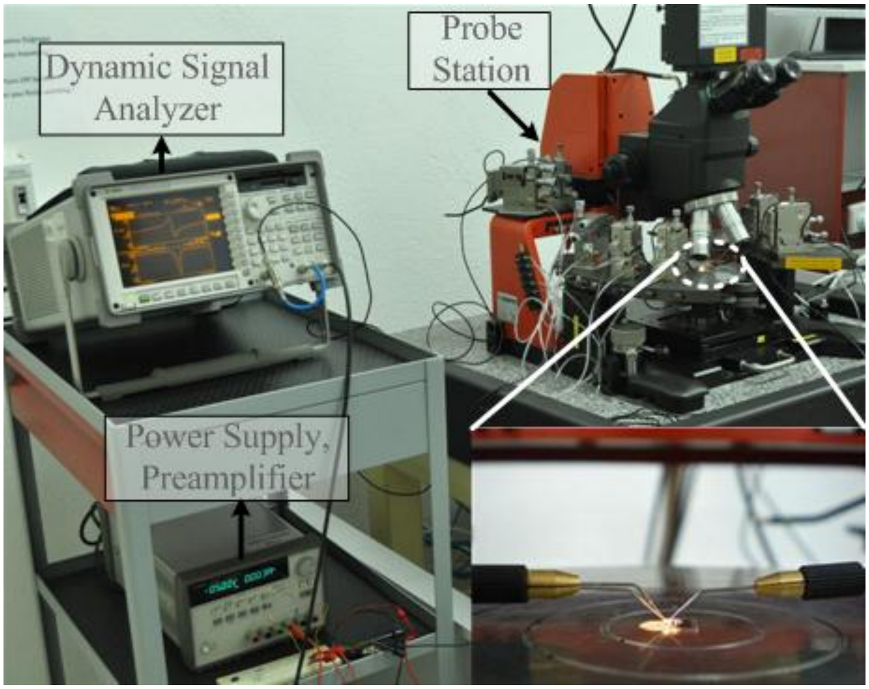

Figure 5.1: Test setup for die level resonance tests.

After die level resonance tests, the gyroscope is integrated with the front-end electronics using a special hybrid glass substrate and package that enables to operate the gyroscope under the vacuum condition. Figure 5.2 shows a gyroscope integrated with the front-end electronics using the hybrid glass substrate and package. The electrical connection between the front-end electronics and gyroscope is accomplished by wire-bonding which leads to a parasitic capacitance. The parasitic capacitance adversely affects the noise performance of the system, shown in Equation 3.33. Therefore, the length of the wire bonding should be kept as small as possible to reduce the amount of the parasitic capacitance. It should be also noted that the hybrid glass substrate is specially designed to keep the stray capacitance between the resonance modes of the gyroscope as small as possible in order to prevent a phase error during mode-matching. After combining the gyroscope and front-end electronics the resonance test is repeated to check whether the gyroscope with the front-end electronics is properly working or not. Next, the hybrid package is vacuumed using a method, called projection welder. Vacuum packaging is necessary to reduce the damping factor during the gyroscope operation.

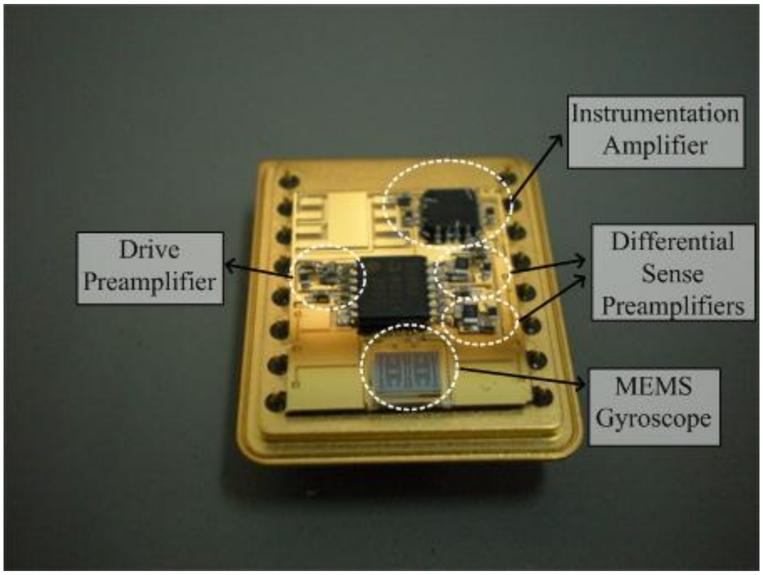

Figure 5.2: View of the gyroscope integrated with the front-end electronics using the hybrid glass substrate and package.

After vacuum packaging, the resonance test is again performed to extract the model parameters of the gyroscope, which are the drive and sense mode capacitive sensitivities, quality factors, resonance frequencies, and gains, required to obtain a complete model of the gyroscope. The complete model of the gyroscope is used in the controller design, discussed in Chapter 3. Table 5.1 and 5.2 shows the drive and sense mode resonance characteristics of the vacuum packaged gyroscopes studied in this thesis, respectively. The resonance tests are performed with an applied tuning potential of 0 V to the frequency tuning electrodes for the gyroscopes of C05, D12, and F09, which are the designed and fabricated single-mass fully decoupled gyroscope, shown in Figure 1.4. However, the gyroscopes of J01 and J02 are the modified fully-decoupled gyroscopes, shown in Figure 1.3.

Table 5.1: Drive mode resonance characteristics of the vacuum packaged gyroscopes studied in this thesis.

Gyro ID	Proof Mass (V)	Res Freq. (Hz)	Res. Gain (dB)	Quality Factor
J01	10	13906	19.7	42224
J02	10	14184	21.3	49776
C05	9.5	11805	0.8	22702
D12	9.5	12498	3.2	31457
F09	9.5	12307	0.5	22792

Table 5.2: Sense mode resonance characteristics of the vacuum packaged gyroscopes studied in this thesis.

Gyro ID	Proof Mass (V)	Res Freq. (Hz)	Res. Gain (dB)	Quality Factor	Δf (Hz)
J01	10	13821	31.2	2442	85
J02	10	14013	34.8	2922	171
C05	9.5	11733	25	1350	72
D12	9.5	12429	28.4	1851	69
F09	9.5	12270	24.5	1227	37

At the design stage of the gyroscope, the resonance mode frequencies of the gyroscope are adjusted to be nearly matched considering the electrostatic spring effect, but the fabrication imperfections lead to a frequency split between the resonance modes. In

Table 5.2, Δf represents the frequency split between the resonance modes of the gyroscope for the given proof mass potentials.

In the scope of this thesis, mode-matching is successfully performed using two methods described in Section 3.5. In the first method, the mode-matching is accomplished tuning the sense mode resonance frequency with respect to the drive mode resonance frequency changing the proof mass potential (V_{PM}) in a range of only ±2.5 V. The range of changing V_{PM} directly indicates the amount of the maximum allowable initial frequency split between the modes. Figure 5.3 shows the drive and sense mode resonance frequency characteristics of the gyroscope (J02) on the condition of changing proof mass potential in a range of ±2.5 V. The drive mode resonance frequency of the gyroscope remains constant at 14184 Hz, whereas the sense mode frequency of the gyroscope can be electronically tuned through the sense electrodes in the range of 14355 Hz to 13324 Hz by changing V_{PM} from 8 V to 13 V. The resonance mode frequencies are perfectly matched at the proof mass potential of 9.33 V.

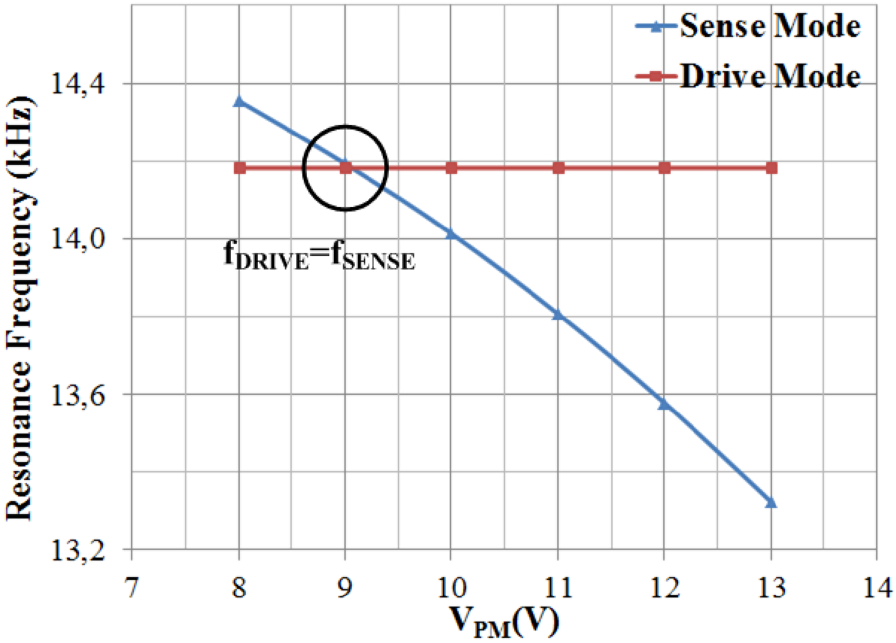

Figure 5.3: Drive and sense mode resonance frequency characteristics of the studied gyroscope (J02) with changing proof mass potential.

In the second method, mode-matching is achieved only changing the tuning potential applied to the frequency tuning electrodes (FTEs) in a range of ±2.5 V. Figure 5.4 shows the frequency characteristics of the resonance modes of the gyroscope (C05) on the condition of changing the tuning potential (V_{FTE}) in a range of ±2.5 V. The drive mode resonance frequency of the gyroscope does not vary with changing V_{FTE}, whereas the sense mode frequency of the gyroscope can be electronically tuned in the range of 11875 Hz to 11543 Hz by changing V_{FTE} from -2.5 V to 2.5 V. The resonance mode frequencies are perfectly matched at the tuning potential of 1.24 V with the proof mass potential of 9.5 V.

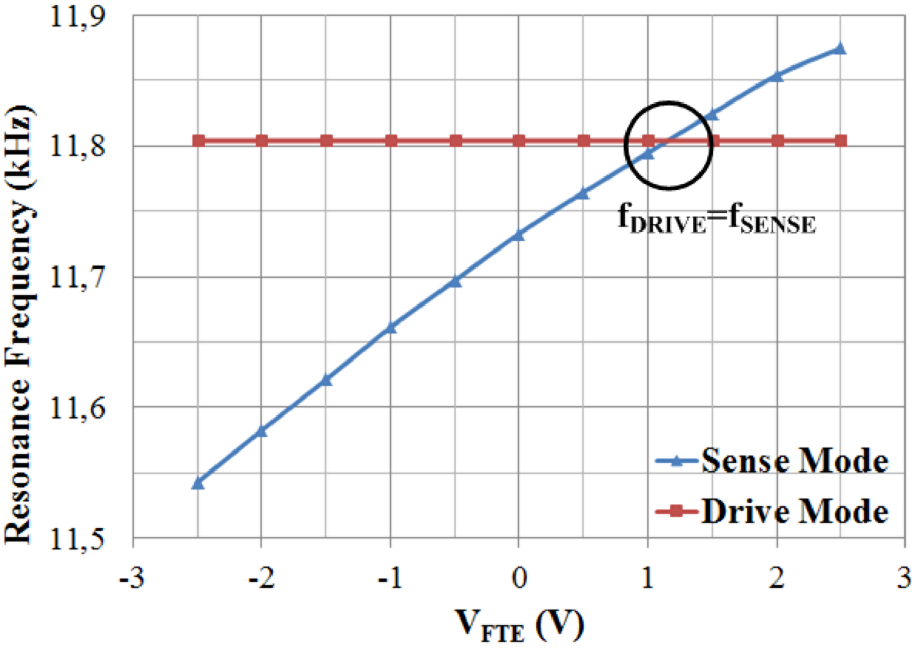

Figure 5.4: Drive and sense mode resonance frequency characteristics of the studied gyroscope (C05) with changing the tuning potential applied to the frequency tuning electrodes.

5.2 System Level Test Setup and Method for Studied MEMS Gyroscopes

After vacuum packaging of the gyroscope, system level tests are performed to get information about the performance of the gyroscope. In order to perform system level tests, the vacuum packaged gyroscope is first integrated with the drive, sense, quadrature cancellation, and mode-matching controller loops on a PCB. The controller loops are implemented in hybrid packages for low-noise measurements. Second, the PCB is mounted in a test setup, illustrated in Figure 5.5, to perform system level tests.

System level tests consist of scale factor and noise tests. Scale factor tests are first performed using a computer controlled Ideal Aerosmith single-axis rate table, shown in Figure 5.5, which generates an angular rotation rate at various magnitudes and frequencies. In the scale factor test, the rate signal is applied to the system in a range of ±100 °/sec. During the scale factor tests the applied angular rotation rate is first increased from 0°/sec to 100 °/sec, and then decreased from 100 °/sec to -100 °/sec, and finally it is increased from -100 °/sec to 0°/sec with a step of 10 °/sec. At the same time the output response of the gyroscope is recorded through a data acquisition (DAQ) card placed in a computer. The triangular applied rate provides an opportunity to observe the hysteresis and linearity. Finally, the linearity, dynamic range, and response of the gyroscope to the angular rate rotation are extracted from data obtained during the scale factor test. Second, the stationary gyroscope data is taken through the DAQ card for the noise measurements. The obtained data provides an opportunity to extract the amount of noise density at the rate output of the gyroscope for different integration times. The rate-equivalent input noise density is then obtained by dividing the rate output noise density to the scale factor via “AlaVar 5.2” Allan variance processing software.

The Allan Variance technique, time-domain analysis of the uncertainty at the gyroscope output, is used to determine the performance parameters of the gyroscope, namely angle random walk (ARW) that gives the input referred rate-equivalent white noise density and bias instability which indicates the amount of the minimum detectable angular rotation rate. Figure 5.6 shows a typical Allan Variance graph. The bottom axis shows averaging time, and the vertical axis shows the Allan deviation at the gyroscope output. The cross section point of the slope of -0.5 and averaging time of 1 is the ARW performance of the gyroscope, and the point, where the slope is equal to zero, shows the bias instability performance of the gyroscope.

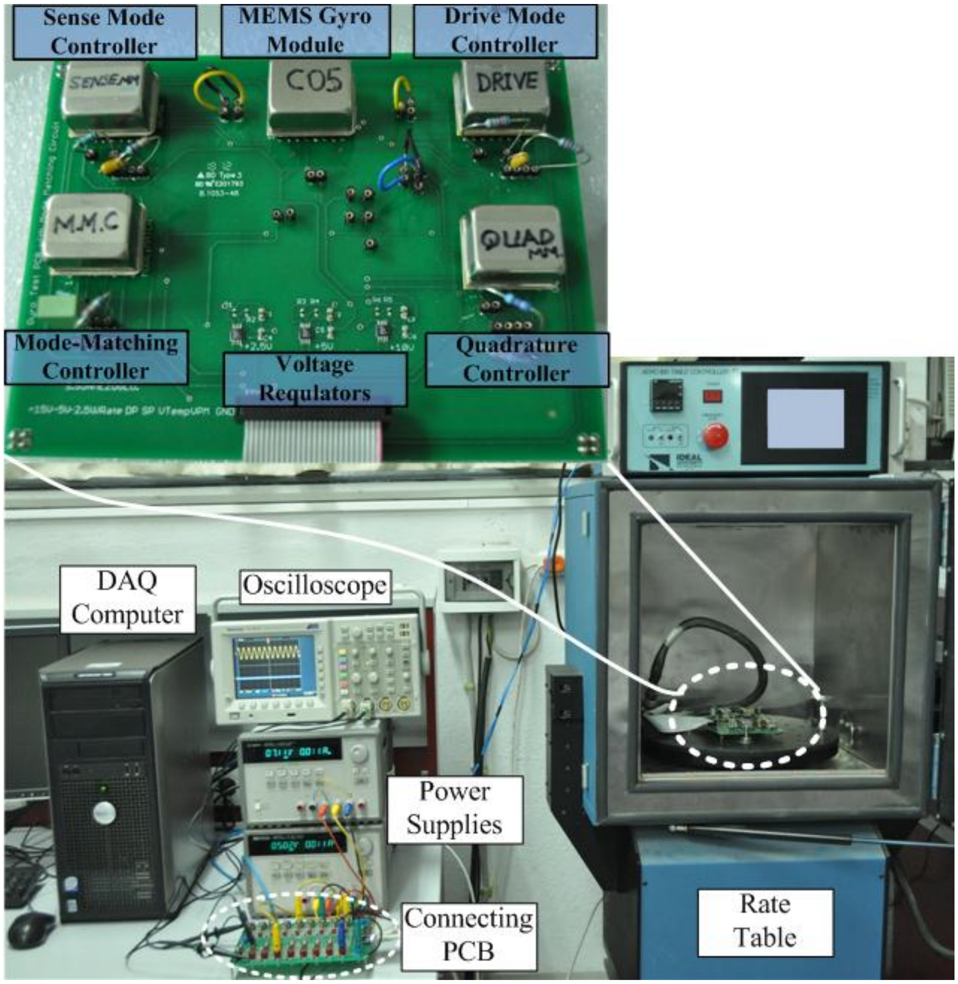

Figure 5.5: Test setup for system level tests.

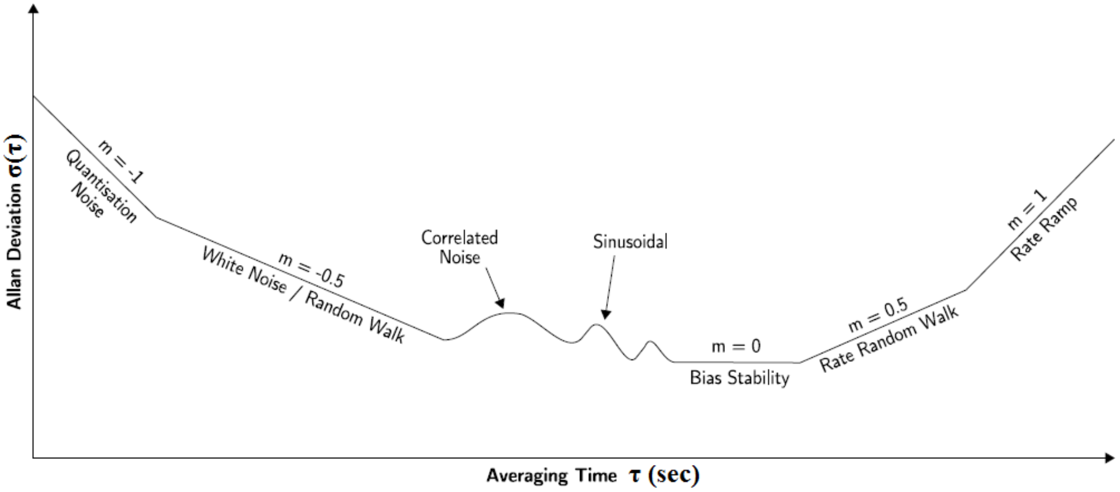

Figure 5.6: A typical Allan Variance graph [51].

5.3 Test Results of Studied MEMS Gyroscopes for Mode-Matched and Mismatch Conditions

During the gyroscope tests, the first step is to monitor the drive pick signal that is the measure of the drive mode displacement. The performance parameters of the gyroscope, such as ARW, bias instability, linearity, and dynamic range, are directly affected in the presence of instability at the drive mode displacement that leads to a change in the scale factor and mechanical Brownian noise. Therefore, the drive mode displacement should be kept constant throughout the life of the gyroscope operation to ensure stable gyroscope operation. In this study, the drive mode displacement is adjusted to be 4 and 4.5 μm for the specified proof mass potentials. Figure 5.7 shows the steady-state drive motor and drive pick signals for the proposed closed loop drive mode controller. The drive pick and motor signals is in-phase due to the resistive preamplifier used in the drive mode controller. The peak-to-peak amplitude of the drive pick signal corresponds to the drive displacement of 4.5μm. The amount of the drive mode displacement can also be adjusted by changing the gain of the low pass filter in the drive mode controller.

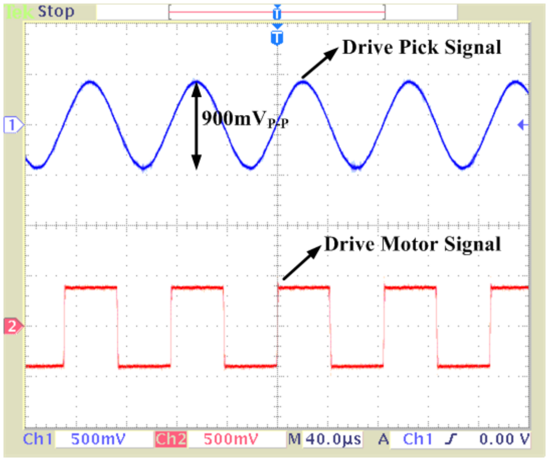

Figure 5.7: Steady-state drive motor and pick signals for the proposed closed loop drive mode controller.

Second step of the tests is to monitor the sense pick signal that directly provides an opportunity to observe the quadrate signal at the rate output of the gyroscope under the zero-rate condition. Figure 5.8 shows the sense and drive pick signals (a) under the high frequency mismatch condition (>100 Hz), (b) the low frequency mismatch condition (<100 Hz), and (c) the mode-matched condition. At the start-up of the mode-matching system, first, there is an initial frequency split between the resonance modes of the gyroscopes, called frequency mismatch, exists, shown in Table 5.2. The frequency mismatch condition leads to a significant amount of the quadrature signal at the sense mode output of the gyroscope due to the phase inconsistency at the system. At mismatched gyroscope operation, there is phase difference of 90° between the quadrature and drive signals, shown in Figure 5.8-a. When the frequency mismatch amount between the resonance modes decreases thanks to the mode-matching controller loop that provides tuning of the sense mode resonance frequency with respect to drive mode resonance frequency the quadrature signal amplifies due to the sensitivity improvement at the gyroscope. The amplified quadrature signal saturates the rate output of the sense mode controller, shown in Figure 5.8-b. After the mode-matching system reaches to the steady-state condition, the quadrature signal substantially minimized through the quadrature cancellation controller within a short period of time, around 16 msec. The minimized quadrature signal, shown in Figure 5.8-c, ensures the functionality of our mode-matching system because if the quadrature controller does not work properly, the quadrature signal would not be cancelled since the phase relationship in the system will be inconsistent for proper operation. Additionally, when the resonance modes of the gyroscope are perfectly matched, there will be no phase difference exists between the residual quadrature and drive signals.

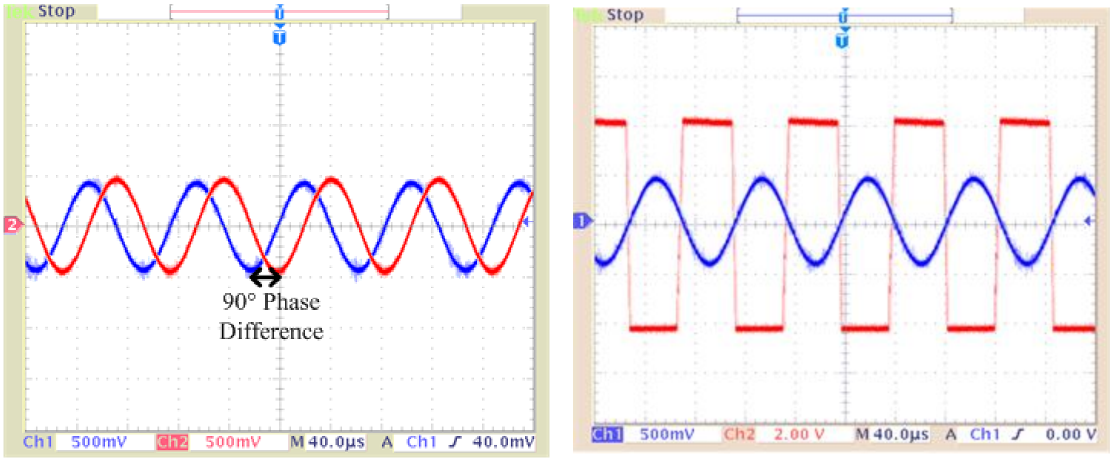

(a) (b)

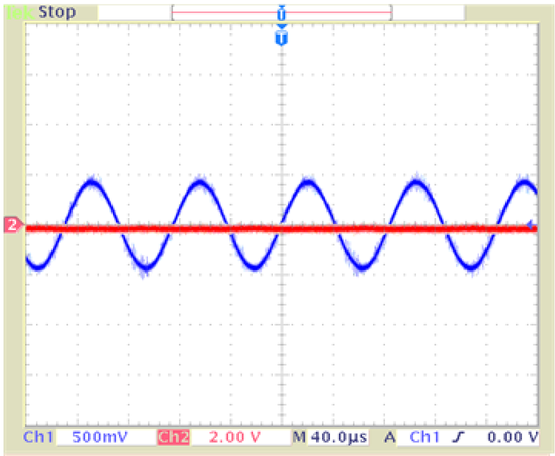

(c)

Figure 5.8: Sense (red line) and drive (blue line) pick signals (a) under the high frequency mismatch condition (>100 Hz), (b) the low frequency mismatch condition (<100 Hz), and (c) the mode-matched condition.

The transient behavior of the mode-matching controller is also investigated in the tests to verify the simulation results, shown in Figure 3.29, with experiments. Figure 5.9 shows the measured tuning potential of the gyroscope (C05) for a frequency split of (a) 69 Hz and (b) 100 Hz during the mode-matching. The experiments demonstrate that the transient response of the mode-matching system depends on the initial frequency split between the resonance modes. The mode-matching system settles within 1.6 sec for a frequency split of 69 Hz and 2.1 sec for a frequency split of 100 Hz. This verifies that the measured and simulated data are approximately consistent with each other. The only difference between the simulation and experiment is the required tuning potential of the gyroscope (C05) for mode-matching. This difference results from the fabrication imperfections during the device layer formation. Normally, the gap spacing, D_0, across the capacitor plates of the frequency tuning electrodes, used in simulations, is designed to be 2 μm, but it is wider after the fabrication, shown in Figure 4.3. Since the electrostatic spring constant is inversely proportional with D_0^3, its effect on the sense mode resonance frequency substantially decreases. Therefore, in order to achieve mode-matching for the same frequency split between the resonance modes, the required tuning potential is higher in experiments compared to simulations. This concludes that the measured transient response of the mode-matching system approximately matches with the simulation results.

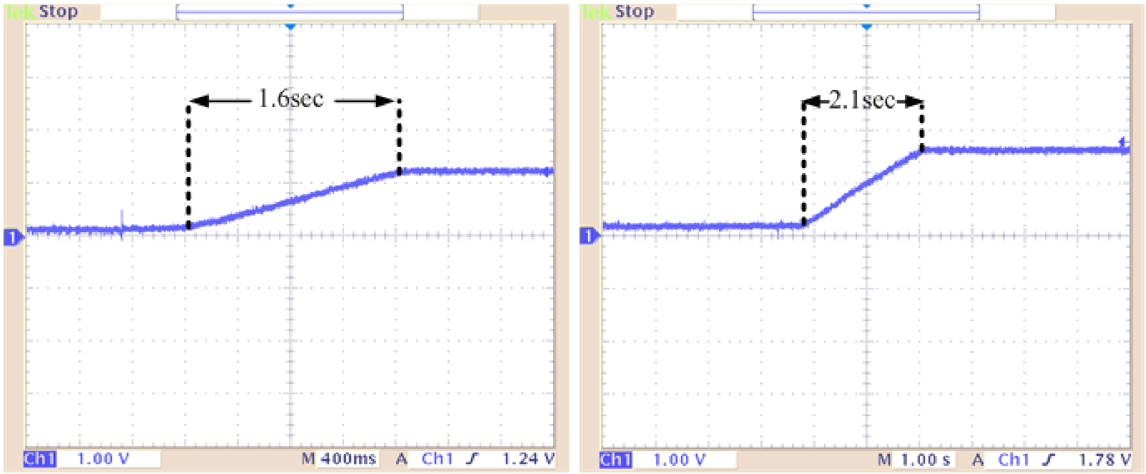

(a) (b)

Figure 5.9: Measured tuning potential of the gyroscope (C05) for a frequency split of (a) 69 Hz and (b) 100 Hz during the mode-matching.

Then, Allan Variance tests are performed under the mode-matched and mismatched conditions to observe the effect of mode-matching on the performance of the gyroscope. First, the tests are performed for the first mode-matching implementation in which the resonance modes of the gyroscope are operated to be perfectly matched by means of the changing proof mass potential. Before Allan Variance tests, the scale factors of the modified fully-decoupled gyroscopes are measured at different proof mass potentials (V_{PM}) and same drive displacements for the mode-matched and mismatched (~100 Hz) conditions, shown in Table 5.3. The scale factors of the gyroscope are not the same both mode-matched and mismatched conditions due to the variation of the proof mass potentials as expected. It should be also noted that the scale factor is obtained after multiplying the rate output of the gyroscope with a gain of 10.

Table 5.3: Scale factor measurement results of the modified fully-decoupled gyroscopes for the mode-matched and ~100 Hz mismatched conditions.

Gyro ID	**Drive Disp. (μm)**	**Mismatch (~100 Hz)**		**Mode-Matched**	
		V_{PM} (V)	**Scale Factor (mV ^{0}/sec)**	**V_{PM} (V)**	**Scale Factor (mV ^{0}/sec)**
J01	4	10.15	11.8	9.55	14
J02	4	9.81	12.9	9.33	15.4

In this study, the Allan Variance test results will be reported for the tested gyroscopes, but the Alan Variance plot is not provided for all of them instead the procedure is explained to clarify how the ARW and bias instability performance of the gyroscopes are obtained. Only best performance results are given as an Allan Variance graph. In Allan Variance tests, the zero-rate output (ZRO) of the studied gyroscopes was recorded by using the data acquisition card with a sampling frequency of 5 kHz for a period greater than 1hr. Then, the recorded data is processed in "AlaVar 5.2" Allan Variance processing software using the scale factors of the gyroscopes. Figure 5.10 shows a sample Allan Variance graph for the gyroscope (JO1) under the mode-matched condition. ARW value corresponds to the intersection point of the fitted line with a slope of -1/2 and averaging time, τ, of 1sec, and bias instability is found by fitting a line to the point where the slope is equal to zero. Using Figure 5.10, the ARW and bias instability value of the gyroscope (J01) under the mode-matched condition is found as 2.18 °/hr and 1.6 °/hr, respectively. However, in the literature generally the unit of ARW is expressed by °/√hr. Therefore, in this study the ARW values are also expressed in terms of °/√hr that is obtained by dividing the unit of °/hr to 60. Furthermore, in the Allan Variance graph, the trend of the noise level decreases as τ decreases because of the low-pass filer characteristics used in the closed loop sense mode controller. The τ, smaller than 0.01 sec, corresponds to the high frequency noises that is rejected by the low-pass filer having a cut-off frequency of 100Hz. Therefore, this portion of the graph up to 0.01 sec of τ should not be considered during the noise analysis of the mode matching system.

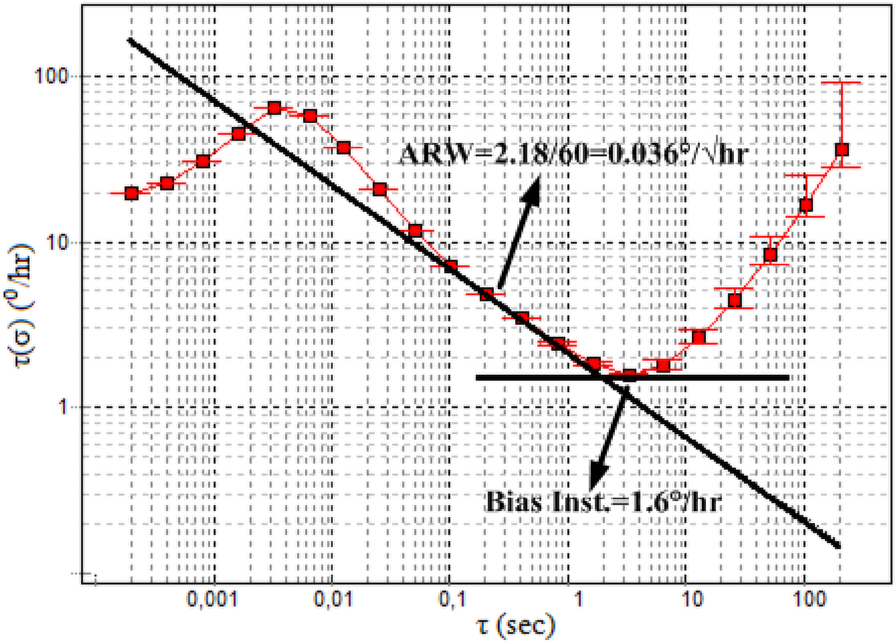

Figure 5.10: Sample Allan Variance graph for the gyroscope (JO1) under the mode-matched condition.

Table 5.4 shows the ARW and bias instability performances of the modified fully-decoupled gyroscopes under the mode-matched and mismatched (~100 Hz) conditions for the given proof mass potentials, provided in Table 5.3. The frequency split of 100 Hz between resonance modes is chosen for the mismatch gyroscope operation because it is the point where the highest performance is obtained. Test results demonstrate that the ARW and bias instability performances of the gyroscopes significantly improve up to 1.7 and 2.4 times, respectively, under the mode-matched condition compared to the mismatched (~100 Hz) condition. On the condition of the mode-matched gyroscope operation, the performance improvement is achieved through the substantial suppression of the electronic noise of the sense mode controller. At the mode-matched gyroscope operation, the ARW performance of the gyroscope is quite close to the estimated mechanical Brownian noise limit of the gyroscope.

Table 5.4: ARW and bias instability performances of the modified fully-decoupled gyroscopes under the mode-matched and mismatched (~100 Hz) conditions.

Gyro ID	Drive Disp. (µm)	Mismatch (~100 Hz)		Mode-Matched	
		ARW (°/√hr)	Bias Inst. (°/hr)	ARW (°/√hr)	Bias Inst. (°/hr)
J01	4	0.043	2.6	0.036	1.6
J02	4	0.044	2	0.026	0.83

Figure 5.11 shows the Allan Variance graphs of the gyroscope (J02) under the mode-matched and mismatched (~100 Hz) conditions. The ARW and bias instability performances of the gyroscope reach to 0.026 °/√hr and 0.83 °/hr, respectively, close to the theoretically-calculated mechanical Brownian noise limit of 0.018 °/√hr for the gyroscope, with mode-matching.

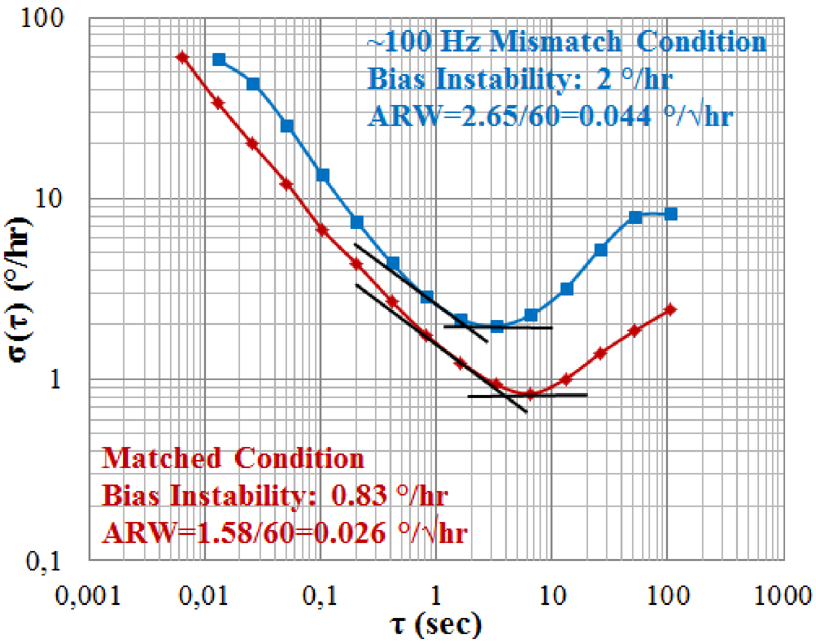

Figure 5.11: Allan Variance graphs of the gyroscope (J02) under the mode-matched and mismatched (~100 Hz) conditions, close to the theoretically-calculated mechanical Brownian noise limit of 0.018 °/√hr, with mode-matching.

Second, the Allan Variance tests are performed for the second mode-matching implementation in which mode-matching is achieved using the frequency tuning electrodes that provides a capability of tuning the sense mode resonance frequency with respect to the drive mode resonance frequency, independently from the proof mass potential. This study mainly focuses on the second mode-matching implementation because a change in the proof mass potential is not desired during the gyroscope operation since it directly affects the overall system dynamics of the gyroscope, discussed in Section 3.5. Before Allan Variance tests, the scale factors of the single-mass fully-decoupled gyroscopes are measured for the same proof mass potentials (V_{PM}) and drive displacements for the mode-matched and mismatched (~200 Hz) conditions, shown in Table 5.5. The scale factors of the gyroscopes are same for both mode-matched and mismatched (~200 Hz) conditions thanks to the frequency tuning electrodes because the proof mass potential and the drive displacement is kept constant during the gyroscope operation. The frequency split between the resonance modes of the gyroscope is directly adjusted applying a DC potential, called V_{FTE}, to the frequency tuning electrodes.

Table 5.5: Scale factor measurement results of the single-mass fully-decoupled gyroscopes under the mode-matched and mismatched (~200 Hz) conditions. (Tabulated V_{FTE} values are used to achieve ~200 Hz mismatched condition.)

Gyro ID	**Drive Disp. (µm)**	**V_{PM} (V)**	**V_{FTE} (V)**	**Scale Factor (mV °/sec)**
C05	4.5	9.5	4.34	24.3
D12	4.5	9.5	4.29	20.5
F09	4.5	9.5	3.78	21.2

Table 5.6 shows the ARW and bias instability performances of the single-mass fully-decoupled gyroscopes under the mode-matched and mismatched (~200 Hz) conditions for the proof mass potential of 9.5 V. The amount of mismatch is chosen to be 200 Hz for the gyroscope operation to obviously see the effect of mode-matching on the

performance of the gyroscope because as the frequency split between the resonance modes increases, the performance of the gyroscope decreases due to the sensitivity reduction of the sensor. Test results demonstrate a substantial performance enhancement up to 2.6 times in bias instability and 2 times in ARW with mode-matching. Furthermore, as seen in Table 5.6 and Table 3.8, the measured and calculated ARW performances of the gyroscope (C05) are approximately consistent with each other for the mode-matched and mismatched (~200 Hz) gyroscope operations. The ARW value of the gyroscope (C05) is approximately matches the theoretically-calculated mechanical Brownian noise limit (~0.029 °/√hr) under the mode-matched condition. This obviously verifies and indicates that the electronic noise of the sense mode controller is almost totally suppressed with mode-matching.

Table 5.6: ARW and bias instability performances of the single-mass fully-decoupled gyroscopes under the mode-matched and mismatched (~200 Hz) conditions.

Gyro ID	**Drive Disp. (µm)**	**Mismatch (~200Hz)**		**Mode-Matched**	
		ARW (°/√hr)	**Bias Inst. (°/hr)**	**ARW (°/√hr)**	**Bias Inst. (°/hr)**
C05	4.5	0.042	2.6	0.029	1
D12	4.5	0.049	1.8	0.024	0.73
F09	4.5	0.061	1.8	0.031	1.3

Figure 5.12 shows the Allan Variance graphs of the gyroscope (D12) under the mode-matched and mismatched (~200 Hz) conditions. The gyroscope demonstrates a performance of 0.024°/√hr in ARW and 0.73°/hr in bias instability, close to the estimated mechanical Brownian noise limit of 0.023°/√hr for the tested gyroscope, with mode-matching. The gyroscope (D12) shows better performance among other single-mass fully-coupled gyroscopes (C05 and F09) thanks to the sense mode quality factor that is higher than the others. An increase in the sense mode quality factor provides an improvement in the mechanical Brownian noise of the sensor. Since the performance of

the gyroscope is limited with the mechanical Brownian noise, the sense mode quality factor directly affects the gyro performance.

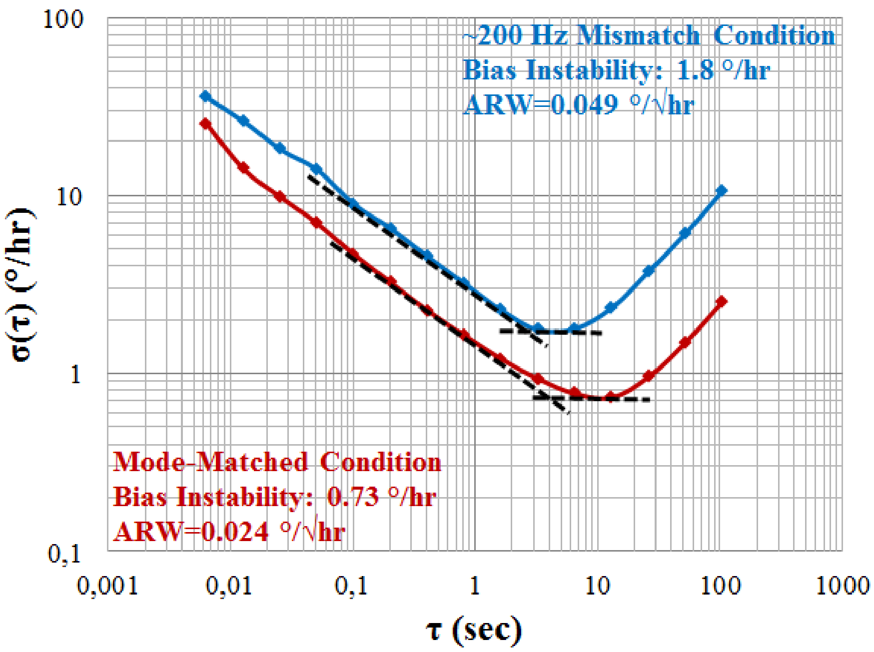

Figure 5.12: Allan Variance graphs of the gyroscope (D12) under the mode-matched and mismatched (~200 Hz) conditions.

To see the effect of mode-matching on linearity and determine dynamic range of the mode-matching system, the scale factor test, described in Section 5.2 are performed for the gyroscope (C05). Figure 5.13 shows the measured angular rate response and corresponding R^2 linearity of the gyroscope (C05) operated under the mode-matched condition. R^2 linearity, obtained by fitting a line to a real slope of the gyroscope rate output, is not the actual linearity. The actual linearity is calculated by dividing the maximum deviation of the real slope from the fitted line to the whole range of the applied angular rotation rate. The actual linearity for the mode-matched gyroscope (C05) is found to be 99.99%. Furthermore, the actual linearity is calculated to be 99.98% for the ~200 Hz mismatched gyroscope (C05) operation. Since the obtained linearity results are quite close to each other for both mode-matched and ~200 Hz mismatched gyroscope operations, it is concluded that there is considerably no effect of the mode-matching on linearity. The mode-matched gyroscope has a dynamic range of ±90 °/sec, but it is not the maximum limit for the mode-matching system. The dynamic range can be significantly increased above that value by reducing the gain of the Opamp that is used to provide a gain at the rate output of the gyroscope.

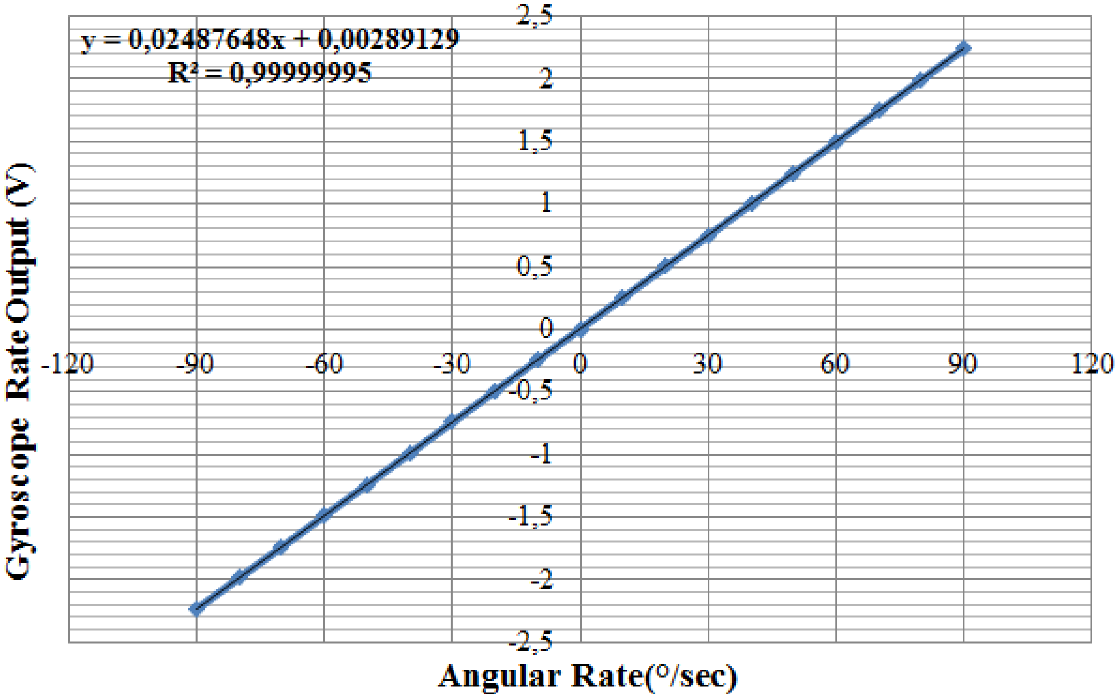

Figure 5.13: Measured angular rate response and corresponding R^2 linearity of the gyroscope (C05) operated under the mode-matched condition.

5.4 Performance Test Results under Different Temperature and Vacuum Conditions

First, the thermal stability of the resonance modes of the gyroscope should be concerned to ensure proper mode-matched gyroscope operation. Figure 5.14 shows the measured frequency variation of the individual unmatched resonance modes of the gyroscope (D12) as a function of temperature. Temperature coefficients of the drive and sense mode resonance frequencies of the gyroscope (D12) are measured to be -12.6 ppm/°C and -23.9 ppm/°C in a range from -40 °C to 80 °C. The resonance frequency variation with changing temperature is attributed to the temperature dependence of the Young's modulus of the single crystalline silicon used to form device layer of the sensor.

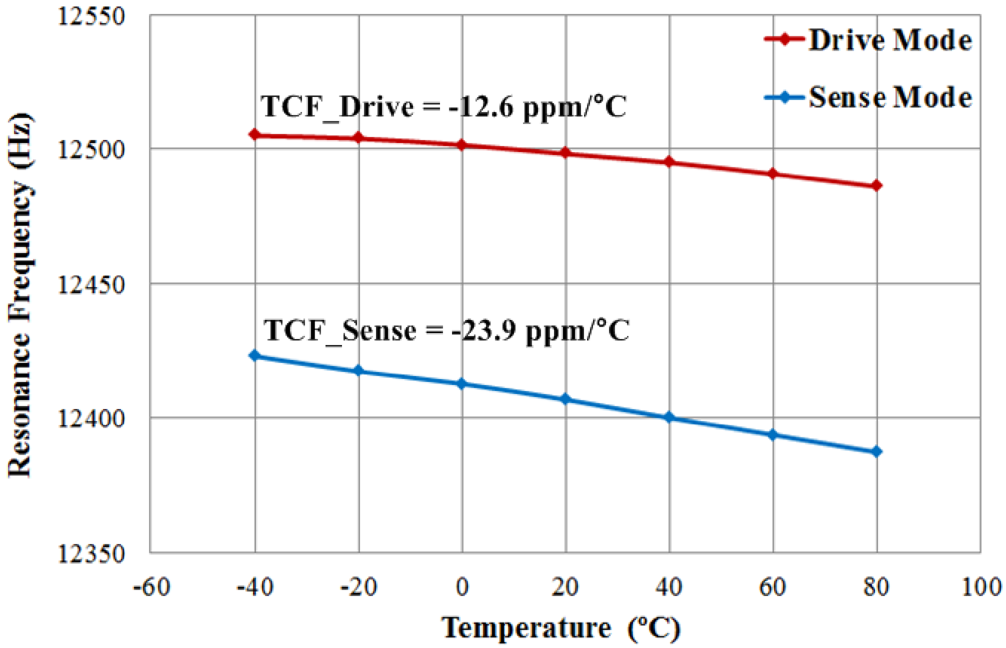

Figure 5.14: Measured frequency variation of the individual unmatched resonance modes of the gyroscope (D12) as a function of temperature.

Referring to Figure 5.14, the measured temperature coefficients of the resonance modes of the gyroscope are different than each other in a temperature range from-40°C to 80°C. However, once the resonance modes of the gyroscope are perfectly matched, they track each other on the condition of changing temperature without requiring any calibration, and hence the mode-matching is maintained over temperature with the aid of the fully-closed loop mode-matching system.

Allan Variance tests are performed at three different temperature settings. In each of the temperature settings, the thermal equilibrium is satisfied between the ambient and device before recording the zero-rate output data. To achieve the thermal equilibrium, the gyroscope is allowed to attain to a desired temperature for a minimum period of 3 hours. Before Allan Variance tests, the quality factors of the resonance modes of the gyroscope are monitored for three different temperature settings, shown in Table 5.7. As seen in Table 5.7, an increase in temperature leads to the quality factor degradation at the operating gyroscope resonance modes.

Table 5.7: Measured quality factor of the resonance modes of the gyroscope (D12) with temperature.

Temperature (°C)	Drive Mode Quality Factor	Sense Mode Quality Factor
25	30114	1541
50	25366	1331
75	19343	1178

In Allan Variance tests, the gyroscope (D12) is operated under the mode-matched condition with the drive displacement of 4.5 µm. Figure 5.15 shows the Allan Variance graphs of the tested gyroscope (D12) obtained at temperatures of 25 °C, 50 °C, and 75 °C.

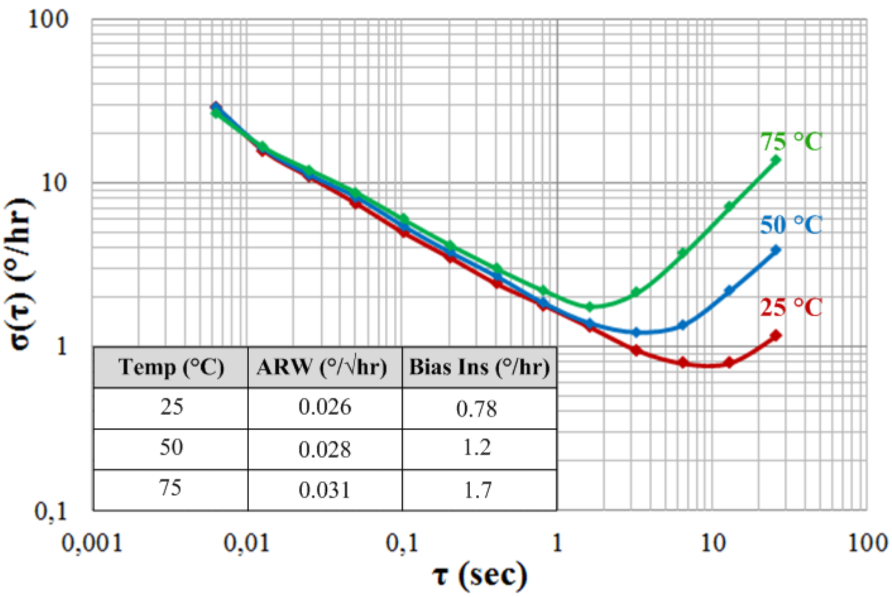

Temp (°C)	ARW (°/√hr)	Bias Ins (°/hr)
25	0.026	0.78
50	0.028	1.2
75	0.031	1.7

Figure 5.15: Allan Variance graphs of the tested gyroscope (D12) obtained at temperatures of 25 °C, 50 °C, and 75 °C.

As seen in Figure 5.15, the gyroscope demonstrates the ARW performance of 0.026 °/√hr and bias instability performance of 0.78 °/hr at 25 °C, which is not far from the reported gyroscope performance of the gyroscope (D12), shown in Figure 5.12. The ARW and bias instability performances of the gyroscope is degraded with increasing temperature, which primarily results from the sensitivity of the sense mode quality factor to temperature variations.

After temperature tests, Allan Variance tests are performed for two different vacuum settings to verify the effect of the electronic noise suppression on the performance of the gyroscope under the mode-matched condition. The special device, called vacuum chamber, is used to operate the gyroscope with the controller electronics under different vacuum level conditions. This device provides an opportunity to stabilize vacuum level, which is required to prevent possible quality factor variations at the resonance modes of the gyroscope. After stabilizing the vacuum level at two different vacuum settings, the quality factors of the resonance modes of the gyroscope (F09) are obtained from the resonance tests, shown in Table 5.8. The quality factor is directly associated with the vacuum through the damping factor. It improves as the vacuum decreases thanks to a reduction in the damping factor. The measured operating mode quality factors of the gyroscope (F09) highlights the quality factor improvement in each of the individual resonance modes with decreasing vacuum levels.

Table 5.8: Measured quality factors of the resonance modes of the gyroscope (F09) with vacuum settings.

Vacuum (mTorr)	Drive Mode Quality Factor	Sense Mode Quality Factor
10	133812	7961
250	22798	1229

In the vacuum tests, the gyroscope is operated under the mode-matched condition with the drive displacement of 4.5μm. Figure 5.16 shows the Allan Variance graphs of the tested gyroscope (F09) obtained for vacuum ambient of 10 mTorr and 250 mTorr. The

ARW performance of the gyroscope improves from 0.031 °/√hr to 0.014 °/√hr as the vacuum level decreases from 250 mTorr to 10 mTorr, which primarily caused by a reduction in the mechanical Brownian noise of the gyroscope. This indicates and verifies that the mechanical Brownian noise becomes a dominant noise source under the mode-matched gyroscope operation. In other words, the electronic noise of the sense mode controller is almost totally suppressed with mode-matching. Furthermore, the bias instability performance of the gyroscope improves up to 1.5 times in a vacuum condition of 10 mTorr compared to a vacuum condition of 250 mTorr thanks to a sensitivity improvement at the gyroscope which also results from an increase in the sense mode quality factor.

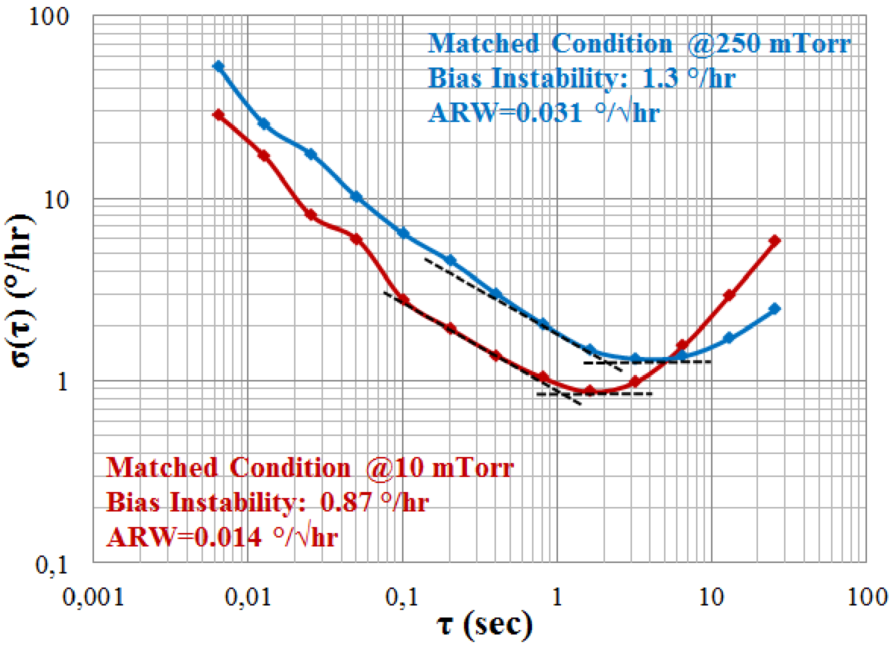

Figure 5.16: Allan Variance graphs of the tested gyroscope (F09) obtained for vacuum levels of 10 mTorr and 250 mTorr.

5.5 Experimental Bandwidth Verification of the Mode-Matching System

In this study, the system bandwidth is electronically adjusted through the closed loop sense mode controller, independently from the mechanical sensor bandwidth. The system bandwidth measurement is experimentally performed using the rate table that provides a sinusoidal angular rotation rate to the system with a maximum frequency of 42 Hz. First, the amplitude information of the sense pick output signal is collected through the dynamic signal analyzer in the presence of the sinusoidal angular rate inputs with the same amplitudes and different frequencies, starting from DC to 42 Hz with 6 Hz intervals. Then, the collected data is overlapped with the simulated data, shown in Figure 3.16, to form the frequency response characteristics of the mode-matching system. Figure 5.17 shows the frequency response of the mode-matching system that is measured up to 42 Hz and then overlapped with the simulated data. The measured and simulated data are consistent with each other. This consistency evidently verifies and indicates that the system bandwidth, corresponding to 3 dB point, is greater than 50 Hz.

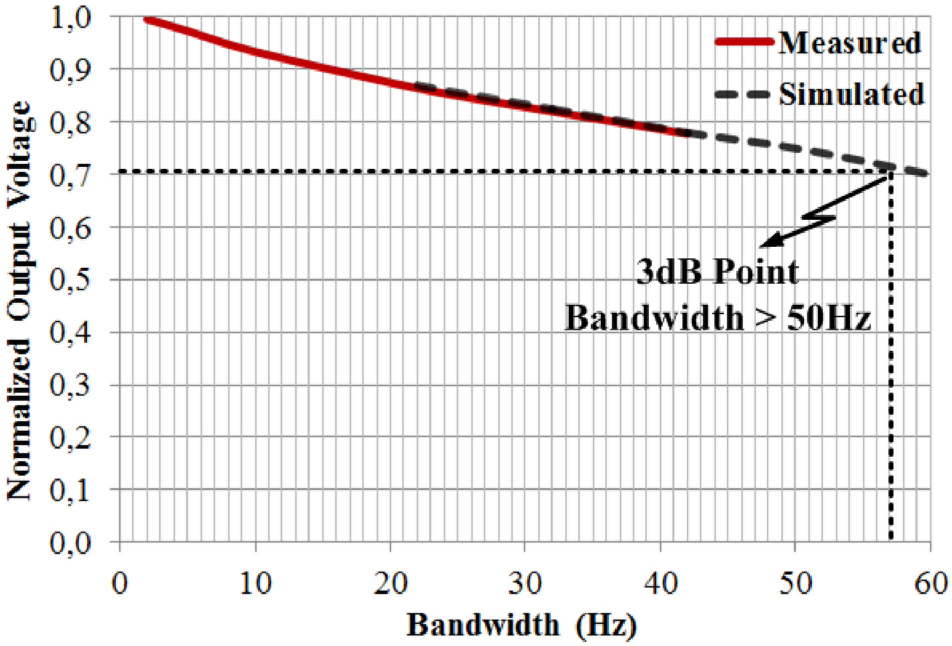

Figure 5.17: Frequency response of the mode-matching system that is measured up to 42 Hz and then overlapped with the simulated data.

Figure 5.18 shows the measured sense mode output in response to two different angular rate inputs with amplitudes of 2π °/sec and frequencies of 20 Hz and 40 Hz. The amplitude of the sidelobes, corresponding to the sinusoidal angular rate signals with a frequency of 20 Hz and 40 Hz, is about 21.6 mV_{rms} and 23.6 mV_{rms}, respectively. These amplitudes agree with the frequency response of the mode-matching system, shown in Figure 5.17. The central peak at the drive mode resonance frequency corresponds to the measured sum of the residual quadrature and in-phase Coriolis coupling offset signals. The amplitude of the central peak is quite small compared to the amplitude of the sidelobes. This ensures the functionality of the mode-matching system because if it does not properly work, the quadrature signal would not be minimized since the phase relationship in the closed loop quadrature controller will be inconsistent for proper operation.

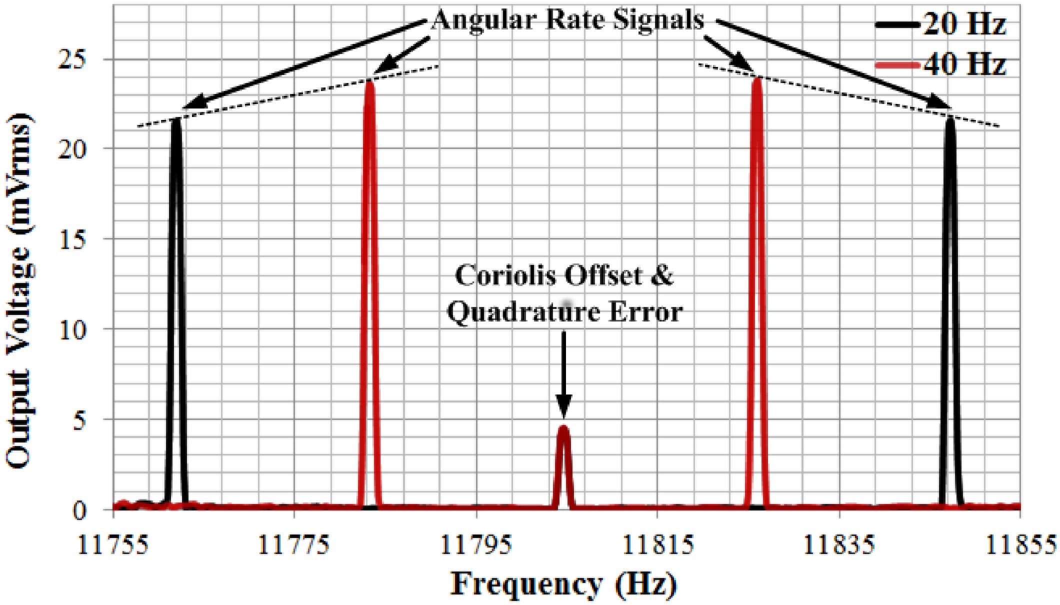

Figure 5.18: Measured sense mode output in the presence of a sinusoidal angular rate signals, having amplitudes of 2π °/sec and frequencies of 20 Hz and 40 Hz.

5.6 Summary

This chapter presents the performance test results of the studied MEMS gyroscopes. The experimental verification of the system bandwidth is also covered in this chapter. In order to perform the performance tests, the proposed closed loop drive, sense, quadrature cancellation, and mode-matching controllers are integrated with the vacuum packaged gyroscope on the designed PCB. The electronic controller and gyroscope modules are constructed using the hybrid packages for low noise measurements.

Tests are started to control the functionality of the mode-matching system. It is shown that the mode-matching system is successfully operated because the phase relationship between the quadrature and drive signals is consistent with each other. Furthermore, it is verified that the transient behavior of the mode-matching controller obtained during tests approximately matches with the simulation results.

There are two methods used to achieve mode-matching, mentioned in Section 5.1. The performance tests are performed for these two methods. In the first method, the fully-decoupled gyroscopes are tested under the mode-matched and mismatched (~100 Hz) conditions. The amount of mismatch (~100 Hz) between the resonance modes is chosen to perform mismatch operation because it is the point where the highest performance is obtained for the mismatch gyroscope operation. It is verified from test results that the mode-matching operation enhances the performance of the studied gyroscopes up to 2.4 times in bias instability and 1.7 times in ARW, reaching down to 0.83 °/hr and 0.026 °/√hr, respectively. In the second method, the single-mass fully-decoupled gyroscopes are tested under the mode-matched and mismatched (~200 Hz) conditions. The mismatch amount between the resonance modes is increased from 100 Hz to 200 Hz to clearly see the effect of mode-matching on the performance of the gyroscope because the performance of the gyroscope decreases with increasing mismatch amount due to a decrease in the sensor sensitivity. The mode-matched gyroscope operation improves the performance of the gyroscope up to 2.6 times in bias instability and 2 times in ARW, reaching down to 0.73 °/hr and 0.024 °/√hr, respectively. It is concluded from the performance tests that the performance of the mode-matched gyroscopes is limited with the mechanical Brownian noise of the sensor that is the highest achievable performance for the gyroscope operation. Based on the conclusion, the electronic noise at the mode-matching system is almost totally suppressed with mode-matching thanks to the sensitivity improvement of the gyroscope, which is also verified through the noise analysis of the gyroscope (C05), described in Section 3.6.

This study mainly focuses on the second mode-matching implementation because mode-matching is achieved using the frequency tuning electrodes, which enables to perform matching between the resonance modes of the gyroscopes as an independent of the proof mass potential. The proof mass potential variation is not desired during mode-matching because it affects the overall dynamics of the system.

The performance tests are also performed under different temperature and vacuum conditions for the second mode-matching implementation. In temperature tests, frequency characteristics of the individual unmatched resonance modes are first investigated with changing temperature in a range from -40 °C to 80 °C. Then, the performance tests are performed using the mode-matched gyroscope for temperature settings of 25 °C, 50 °C, and 75 °C. Temperature test results show that the performance of the gyroscope is degraded with increasing temperature, which results from the sensitivity of the quality factor to temperature variations. In vacuum tests, the mode-matched gyroscope is tested under different vacuum ambient conditions. It is observed that the gyroscope performance substantially improves in the lower vacuum level thanks to the quality factor improvement of the sense mode.

The mode-matched gyroscope has a linearity of 99.99% in a range of ±90°/sec, which is not the dynamic range limit for the mode-matching system because it can be significantly increased above that range changing the gain of Opamp used to provide gain at the rate output of the sense mode controller.

Finally, the system bandwidth measurement is experimentally performed up to 42 Hz, limited by the rate table used in tests. Then, the experimental and simulation data are overlapped with each other. These are consistent with each other. This consistency indicates and verifies that the system bandwidth is greater than 50 Hz for the proposed mode-matching system.

CHAPTER 6

CONCLUSIONS AND FUTURE WORK

This work presents the mode-matching system and demonstrates the effect of mode-matching on the performance of the gyroscope providing experimental data. In the first proposed mode-matching system, the fully-decoupled gyroscopes are first modified to make them suitable for the mode-matched gyroscope operation. The details of the modifications of the fully-decoupled gyroscope can be found in Section 1.4. Then, the closed loop drive, sense force-feedback, quadrature cancellation, and mode-matching controllers are designed and verified through the closed loop analysis performed in SIMULINK design software. Next, the modified fully-decoupled gyroscopes are integrated with the closed loop controller electronics on the designed PCB. It should be noted that the gyroscope with the front-end electronics and closed loop controllers are packaged using the special hybrid packages for low noise measurements. Following, the Allan Variance tests of the studied gyroscopes are performed under the mode-matched and mismatched conditions to evaluate the effect of mode-matching on the performance of the gyroscope. The main motivation behind the first mode-matching implementation is to tune the sense mode resonance frequency by changing the proof mass potential. In this study, the proof mass potential variation is not desired in the gyroscope operation because it affects the overall system dynamics of the system. Therefore, the second mode-matching method is proposed to eliminate the proof mass potential variation at the system. This study mainly focuses on the second proposed mode-matching system, in which mode-matching is accomplished using the frequency tuning electrodes, which provides the tuning capability of the sense mode resonance frequency without changing the proof mass potential. In the first step, the governing equations of the drive mode, sense mode, and frequency tuning electrodes are derived. Regarding these governing equations, the single-mass fully-decoupled gyroscopes including the frequency tuning electrodes are designed, and then FEM simulations are performed to identify the mode shapes and their modal frequencies of the gyroscope. Next, the designed gyroscopes are fabricated using facilities of METU-MEMS Research and Applications Center. Closed loop drive, sense, quadrature, and mode-matching controllers are designed and verified in the SIMULINK design software. The similar packaging technique, used in the first implementation, is also used for low noise measurements combining the fabricated gyroscopes with the controller electronics. Then, the effect of mode-matching on the performance of the gyroscope is evaluated through the Allan Variance tests. An analytical noise analysis is also performed to see the effect of mode-matching on the gyro performance. Finally, the system bandwidth is experimentally determined by overlapping the experimental and simulated data with each other.

Results of this study and accomplishments can be listed as follows:

1. There are number of different approaches presented in the literature to reduce a frequency split between resonance modes of the gyroscope. Some of them rely on manual tuning efforts, which make them unsuitable in terms of time, cost, and process complexity. Therefore, an automatic tuning is desirable to adjust the resonance mode frequencies of the gyroscope. This work, for the first time in the literature, proposes an automatic mode-matching system that uses the phase relationship between the residual quadrature and drive signals in the gyroscope. The main motivation behind the proposed mode-matching system is to tune the sense mode resonance frequency with respect to the drive mode resonance frequency using an electrostatic spring constant effect.

2. Design of the single-mass fully-decoupled gyroscope including the frequency tuning electrodes is carried out to eliminate the requirement for the proof mass potential variations. The frequency tuning electrodes provides the capability of tuning the sense mode resonance frequency with respect to the drive mode resonance frequency by generating an electrostatic spring constant effect without changing the proof mass potential. They are placed on a sense frame in a special

capacitive configuration that provides higher tuning capability compared to the sense electrodes. Also, the special capacitive configuration prevents the scale factor variation by generating an equal amount of electrostatic forces acting on the sense frame. The expression of the generated electrostatic force and spring constant effect in the frequency tuning electrodes are derived. Furthermore, in the design stage of the single-mass full decoupled gyroscope, the resonance frequencies of the higher order modes are kept two times higher than the drive and sense mode resonance frequencies to ensure proper gyroscope operation.

3. Closed loop drive, sense, quadrature cancellation, and mode-matching controllers are designed regarding the phase requirements of the proposed mode-matching method. The closed loop controllers except the mode-matching controller are optimized through the open loop and closed loop analysis, which are performed to adjust the PI controller parameters and to observe the transient behavior of the closed loop controller. The pole-zero cancellation method is used in these controllers, which provides substantial increase in the transient response time (settling time) of the controllers. The closed loop sense mode feedback mechanism enables to achieve substantial improvement in the system bandwidth with the aid of the pole-zero cancellation, independently from the mechanical sensor bandwidth. The noise analysis is performed for the sense mode controller because it mainly determines the minimum detectable rate amount. It is shown that the preamplifier noise is the dominant electrical noise at the sense mode controller. However, the electronic noise is substantially suppressed under the mode-matched case thanks to the sensitivity improvement of the gyroscope. The effect of the electronic noise at the sense mode controller is found to be approximately 50 times smaller than the mechanical Brownian noise for the mode-matched gyroscope (C05). This indicates and verifies that the performance of the mode-matched gyroscope is directly determined by the mechanical Brownian noise in this work. Furthermore, the mode-matching controller is directly optimized through the closed loop analysis instead of the open loop analysis because during the mode-matched gyroscope operation, the

sense mode dynamics of the gyroscope shows nonlinear characteristics due to the sense mode resonance frequency variation. It is observed from the closed loop analysis that the settling time of the mode-matching controller depends on the initial frequency split between the resonance modes.

4. The fabrication of the single-mass fully-decoupled gyroscopes is carried out using SOI-based SOG process. It is observed that the designed capacitive gaps and spring widths after the fabrication are wider and narrower, respectively. This is a result of the critical dimension loss problem that is caused by lithography tolerances and finite lateral etch of DRIE during the formation of the structural layer of the device. Therefore, although the gyroscope is designed to be nearly matched for 10 V proof mass potential, a non-uniform shift in the resonance mode frequencies of the gyroscope are observed. Furthermore, the critical dimension loss at the capacitive gaps of the gyroscope adversely affects the performance of the gyroscope, the quadrature suppression capability of the quadrature electrodes, the frequency tuning capability of the frequency tuning electrodes.

5. The tested gyroscope, combined with front-end electronics, and closed loop controller modules are integrated on the designed PCB. Each of the modules is prepared using the hybrid packages and high-quality discrete electronics components for low noise measurements. Then, the phase relationship consistency between the quadrature and drive signals is verified through the functionality test of the mode-matching system. The transient behavior of the mode-matching controller is observed for different initial frequency splits between the resonance mode frequencies. It is concluded that the settling time of the mode matching controller significantly relies on the initial frequency split between the resonance modes of the gyroscope, which indicates and verifies that the simulation results approximately match with the experimental results regarding the fabrication imperfections. Scale factor tests of the studied gyroscopes are performed for the first and second mode-matching

implementations. In the first mode-matching implementation, the scale factor variations are observed in the mode-matched and mismatched gyroscope operations due to the proof mass potential variation. In the second mode-matching implementation, it is verified that the applied potential to the frequency tuning electrodes, used to adjust the amount of frequency mismatch between the resonance modes, does not affect the scale factor that is constant for the mode-matched and mismatched gyroscope operations thanks to the fixed proof mass potential. Allan Variance tests are performed for the mode-matched and mismatched gyroscope operations. Test results demonstrate a substantial performance improvement up to 2.6 times in bias instability and 2 times in ARW with the mode-matching, reaching down to 0.73 °/hr and 0.024 °/√hr, respectively. It is also observed from the tests results that the measured and calculated ARW performances of the gyroscope (C05) are consistent with each other. This obviously verifies and indicates that the electronic noise coming from the sense mode controller is almost totally suppressed under the mode-matched condition. This means that the performance of the mode-matched gyroscope came to a mechanical Brownian noise limit with mode-matching. Therefore, further performance improvement can be achieved by reducing the mechanical Brownian noise of the gyroscope.

6. Allan Variance tests are also performed under different temperature and vacuum conditions. In temperature tests, frequency characteristics of the individual unmatched resonance modes are first investigated with changing temperature in a range from -40 °C to 80 °C. It is shown that although the temperature coefficients of drive and sense mode resonance frequencies are different, the proposed mode-matching system achieves and maintains the frequency matching condition without requiring any calibration. The performance of the gyroscope is evaluated for temperature settings of 25 °C, 50 °C, and 75 °C. Tests results highlight that the quality factor of the gyroscope reduces with increasing temperature as expected, which results in a degradation in the performance of the gyroscope. In vacuum tests, the performance of the mode-matched gyroscope

substantially improves on the condition of decreasing vacuum level thanks to the quality factor enhancement of the sense mode. It is shown that the performance improvement is directly associated with the reduction in the mechanical Brownian noise. This also verifies that the mechanical Brownian noise substantially dominates the electronic noise at the mode-matched gyroscope operation.

7. Linearity and dynamic range are measured from the scale factor tests. The linearity of the mode-matched gyroscope is 99.99%, quite close to 1. The mode-matched gyroscope has a dynamic range of ±90 °/sec, which is not the maximum dynamic range limit. It can be increased above that range without sacrificing linearity. The system bandwidth is experimentally measured up to 42 Hz, limited by the rate table used in tests. Then, the simulated and measured data are overlapped with each other. It is observed that they are consistent with each other. From this consistency, it is verified that the system bandwidth is greater than 50 Hz for the proposed fully closed loop mode-matching system.

The major achievement of this study is that sub-degree per-hour gyroscope performance is achieved with greater than 50 Hz system bandwidth and without sacrificing linearity through the proposed mode-matching system. This makes the proposed mode-matching system suitable for high-end of tactical grade applications. To achieve further performance improvement at the gyroscope operation, some of the topics are listed as follows:

1. Wafer level vacuum packaging should be performed to achieve performance improvement at the mode-matched gyroscope operation. This will significantly improve the quality factors of the resonance modes of the gyroscope providing substantial reduction at the vacuum level compared to the current packaging technique. The increase in the quality factors directly enhances the noise performance of the gyroscope because it reduces the mechanical Brownian noise,

coming from the sensor; and electronic noise, coming from the sense mode controller.

2. A new gyroscope can be designed to decrease the ratio of m_S/m_{PM}, where m_S and m_{PM} are mass of the sense frame and proof mass frame. If this ratio is reduced through the new mechanical design, the mechanical Brownian noise decrease, and hence the gyroscope performance is improved.

3. A fully-automated digital control can be implemented combining the current controller loops in a single chip. Hence, the overall size of the system can be significantly reduced, and the controller parameters can be automatically adjusted in the presence of environmental condition variations. Moreover, the performance of the gyroscopes can be enhanced by reducing the electronic noise by means of the digital control.

REFERENCES

[1] http://pradeepchakraborty.wordpress.com/2010/09/16/focus-on-gyroscopes-for mobile phone-applications-yole/.

[2] B. R. Johnson, E. Cabuz, H. B. French, and R. Supino, “Development of a MEMS Gyroscope for Northfinding Applications,” *Position Location and Navigation Symposium (PLANS)*, pp.168-170, May 2010.

[3] A. Persson, “How Do We Understand the Coriolis Force?,” *Bulletin of the American Meteorological Society*, Vol. 79, No. 7, July 1998.

[4] N. Yazdi, F. Ayazi, and K.Najafi, “Micromachined Inertial Sensors,” *Proceedings of the IEEE*, Vol. 86, No. 8, pp.1640-1659, August 1998.

[5] IEEE Standard for Inertial Sensors Terminology, *IEEE Std 528-2001*, August 2001.

[6] H. Wu., “System Architecture for Mode-Matching a MEMS Gyroscope,” *M. of Eng. Thesis*, *MIT*, June 2009.

[7] Bryan, G. H., “On the Beats in the Vibrations of a Revolving Cylinder or Bell,” *In Proceedings of the Cambridge Philosophical Society*, Vol. 7, No. 3, pp. 101, November 1890.

[8] P. Greiff, B. Boxenhorn, T. King, and L. Niles, ”Silicon Monolithic Micromechanical Gyroscope,” *6th International Conferenceof Solid-State Sensors and Actuators*, San Francisco, CA, pp. 966-968, June 1991.

[9] J. Bernstein, S. Cho, A. T. King, A. Kourepenis, P. Maciel, and M. Weinberg, “A Micromachined Comb-Drive Tuning Fork Rate Gyroscope,” *Proc. of IEEE Micro Mechanical Systems Workshop*, Fort Lauderdale, FL, pp. 143-148, February 1993.

[10] M. W. Putty and K. Najafi, “A Micromachined Vibrating Ring Gyroscope,” *Solid-State Sensor and Actuator Workshop,* Hilton Head Island, SC, pp. 213–220, June 1994.

[11] A. Selvakumar and K. Najafi, “High Density Vertical Comb Array Microactuators Fabricated Using a Novel Bulk/Poly-silicon Trench Refill Technology,” *Solid-State Sensor and Actuator Workshop,* Hilton Head Island, SC, USA, pp. 138–141, 1994.

[12] F. Ayazi and K. Najafi, “A HARPSS Polysilicon Vibrating Ring Gyroscope,” *Journal of Microelectromechanical Systems,* Vol. 10, No. 2, pp. 169-179, June 2001.

[13] G. He and K. Najafi, “A Single-Crystal Silicon Vibrating Ring Gyroscope,” *Proceedings of the IEEE Micro Electro Mechanical Systems Workshop,* Las Vegas, CA, pp. 718-721, January 2002.

[14] M. Lutz, W. Golderer, J. Gerstenmeier, J. Marek, B. Maihofer, S. Mahler, H.Munzel, and U. Bischof, “A Precision Yaw Rate Sensor in Silicon Micromachining,” *Tech. Dig. 9th Int. Conf. Solid-State Sensors and Actuators (Transducers’97),* Chicago, IL, pp. 847-850, June 1997.

[15] K. Tanaka, Y. Mochida, S. Sugimoto, K. Moriya, T. Hasegawa, K. Atsuchi, and K. Ohwada, “A Micromachined Vibrating Gyroscope,” *Proceedings of the International Conference on Micro Electro Mechanical Systems,* Netherlands, pp. 278-281, January 1995.

[16] K. Funk, H. Emmerich, A. Schilp, M. Offenberg, R. Neul, and F. Larmer, , "A Surface Micromachined Silicon Gyroscope Using a Thick Polysilicon Layer," *Proceedings of the International Conference on Micro Electro Mechanical Systems*), pp.57-60, January 1999.

[17] J. A. Geen, S. J. Sherman, J. F. Chang, and S. R. Lewis, "Single-Chip Surface Micromachined Integrated Gyroscope with 50°/h Allan Deviation," *Solid-State Circuits, IEEE Journal of* , Vol. 37, No. 12, pp. 1860- 1866, December 2002.

[18] H. Luo, X. Zhu, H. Lakdawala, L. R. Carley, and G. Fedder, “A Copper CMOS-MEMS Z-Axis Gyroscope,” *in Proc. IEEE Micro Electro Mechanical Systems Workshop*, Las Vegas, CA, pp. 631-634, January 2002.

[19] H. Xie and G. K. Fedder, “Fabrication, Characterization, and Analysis of a DRIE CMOS-MEMS Gyroscope,” *IEEE Sensors Journal*, Vol. 3, No. 5, pp. 622-631, October 2003.

[20] B. L. Lee, S. W. Lee, K. D. Jung, J. H. Choi, T. R. Chung, and Y. C. Cho, “A Decoupled Vibratory Gyroscope Using a Mixed Micromachining Technology,” *Proceedings of the IEEE Int. Conf. on Robotics&Automation (ICRA’01),* Korea, pp. 3412-3416, May 2001.

[21] W. Geiger, W. U. Butt, A. Gaiβer, J. Frech, M. Braxmaier, T. Link, A. Kohne, P. Nommensen, H. Sandmaier, and W. Lang, “Decoupled Microgyros and the Design Principle DAVED,” *Sensors Actuators A*, Vol. 95, pp. 239-249, 2002.

[22] A. Sharma, F. M. Zaman, B. V. Amini, and F. Ayazi, “A High-Q In-Plane SOI Tuning Fork Gyroscope,” *Proc. IEEE Sensors Conf.*, Austria, pp. 467-470, October 2004.

[23] C. Acar and A. M. Shkel, “Structurally Decoupled Micromachined Gyroscopes with Post-Release Capacitance Enhancement,” *J. Micromech. Microeng.,* Vol. 15, pp. 1092-1101, 2005.

[24] M.F. Zaman, A. Sharma, and F. Ayazi, “High Performance Matched-Mode Tuning Fork Gyroscope,” *Proceedings of the International Conference on Micro Electro Mechanical Systems,* Istanbul, pp. 66-69, 2006.

[25] A. Sharma, M. F. Zaman, and F. Ayazi, “A Sub 0.2 °/hr Bias Drift Micromechanical Gyroscope With Automatic CMOS Mode-Matching,” *IEEE Journal of Solid State Circuits*, Vol. 44, No. 5, pp. 1593-1608, May 2009.

[26] B. Chaumet, B. Leverrier, C. Rougeot, and S. Bouyat, “A New Silicon Tuning Fork Gyroscope for Aerospace Applications,” *Symposium Gyro Technology*, pp. 1.1-1.13, Karlsruhe, Germany, September 2009.

[27] D. Lapadatu, B. Blixhavn, R. Holm, and T. Kvisteroy, “SAR500 - A High-Precision High-Stability Butterfly Gyroscope with North Seeking Capability,” *Position Location and Navigation Symposium (PLANS), 2010 IEEE/ION*, pp. 6-13, May 2010.

[28] E. Tatar, S. E. Alper, and T. Akin, “Quadrature Error Compensation and Corresponding Effects on the Performance of Fully Decoupled MEMS Gyroscopes,” *IEEE/ASME Journal of Micro Electro Mechanical Systems*, Vol. 21, No. 3, pp. 656-667, June 2012.

[29] S. Sonmezoglu, S. E. Alper, and T. Akin, “An Automatically Mode-Matched MEMS Gyroscope with 50 Hz Bandwidth,” *Micro Electro Mechanical Systems (MEMS), 2012 IEEE 25th International Conference on.*, pp. 523-526, January 2012.

[30] M. M. Torunbalci, E. Tatar, and S. E. Alper, and T. Akin, “Comparison of Two Alternative Silicon-on-Glass Microfabrication Processes for MEMS Inertial Sensors,” *Proc. Eurosensors XXV*, Athens, Vol. 25, pp. 900-903, September 2011.

[31] T. Remtema and L. Lin, “Active Frequency Tuning for Microresonators by Localized Thermal Stressing Effects,” *Sensors and Actuators A*: *Physical*, Vol. 91, No. 3, pp. 326–332, July 2001.

[32] M. A. Abdelmoneum, M. M. Demirci, Y.W. Lin, and C. T. -C Nguyen, “Location-Dependent Frequency Tuning of Vibrating Micromechanical Resonators via Laser Trimming, ” *Frequency Control Symposium and Exposition, 2004. Proceedings of the 2004 IEEE International*, pp. 272- 279, August 2004.

[33] D. Joachim and L. Liwei, “Characterization of Selective Polysilicon Deposition for MEMS Resonator Tuning,” *J. Microelectromech. Syst.*, Vol. 12, No. 2, pp. 193-200, April 2003.

[34] D. J. Kim and R. T. M'Closkey, “A Systematic Method for Tuning the Dynamics of Electrostatically Actuated Vibratory Gyros,” *Control Systems Technology, IEEE Transactions on*, Vol. 14, No. 1, pp. 69- 81, January 2006.

[35] D. Keymeulen, et.al., “Tuning of MEMS Gyroscope Using Evolutionary Algorithm and Switched Drive-Angle Method,” *Aerospace Conference, 2006 IEEE*, pp. 1-8, January 2006.

[36] C. D. Ezekwe and B. E. Boser, “A Mode-Matching ΣΔ Closed-Loop Vibratory-Gyroscope Readout Interface with a 0.004°/s/√Hz Noise Floor over a 50 Hz Band,” *Solid-State Circuits, IEEE Journal of* , Vol. 43, No. 12, pp. 3039-3048, December 2008.

[37] H. Wu, “System Architecture for Mode-Matching a MEMS Gyroscope,” *Master of Engineering. Thesis, MIT*, June 2009.

[38] S. Sung, W.-T. Sung, C. Kim, S. Yun, and Y. J. Lee, “On the Mode-Matched Control of MEMS Vibratory Gyroscope via Phase-Domain Analysis and Design,” *Mechatronics, IEEE/ASME Transactions on*, Vol. 14, No. 4, pp.446-455, August 2009.

[39] E. Tatar, “Quadrature Error Compensation and Its Effects on the Performance of Fully Decoupled MEMS Gyroscopes,” *M.Sc. Thesis*, Middle East Technical University, September 2010.

[40] B. Eminoglu, S. E. Alper, and T. Akin, “An Optimized Analog Drive-Mode Controller for Vibratory MEMS Gyroscopes,” *Proc. Eurosensors XXV*, Vol. 25, pp. 1309-1312, September 2011.

[41] S. E. Alper, “MEMS Gyroscopes for Tactical-Grade Inertial Measurement Applications,” *Ph.D. Dissertation*, Middle East Technical University, September 2005.

[42] S.E. Alper, A. Aydemir, and T. Akin, “Stepped-Etching for Preserving Critical Dimensions in Through-Wafer Deep Reactive Ion Etching of Thick Silicon,” *IEEE International Conference on Solid State Sensors, Actuators and Microsystems, Transducers’09*, pp. 1110-1113, June 2009.

[43] E. Tatar, M. M. Torunbalci, S.E. Alper, and T. Akin, “A method and Electrical Model for the Anodic Bonding of SOI and Glass Wafers,” *Micro Electro Mechanical Systems (MEMS), 2012 IEEE 25th International Conference on.*, pp.523-526, January 2012.

[44] J. Cui, Z. Guo, Q. Zhao, Z. Yang, Y. Hao, and G. Yan, “Force Rebalance Controller Synthesis for a Micromachined Vibratory Gyroscope Based on Sensitivity Margin Specifications,” *Microelectromechanical Systems, Journal of* , Vol. 20, No. 6, pp. 1382-1394, December 2011.

[45] J. Raman, E. Cretu, P. Rombouts, and L. Weyten, “A Closed-Loop Digitally Controlled MEMS Gyroscope With Unconstrained Sigma-Delta Force-Feedback,” *Sensors Journal, IEEE* , Vol. 9, No. 3, pp. 297-305, March 2009.

[46] Analog Devices, “AD8608 Precision, Low Noise, CMOS, Rail-to-Rail, Input/Output Operational Amplifiers,” *Datasheet*, 2010.

[47] Analog Devices, “AD8222 Precision, Dual-Channel Instrumentation Amplifier,” *Datasheet*, 2010.

[48] B. Eminoglu, “Control Electronics for MEMS Gyroscopes and Its Implementation in a CMOS Technology,” *M.Sc. Thesis*, Middle East Technical University, February 2011.

[49] Analog Devices, “AD630 Balanced Modulator/Demodulator,” *Datasheet*, 2004.

[50] Analog Devices, “AD8630 Zero Drift, Single-Supply, Rail-to-Rail Input/Output Operational Amplifier,” *Datasheet*, 2010.

[51] O. J. Woodman, “An Introduction to Inertial Navigation,” August 2007.